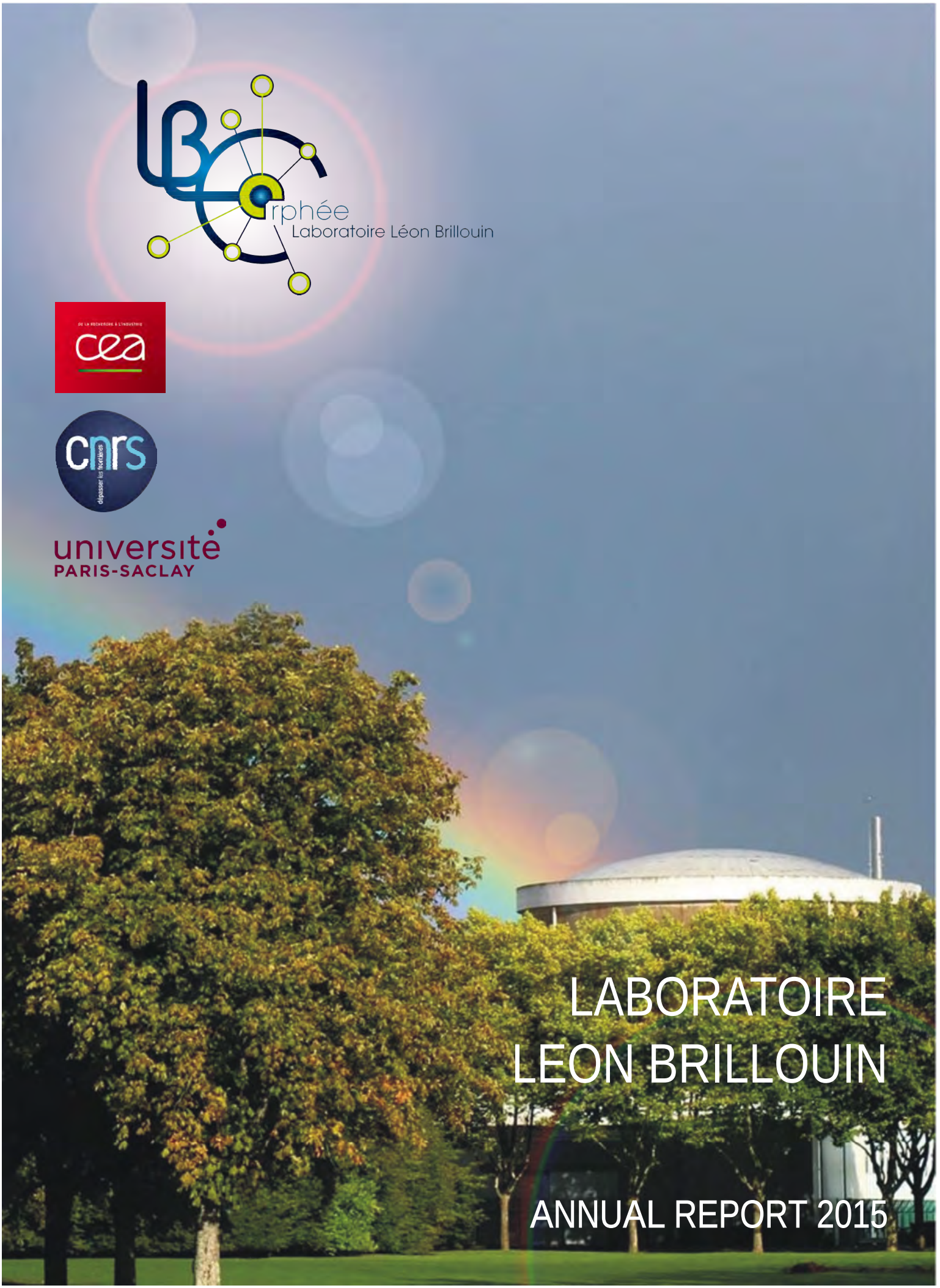

LABORATOIRE LEON BRILLOUIN

ANNUAL REPORT 2015

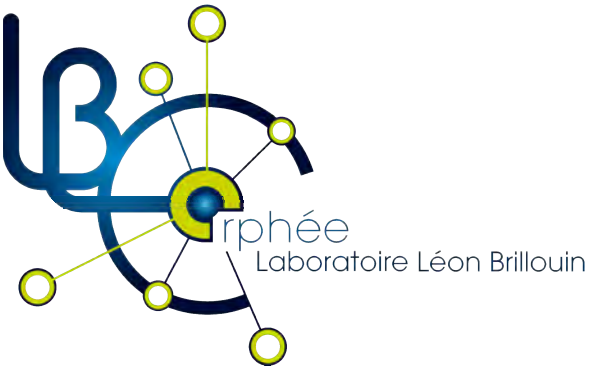

LABORATOIRE LEON BRILLOUIN

ANNUAL REPORT 2015

Table of contents

Director's foreword

In 2015 LLB fully played its role in developing Science with Neutrons and Instrumentation across the French Research Community. Using the Orphée Reactor as its principle resource, LLB is the hub for the use of the neutron probe and connects academic researchers, instrument developers, industry, and other scientific facilities in France and in Europe. It plays a critical role in preserving and developing the know-how in neutron based research that includes training new users, providing critical access to neutrons for established users, and training a cohort of new researchers and engineers who know how to build and develop instrumentation.

Insertion of the LLB within the new Paris Saclay University (in green) in the South West of Paris.

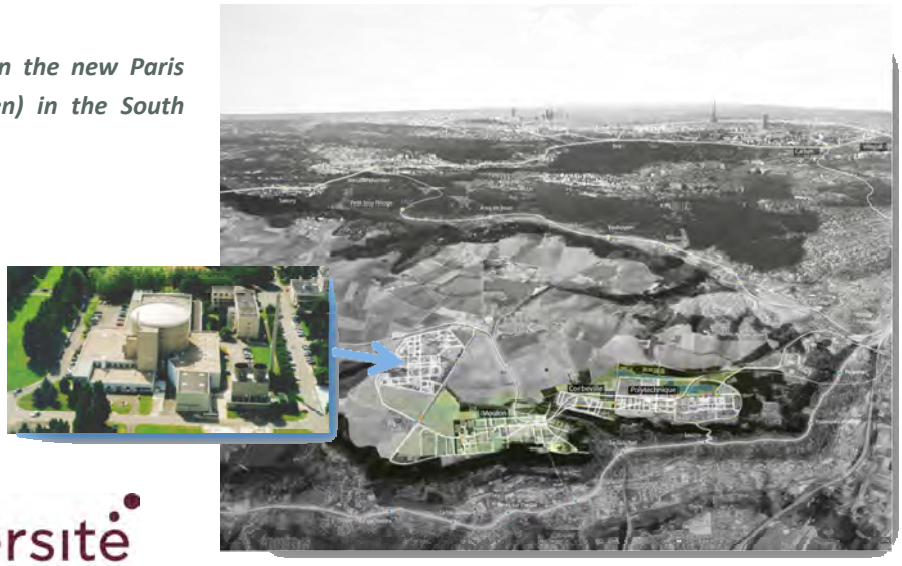

université
PARIS-SACLAY

In 2015, the LLB continued actively the renewal of its instrumental suite in 2015. Over the last five years, new strategically capabilities were developed and certainly aimed at providing new capability; ten instruments were created or upgraded covering most of the neutron methods, three others are into the commissioning process. However, in May 2015, faced with the uncertainty in the supply of highly enriched Uranium and the rising cost of fabrication of fuel elements for the Orphée reactor, the CEA and CNRS management announced that the Orphée reactor would operate at a reduced level of 120 days (full power equivalent) until a definitive shut down at the end of 2019. As a consequence the time-of-flight project FA# was stopped, but it might be built elsewhere.

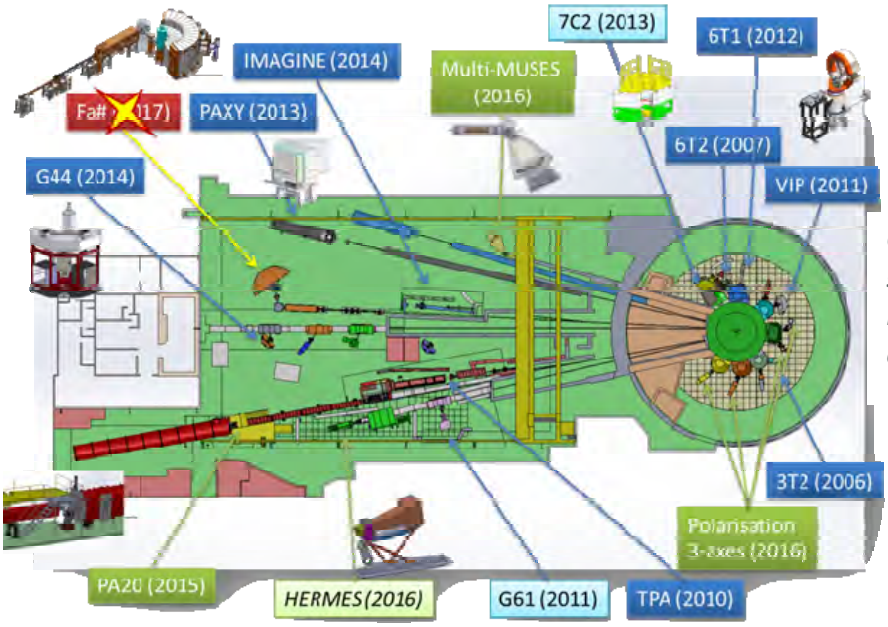

Guide hall and reactor hall of the LLB showing the new upgrade program. Names of the instruments are detailed at the end of the report.

In 2015, about 400 experiments were performed on all the instruments by more than 600 unique users. 42% of their research topics addressed Societal Grand Challenges but still satisfied a high demand on basic research and curiosity.

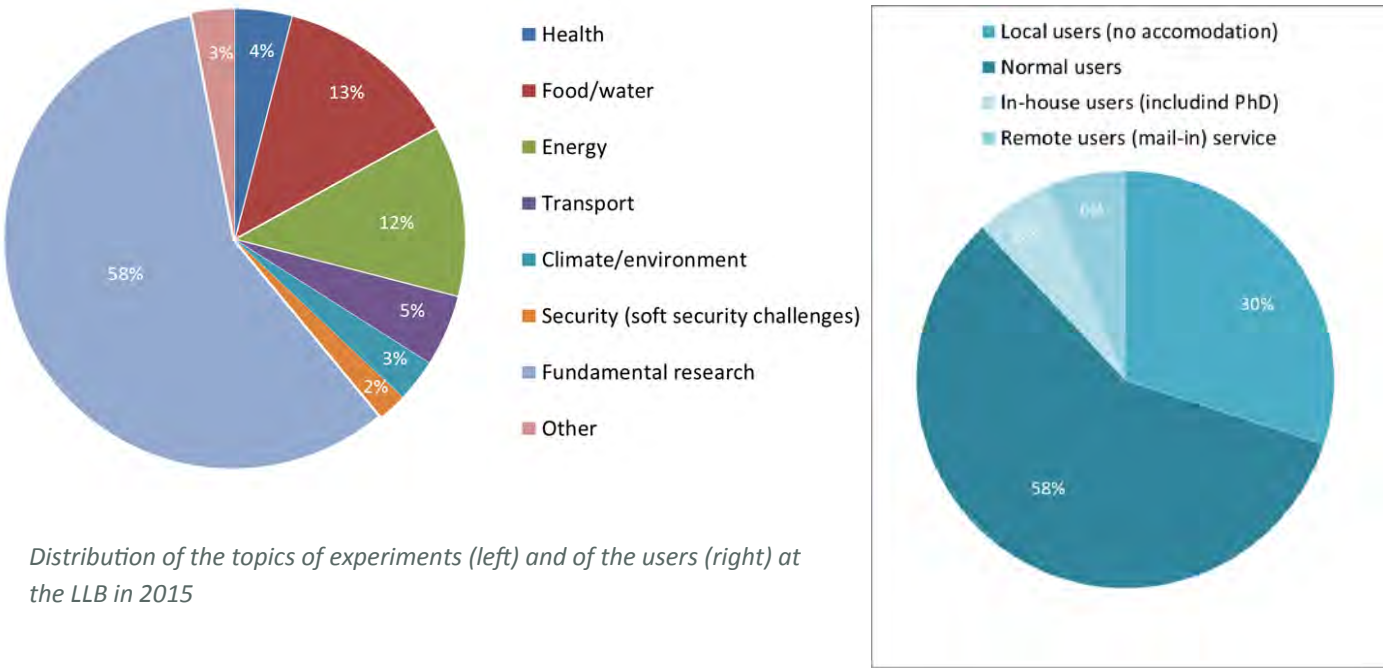

Distribution of the topics of experiments (left) and of the users (right) at the LLB in 2015

The involvement in ESS instrumentation is a recent mandate for LLB; 2015 was a quite successful year since all the proposed projects involving the LLB with its European partners were supported by the ESS ERIC Scientific Advisory Council and Steering Committee; it includes most of the NS methods in Diffraction, Spectroscopy and Larges Scale Structures. A management structure was proposed, where the LLB ensures its role. Over the years, LLB is becoming an interdisciplinary center for the use of neutrons, assembling all instrumental, methodological and scientific expertise for the successful use of the ESS and other major sources, serving as a resource in neutron based science for the whole community; a long term status would require also the association to a new local source of neutrons where users at all levels could practice their skills. To face the future shutdown of the Orphée reactor, the LLB organized a workshop "New Opportunities in Neutron Scattering: Small to Medium Sources and their Applications", in Paris on May 18 – 19, with the active contribution of the Council for Science and Instrumentation (CSI), chaired by I. Anderson (ONRL), providing new perspectives on the medium and long term strategy for the French Neutron Scattering activities within the future European Neutron Scattering Landscape.

Enjoy reading the report on science with neutrons at the LLB!

SONATE Compact Neutron Source

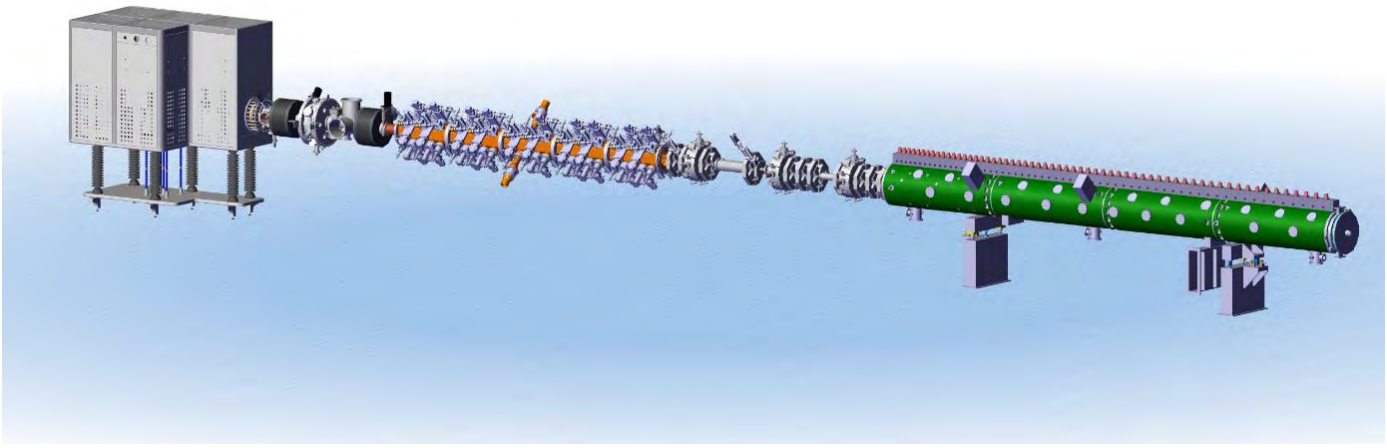

F. Ott[a], A. Menelle[a], X. Fabrèges[a], N. Chauvin[b], J. Schwindling[b], A. Letourneau[b], A. Marchix[b]

a Laboratoire Léon Brillouin, Saclay, France
b CEA/IRFU, Saclay, France

Frederic.ott@cea.fr

Nuclear reactors used to produce neutrons for neutron scattering are progressively being replaced by spallation sources, PSI, ISIS, SNS, JPARC and ESS in the near future. These facilities are however rather expensive, in the 1G€ range. In 2015, the LLB has thus conducted a reflexion on the possibility of building compact neutron sources which would provide a high neutron brilliance while remaining rather inexpensive. It appears that the accelerator technology has made significant progress in the recent decade and is now able to provide high currents of particles (above 100mA). One of the first beneficiary of these new technologies will be ESS which will use an accelerator with a peak current of 60mA.

While spallation sources will always remain expensive due to the length of the accelerator , we have considered an other nuclear reaction, namely *stripping* which is also producing neutrons. When a proton is sent on a light element (e.g. Be or Li), neutrons can be stripped from the nucleus. This reaction takes place at rather low neutron energies (3-100MeV). The trade-off is that while a spallation reaction produces between 10 to 20 neutrons per proton, a stripping reaction produces only 0.01 to 0.1 n/proton. However, a spallation source such as ISIS Target Station 2 is operating at 0.8GeV with a current of 50µA, so that even though the stripping reaction is significantly lower than the spallation reaction by a factor 100 to 1000, this can be compensated by a larger current (100mA) which is 2000 times higher. Besides, due to the much lower proton energy, the target volume can be decreased from 4 litres (in the case of ISIS TS2) down to 2-3 cm^3 so that the brilliance of the source can be significantly increased.

A working group gathering scientists from LLB and IRFU from various fields (accelerators, simulations, neutron optics, neutron scattering) has been formed to evaluate the performances of a neutron source based on the most advanced accelerator technologies. A reference design has been proposed, namely, a source using a 20MeV accelerator with a peak current of 60mA and a duty cycle of 4%. Such a source is readily feasible since it corresponds technically to the first 30m of the ESS accelerator. Within this scenario, the neutron flux has been evaluated by Monte-Carlo simulations for simple moderator designs. The peak flux has been calculated as $4x10^{13}$ n/cm²/s on the moderator surface while the flux in the reactor Orphée is $1.5x10^{14}$ n/cm²/s. Hence the calculated flux are in the same range. The key difference lies in the fact that Orphée is operating is continuous mode while a new source would operate in pulsed mode.

We have then benefited from the work done for the ESS instruments (together with the expertise on some Time-Of-Flight instruments at LLB) to estimate the performances of instruments on such a compact source operating in pulsed mode. We have considered the following instruments, SANS, reflectometer, powder diffractometer, radiography, Time-of-flight inelastic instrument, spin-echo. Figure 1 shows the comparison of a spectrum measured on G41 (on Orphée) and PRESTO (on SONATE). By simply moving G41 on SONATE, the performances would be 0.7 that on Orphée. A simple upgrade of the detector, by replacing it with the 7C2 detector which is covering a larger solid angle and which has a much higher detection efficiency would provide an overall gain of 20. Besides, the operation of a time-of-flight spectrometer on a pulsed

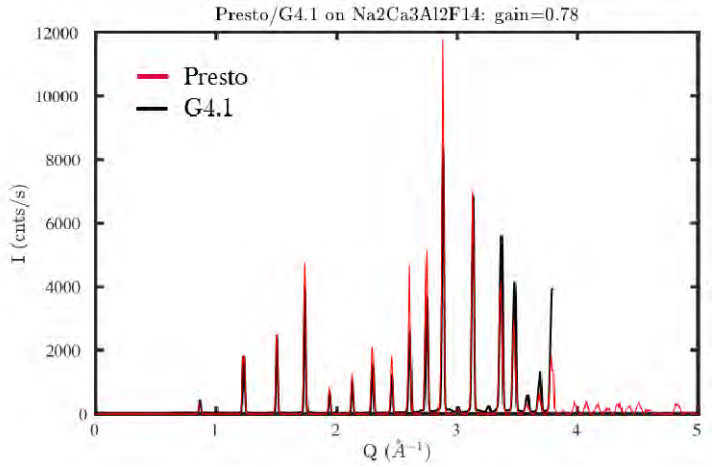

***Figure 1** : Comparison of the Time-Of-Flight spectra measured on $Na_2Ca_3Al_2F_{14}$ on the G41 and on the PRESTO instruments.*

source is way more flexible than on a reactor. While on a reactor, each powder diffractometer is designed to be either high resolution or high flux, on a pulsed source, the resolution can be tuned rather easily by simple shaping the incident pulse with mechanical devices (double disk chopper typically). In any case, these calculations show that a diffraction instrument could efficiently replace the existing powder diffractometers on Orphée .

The table below compares the performances of various instruments types in terms of flux at the sample position. For each instrument types the expected performances are on par with existing instruments which suggest that it would be possible to continue performing the current scientific programs going on in Orphée.

It should however be underlined that different types of instruments operate in optimal conditions for different types of pulse length and repetition rate. For example a high resolution powder instrument has rather different optimal working conditions than a SANS instrument (short pulse with high repetition rate Vs long pulse with slow repetition rate). In the case of ESS, this has led to a weighted compromise between instruments for the source characteristics (14 Hz, with pulses of 3ms). On the other hand, in a compact source, due to the compacity of the moderator, it is likely that only a few instruments (max. 4) could be accommodated around each target. This should be seen as an opportunity since each target could be optimized for a specific family of instruments. Beyond this aspect, the use of smaller accelerator makes the design of such compacts sources both modular and upgradable. New targets may be added over time or the accelerator energy can be increased over the time to increase the neutron production.

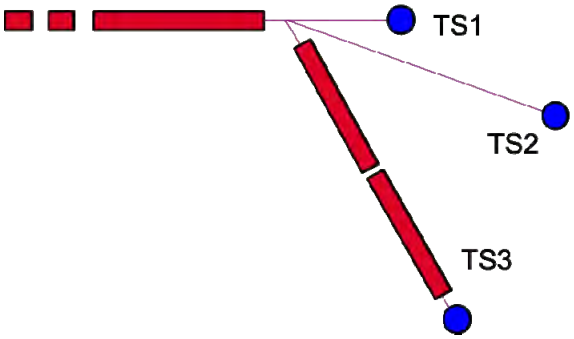

***Figure 2**: Example of a modular architecture. A first target might be optimized for low resolution instruments (SANS, reflectivity). A second target might be built for higher resolution techniques (diffraction). Later on a third target with an increased proton beam (e.g. from 20MeV to 60MeV might be added)*

The first experimental tests will be performed in 2016 on the IPHI accelerator at Saclay in order to validated the Monte-Carlo and GIANT4 simulations.

Technique	**Flux on sample**	**Reference spectrometer**	**Potential gains**
SANS	3.10^5 n/s/cm² (low Q) 10^6 n/s/cm² (med Q) 4.10^6 n/s/cm² (high Q)	PAXE@LLB (med Q) 7.10^5 n/s/cm² SANS2D@ISIS 10^6 n/s/cm² (under construction)	Slit setup x10 Focusing optics for VSANS (small Q) x10
Reflectivity	10^6 n/s/cm²	POLREF@ISIS TS2 10^7 n/s/cm² (under construction)	SELENE concept (x10) Advanced Deconvolution x3
Spin-Echo	1.3 10^6 n/s/cm²	MUSES 2.10^7 n/s/cm² (at 5A°)	Multi-MUSES (x70)
Low resolution powder diffraction	2.10^6 n/s/cm²	G41@LLB 4.10^6 n/s/cm²	Large solid angle detector (7C2 type) x20
TOF	3.10^7 n/s/cm²	OSIRIS@ISIS 3.10^7 n/cm²/s	
Imaging (white beam)short instrument	10^6 n/s/cm² (for L/D = 250) 10^7 n/s/cm² (for L/D = 80)	IMAGINE@LLB 10^7 n/s/cm² ICON@PSI 2.10^7 n/s/cm²	MCP detectors x5 Coded Source Imaging x10
Imaging (time resolved)	10^6 n/s/cm² (for L/D = 250) $d\lambda/\lambda = 2\%$	ICON@PSI 4.10^6n/s/cm² (2%) NEUTRA@PSI 4.10^6n/s/cm² (2%) RADEN@JPARC 2.10^7 n/s/cm² (0.3%)	MCP detectors x5 Coded Source Imaging x10

Scientific Highlights

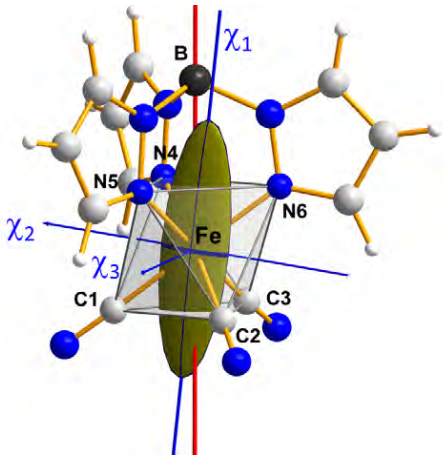

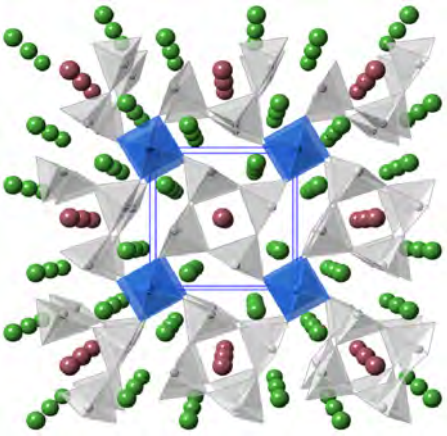

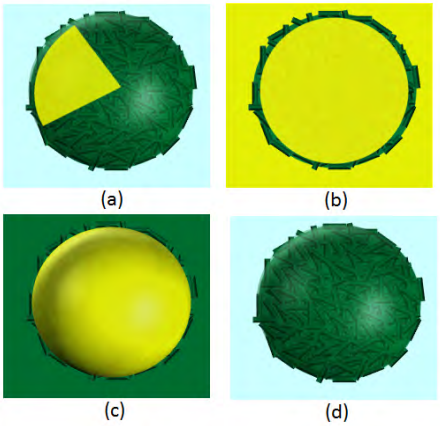

Magnetism and superconductivity

Material and Nanosciences,
Fundamental Studies and Applications

Soft complex matter
and biophysics

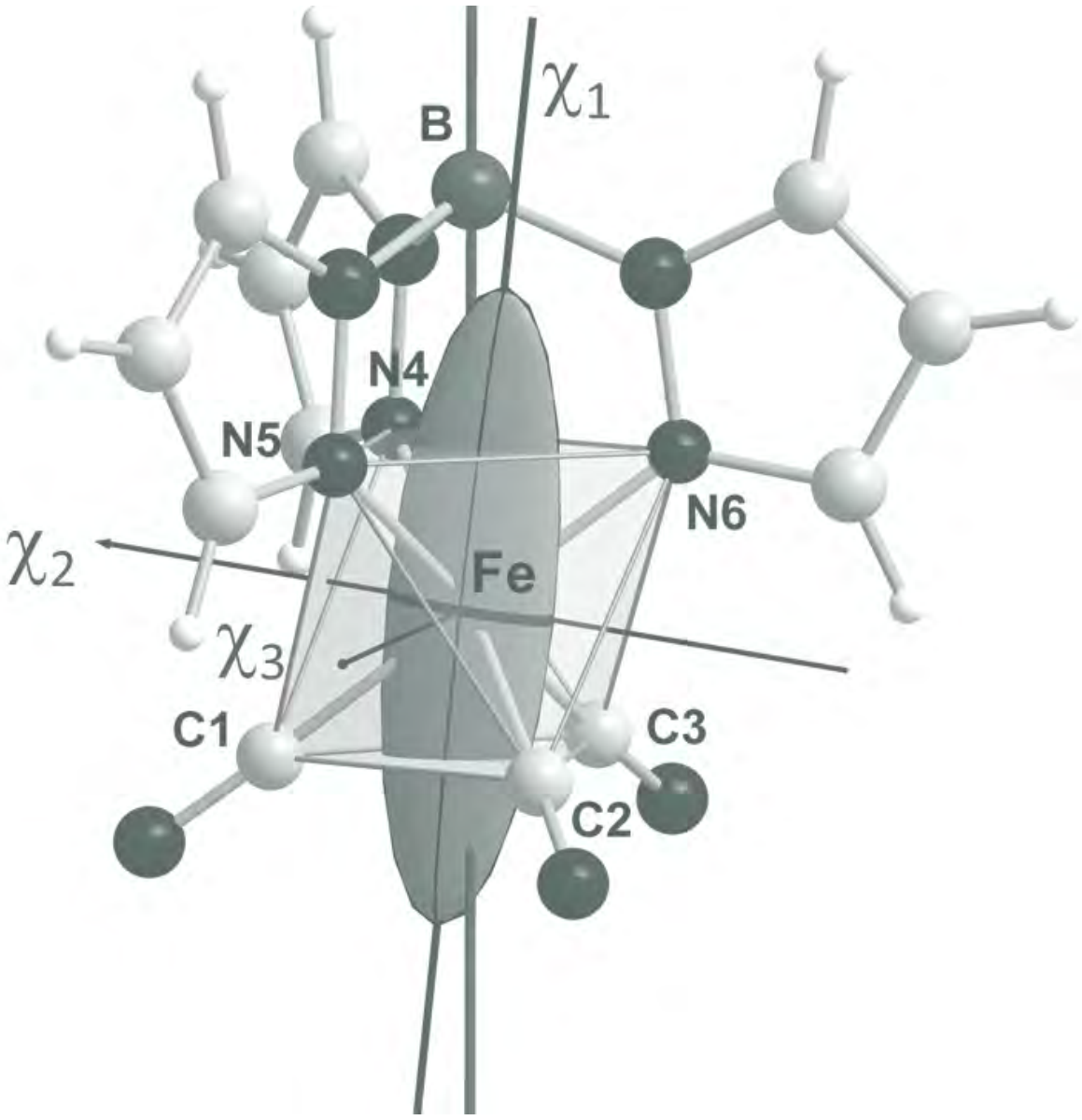
χ1
B
N4
N5
N6
χ2
Fe
χ3
C1
C3
C2

Magnetism and superconductivity

Strongly correlated electron systems are compounds where electron correlations play a crucial role, coupling electronic, magnetic and orbital degrees of freedom, and yielding anomalous,- and potentially useful-, physical properties. The subjects studied at LLB involve unconventional superconductors, quadrupolar orders in heavy fermions, frustrated spin liquids or spin ices, multiferroics, thermoelectrics, chiral and molecular magnets. Studying static and dynamical magnetic correlations through neutron scattering, and investigating precursor states, provide precious clues to understand these anomalous properties.

Various examples of such mechanisms are given in this issue. In FeSe, spin fluctuations are enhanced at the orthorhombic transition, above the onset of superconductivity at T_C, suggesting that they drive both superconductivity and nematicity. In Na-doped $BaFe_2As_2$, the onset of a spin reorientation transition in the orthorhombic phase above T_C suggests that spin orbit coupling and orbital fluctuations are important to mediate the Cooper pair formation. In heavy fermion $Ce_3Pd_{20}Si_2$, the study of quasielastic spin fluctuations give an insight on the propagation vector of the quadrupolar order, uncharacterized before. In $AgCrSe_2$ thermoelectric, the observation of localized Ag^+ vibrations provides a microscopic explanation for the low thermal conductivity. Finally, in a molecular complex, the determination of the local susceptibility tensor yields a test for quantum chemistry methods, aiming at the synthesis of high anisotropy molecules for spintronics and data storage.

Strong interplay between stripe spin fluctuations, nematicity and superconductivity in FeSe

In iron-based superconductors the interactions driving the nematic order (that breaks four-fold rotational symmetry in the iron plane) may also mediate the Cooper pairing. Here, we study FeSe—which exhibits a nematic (orthorhombic) phase transition at T_s=90 K without antiferromagnetic stripe ordering—by neutron scattering, finding substantial spin fluctuations coupled with the nematicity. The magnetic spectral weight in FeSe is found to be comparable to that of the iron arsenides. These results support recent theoretical proposals that both nematicity and superconductivity are driven by spin fluctuations.

Q. Wang[a], Y. Shen[a], B. Pan[a], Y. Hao[a], M. Ma[b], F. Zhou[b], P. Steffens[c], K. Schmalzl[d], T. R. Forrest[e], M. Abdel-Hafiez[f], X. Chen[f], D. A. Chareev[g], A. N. Vasiliev[g], P. Bourges[h], Y. Sidis[h], H. Cao[i], J. Zhao[a]

a State Key Laboratory of Surface Physics and Department of Physics, Fudan University, Shanghai, China.
b Beijing National Laboratory for Condensed Matter Physics, Chinese Academy of Science, Beijing, China
c Institut Laue-Langevin, Grenoble, France
d Juelich Centre for Neutron Science JCNS Forschungszentrum Juelich, Outstation at ILL, Grenoble, France.
e European Synchrotron Radiation Facility, BP 220, 38043 Grenoble Cedex, France
f Center for High Pressure Science and Technology Advanced Research, Shanghai, China.
g Institute of Experimental Mineralogy,Russian Academy of Sciences, Chernogolovka, Moscow District, Russia.
h Laboratoire Léon Brillouin CEA/CNRS UMR 12, Gif sur Yvette, France
i Neutron Scattering Science Division, Oak Ridge National Laboratory, Oak Ridge, Tennessee, USA.

zhaoj@fudan.edu.cn

The iron-chalcogenide compound FeSe (T_c = 8 K), which possesses the simplest crystal structure of all the iron-based superconductors [1], exhibits a variety of exotic properties that are unprecedented for other iron-based superconductors. For example, the T_c of FeSe increases to ~40K under pressure or by ion/molecule intercalation. In addition, the T_c of single-layer FeSe thin film is as high as 100 K, which is vastly superior to other iron-based superconductors. More importantly, unlike most iron-based materials, the tetragonal to orthorhombic structural transition in bulk FeSe is not followed by the stripe magnetic order, that consists of two interpenetrating antiferromagnetic sublattices forming antiparallel ferromagnetic stripes. This provides an excellent opportunity to elucidate the microscopic origin of the nematicity and its interplay with superconductivity. A spin-driven nematicity scenario has been actually proposed [2] where the spin state is expected to break the rotational symmetry of the lattice. However, the absence of stripe magnetic order, as well as recent nuclear magnetic resonance (NMR) measurements [3] that suggested that there were almost no spin fluctuations above T_s in the tetragonal phase, seem to cast doubt on that approach. However NMR probes momentum-integrated spin fluctuations only at very low energies (~0.1 μeV or lower), whereas the momentum dependence of the higher-energy spin fluctuations has yet to be determined. Crucially, it is these spin fluctuations, especially at the energy scale close to the superconducting gap, that are believed to be important in driving both the superconductivity and nematicity. This issue is here addressed by inelastic neutron scattering experiments [4] which probe spin fluctuations over a wide range of momentum and energy.

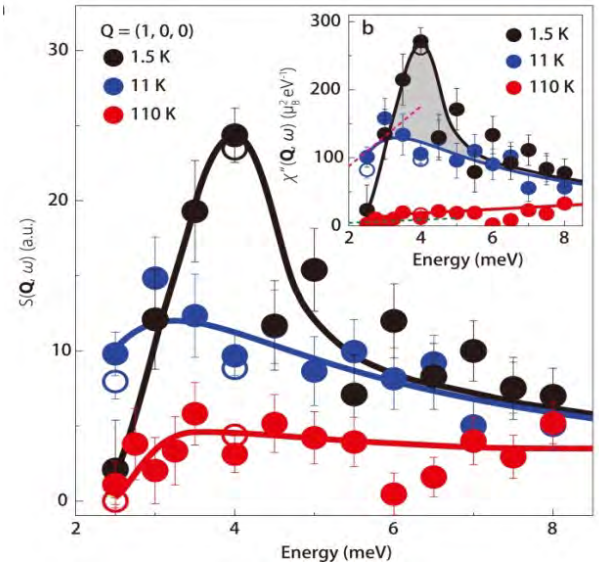

***Figure 1**: Energy dependence of spin fluctuations for FeSe in the superconducting state (T=1.5 K) and normal state (T=11 K and 110 K) [3]. **a**, Energy dependence of the dynamic spin correlation function S(Q,ω) at Q=(1,0,0) after a background correction. The background is measured at Q=(0.944,+/-0.330,0) which are on both sides of the magnetic peak (see ref 3). **b**, Energy dependence of the imaginary part of the dynamic susceptibility. Data are partly from the 2T triple axis at LLB.*

The Figure 1 summarizes the energy dependence of the dynamic spin correlation function S(**Q**,ω) at **Q**=(1, 0, 0) for three temperatures (1.5, 11 and 110 K). The figure shows in the superconducting a sharp resonance mode at around 4 meV above a spin gap (<3meV). The spectral weight loss below the spin gap is compensated by the occurrence of the resonance peak. Moreover, the detailed temperature dependence of the scattering at 4meV shows an order parameter-like behaviour,

which is clearly coupled to the onset of superconductivity (Fig. 2a). The spin resonance mode has been interpreted either as a spin exciton within the superconducting gap, which arises from scattering between portions of the Fermi surface where the superconducting gap function has an opposite sign, or as a broad hump structure induced by an overshoot in the magnetic spectrum above the superconducting gap in a sign-preserving S^{++} pairing state. The sharp mode that we observed here is consistent with the spin exciton model, as the mode energy (4meV) is below the superconducting gap (~5meV). Furthermore, the energy width (~1.2meV) of this mode is essentially resolution limited and much sharper than in other iron-based superconductors. Finally, the resonance energy (E_r=4 meV=5.3k_BT_c) is consistent with the electron boson coupling mode revealed by scanning tunneling spectroscopy, thereby suggesting a strong coupling between the electrons and spin fluctuations. These results are consistent with a spin-fluctuation-mediated sign-changing pairing mechanism, but not with the orbital-fluctuation mediated sign-preserving S^{++}-wave pairing mechanism. The magnetic spectral weight in FeSe is also found to be comparable to that of the iron arsenides.

the spin fluctuations are enhanced abruptly in the orthorhombic phase below T=90 K as shown by a careful study of the temperature dependence of the scattering at 2.5meV (Fig. 2b). Intriguingly, a comparison of that temperature evolution with the orthorhombicity reveals that the enhancement of S(**Q**,ω) is clearly coupled to the development of the nematic (orthorhombic) phase (Fig. 2b). We note that the spin fluctuation enhancement is more pronounced at lower energies (Fig. 1), suggesting a slowing down of spin fluctuations. This indicates that the system is closer to the stripe magnetic ordered state at low temperature. These results are consistent with the recent proposals [2] (based on either itinerant or local moment pictures) that the nematic order is driven by spin fluctuations. In a local moment model where frustrated magnetic interactions drive nematic order in FeSe, the magnetic frustration is lifted by the onset of the orthorhombic distortion, thus causing the system to move towards a stripe ordered phase. As a result the spin fluctuations at the stripe ordering wavevector are enhanced.

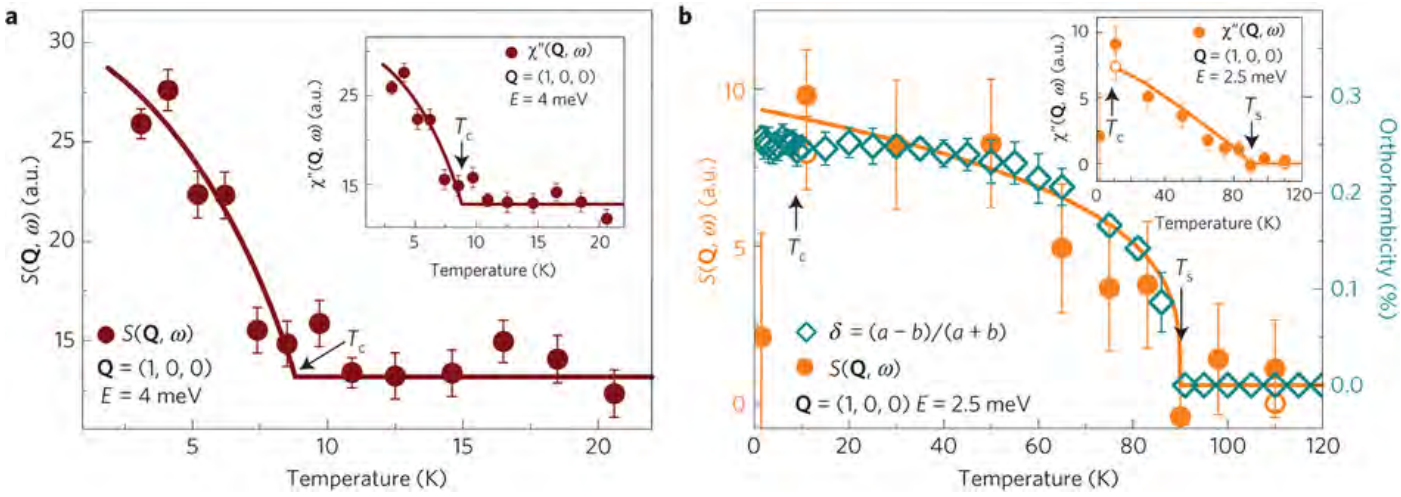

***Figure 2** : Temperature dependence of spin fluctuations in FeSe* [3]. ***a**, Temperature dependence of the dynamic spin correlation S(Q,ω) at E=4 meV, which clearly shows a kink at T_c. The inset shows the temperature evolution of Imχ(Q,ω). **b**, Temperature dependence of S(Q,w) at E=2.5 meV and the orthorhombicity δ(T)=(a-b)=(a+b) shows an order-parameter-like behaviour with an onset at T_s. The orthorhombicity is determined by high-resolution neutron diffraction data on 4F2 at LLB.*

Having established the interplay between the spin fluctuations and superconductivity, we now turn to the impact of nematicity on the spin fluctuations. By contrast with the previous NMR measurements [2], our inelastic neutron scattering measurements show substantial spin fluctuations in the tetragonal phase (T=110 K; Fig. 1). What is more, the energy dependence of the dynamical spin correlation function S(**Q**,w) exhibits a spin-gap-like feature at low energies at T=110K, which is confirmed by a featureless **Q**-scan at 2.5meV [4]. These results agree with a theoretically predicted gapped nematic quantum paramagnetic state, where frustrated magnetic interactions are the driving force of the nematicity and are responsible for the lack of long-range magnetic order in FeSe. This naturally accounts for the absence of low-energy spin fluctuations above T_s suggested by NMR measurements. The most striking observation is that

References

1. *F.-C. Hsu et al. PNAS,* ***105,*** *14262–14264 (2008).*
2. *R.M. Fernandes et al. Nat Phys.* ***10,*** *97-104 (2014).*
3. *S.-H. Baek et al. Nat. Mat.* ***14,*** *210-214 (2015).*
4. *Q. Wang et al., Nature Materials,* ***15*** *159 (2016).*

Spin reorientation transition in Na-doped $BaFe_2As_2$

In iron-based superconductors the most prominent explanation for mediating the Cooper-pair formation in the superconducting state is based on magnetic fluctuations. Therefore the investigation of the magnetic order upon doping is important. Unlike pure or electron doped $BaFe_2As_2$, where the magnetic moments are aligned within the FeAs-layers, we observe for Na-doping a spin reorientation, at which the moments rotate towards an out of layer alignment. This observation documents that spin-orbit coupling and orbital aspects play a crucial role in the magnetic correlations in Fe based superconductors.

F. Waßer[a], A. Schneidewind[b], Y. Sidis[c], S. Wurmehl[d,e], S. Aswartham[d], B. Büchner[d,e], M. Braden[a]

a II. Physikalisches Institut, Universität zu Köln, Germany
b Jülich Centre for Neutron Science, Forschungszentrum Jülich, Outstation at MLZ, Garching, Germany
c Laboratoire Léon Brillouin CEA/CNRS UMR 12, Gif sur Yvette, France
d Leibnitz-Institut für Festkörper- und Werkstoffforschung Dresden, Germany
e Institut für Festkörperphysik, Technische Universität Dresden, Germany

wasser@ph2.uni-koeln.de braden@ph2.uni-koeln.de

Iron-based superconductors (FeSC) are a novel class of high-temperature superconductors, which display close coupling between structural distortion, antiferromagnetism and superconductivity. With increasing charge carrier doping or isovalent substitution superconductivity is induced, while the transition temperatures of the structural distortion and antiferromagnetic order are suppressed in a closely linked fashion [1]. The highest T_cs are located close to the complete suppression of the magnetic order in the corresponding electronic phase diagrams. Therefore, spin fluctuations are the most prominent explanation to mediate the Cooper-pair formation in FeSCs. These materials are composed of $FeAs_4$-tetrahedra, which may be separated by a spacer layer. A typical host compound to study the physics in FeSCs is $BaFe_2As_2$, where the magnetic moments align within the FeAs-layers below T_N, c.f. figure 1.

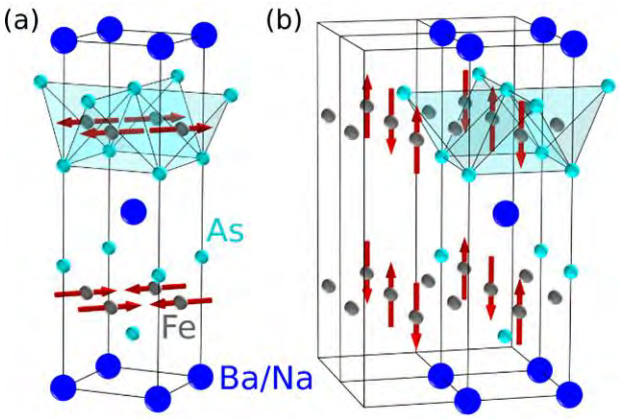

***Figure 1** : (a) Magnetic order below T_N with moments in the FeAs-layers. (b) Magnetic order below T_{reo}, where the moments point out of the FeAs-layers. In a double-Q structure half of the Fe-site are paramagnetic.*

Although, one may think that FeSCs are layered magnets, $BaFe_2As_2$ displays a counterintuitive spin- space anisotropy, because it is easier to rotate the spins out of the FeAs-layers than within [2].

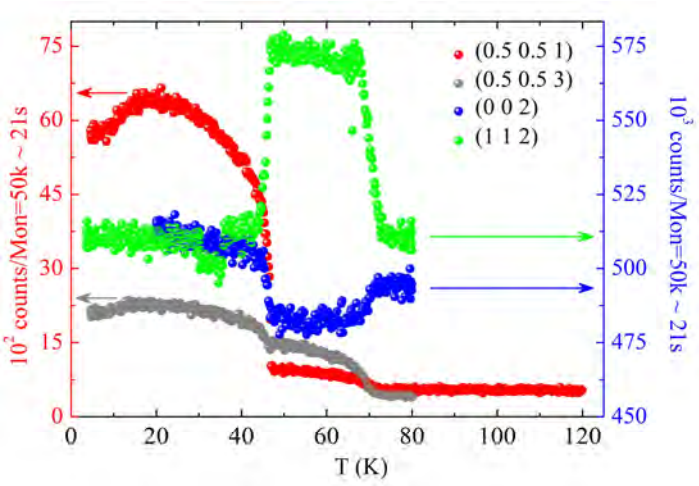

***Figure 2** : Temperature dependence of magnetic and nuclear Bragg reflection intensities in $Ba_{0.65}Na_{0.35}Fe_2As_2$ measured on the PANDA spectrometer. Note that the magnetic, (0.5,0.5,1) and (0.5,0.5,3), and nuclear, (112) and (002), Bragg peaks refer to different scales. (112) and (002) intensities were measured upon heating and cooling, respectively.*

We performed polarised, at 4F1 spectrometer, and unpolarised, at 3T1 and PANDA spectrometers, neutron diffraction experiments on several Na-doped $BaFe_2As_2$ single crystals. For this series a powder neutron diffraction study revealed two magnetic transitions but was unable to fully reveal the characters of the two phases [3]. For 35% Na doping we observed two successive magnetic phase transitions at T_N = 70 K and at T_{reo} = 46 K, which also couple to the structural distortion, c.f. figure 2.

Moreover, the sample enters the superconducting state below 26 K, as it can be seen in the partial suppression of magnetic intensity. Since the intensity of the L=1 and L=3 magnetic Bragg peak at the second magnetic phase transition is interchanged, the L-dependence of the integrated intensities provides information about the spin reorientation. Both magnetic phases can be described by their form factor dependence with respect to their underlying magnetic structure, c.f. figure 3.

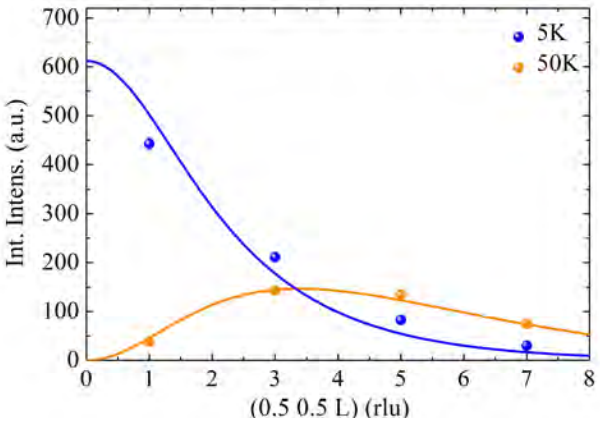

Figure 3 *: L-dependence of the integrated magnetic intensity. At 50 K the moments are aligned within the FeAs-layers, while at 5 K they are rotated towards an out of layer alignment. The lines are fits of the magnetic structure factor with respect to the underlying magnetic order*

As it was previously observed in all FeAs compounds, the ordered moments align within the FeAs-layers at 50 K. However, at 5 K the orientation of the moments is perpendicular to the layers and thus parallel to the *c*-axis [4]. This perfectly resembles the single ion anisotropy of the host compound, where the *c*-axis is the second-softest direction.

The spin-reorientation transition was studied with polarised neutron diffraction, which clearly shows that there is no ordered moment in the transversal in-layer direction and that spins reorient from in-layer longitudinal to out-of-layer. This spin-reorientation transition is coupled to a suppression of the orthorhombic splitting, which suggests a double-Q structure. Neutron diffraction cannot decide between a single- and double -Q structure, but evidence for the latter was recently obtained in Mößbauer studies [5]. In the meanwhile the spin reorientation was also observed in other hole-doped compounds [6, 7], which proves that it is a general feature.

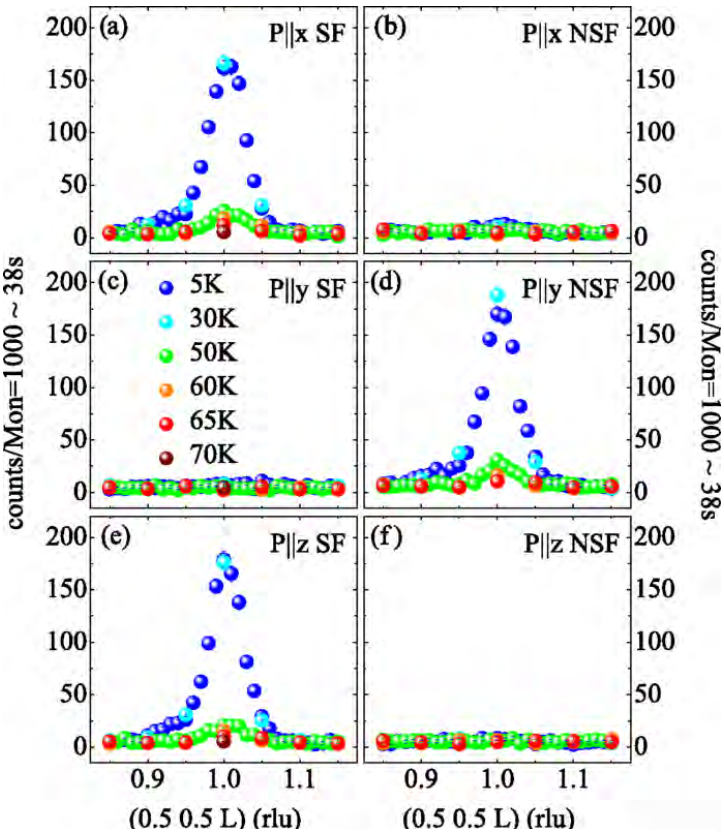

Figure 4 : Results of polarised neutron diffraction experiments on the 4F1 spectrometer. Scans were performed across the (0.5,0.5,1) magnetic Bragg peak in both the SF and NSF channel for the neutron polarisation along the x, y, and z directions. There is no indication of any scattering associated with a magnetic moment pointing in the [1,−1,0] direction.

References

1. *G.R. Steward, Rev. Mod. Phys. 83, 1589 (2011)*
2. *N. Qureshi, P. Steffens, S. Wurmehl, B. Büchner and M. Braden, Phys. Rev. B, 86, 060410(R) (2012)*
3. *S. Avci et al., Nat. Commun 5:3845 (2014)*
4. *F. Waßer, A. Schneidewind, Y. Sidis, S. Wurmehl, S. Aswartham, B. Büchner and M. Braden, Phys. Rev. B, 91, 060505 (R) (2015)*
5. *J. M. Allred et al., nat. phys.* DOI: 10.1038/NPHYS3629 (2016)
6. *A. E. Böhmer et al., Nat. Commun 6:7911 (2015)*
7. *K. M. Taddei et al., Phys. Rev. B, 93, 134510 (2016)*

Momentum-space structure of quasielastic spin fluctuations in $Ce_3Pd_{20}Si_6$

Despite extensive studies, heavy-fermion metals with competing interactions between magnetic and orbital degrees of freedom still attract much attention. Among them $Ce_3Pd_{20}Si_6$ is one of the heaviest-electron systems known to date. The magnetic phase diagram (shown at the right) nearly replicates that of the archetype antiferro-quadrupole (AFQ) order compound CeB_6, though with reduced characteristic temperature and magnetic-field scales, and in a more complex crystal structure consisting of two different, simple-cubic (8c) and face-centered cubic (4a) Ce sublattices. As in CeB_6, the AFM phase in $Ce_3Pd_{20}Si_6$ is surrounded by the AFQ order. We have used high-resolution neutron spectroscopy to observe low-energy magnetic scattering from a single crystal of this compound. Its temperature dependence and distribution in momentum space was investigated using the 4F2 spectrometer. At low temperatures, a quasielastic response persists with varying intensity all over the Brillouin zone and forms a broad hump centered at the (111) scattering vector. With increasing temperature, the energy width of the signal follows the conventional $T^{1/2}$ law. The momentum-space symmetry of the signal suggests that it stems from the simple-cubic Ce 8c sublattice .

P. Y. Portnichenko[a], A. S. Cameron[a], M. A. Surmach[a], P. P. Deen[b,c], S. Paschen[d], A. Prokofiev[d], J.-M. Mignot[e], A. M. Strydom[f], M. T. F. Telling[g,h], A. Podlesnyak[i], D. S. Inosov[a]

a Institut für Festkörperphysik, TU Dresden, Dresden, Gemany
b European Spallation Source ESS AB, Lund, Sweden
c Niels Bohr Institutet, University of Copenhagen, Copenhagen, Denmark
d Institute of Solid State Physics, Vienna University of Technology, Vienna, Austria
e Laboratoire Léon Brillouin CEA/CNRS UMR 12, Gif sur Yvette, France
f Physics Department, University of Johannesburg, Auckland Park, South Africa
g ISIS Facility, Rutherford Apple-ton Laboratory, Chilton, Didcot, Oxon, United Kingdom
h Department of Materials, Uni-versity of Oxford, Parks Road, Oxford, United Kingdom
i Quantum Condensed Matter Division, Oak Ridge National Laboratory, Oak Ridge, USA
Dmytro.Inosov@tu-dresden.de

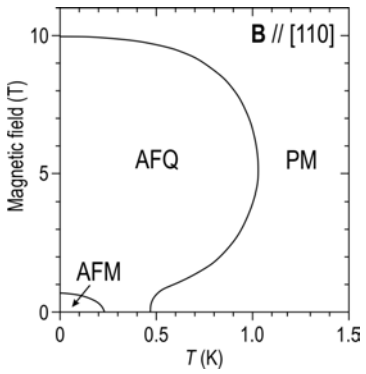

In the best-studied antiferroquadrupolar (AFQ) compound CeB_6, recent studies [1, 2] revealed a pronounced quasielastic magnetic signal centered around the (1/2 1/2 1/2) propagation vector of the elusive magnetically hidden order phase, which is usually attributed to the AFQ ordering. Similarly to CeB_6, the cubic clathrate compound $Ce_3Pd_{20}Si_6$ is a heavy-fermion metal with two successive low-temperature phase transitions in the absence of magnetic field. It exhibits an AFQ phase below T_Q = 0.5 K and an antiferromagnetic (AFM) phase below T_N = 0.31 K [3], whose propagation vector is $\boldsymbol{Q}_{AFM}$ = (0 0 1±δ), with $\delta \approx 1/5$ [4] (figure 1). It is surrounded by the AFQ phase and can be suppressed by a very moderate magnetic field. The structure was shown to result from antiferromagnetic ordering on the simple-cubic 8*c* Ce sublattice [4]. This places

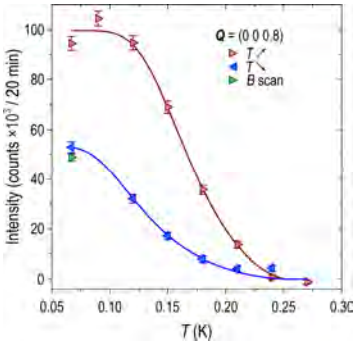

***Figure 1**: Temperature dependence of the AFM Bragg intensity for increasing and decreasing field.*

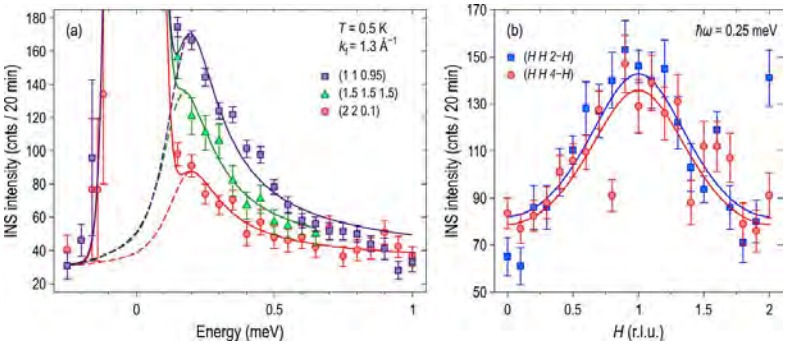

***Figure 2**: (a) Energy dependence of the magnetic scattering measured at several wave vectors. The dashed lines show the magnetic signal without the elastic incoherent scattering contribution. (b) Momentum dependence of the signal along two equivalent trajectories fitted with Lorentzian profiles.*

$Ce_3Pd_{20}Si_6$ very close to a quantum critical point, leading to non-Fermi-liquid behavior and to very high values of the electronic specific-heat coefficient [5]. Previous inelastic neutron scattering (INS) measurements on $Ce_3Pd_{20}Si_6$ have been performed on polycrystalline samples. They revealed a clear crystalline electric field (CEF) line at 3.9 meV and suggested the presence of an additional unresolved low-energy peak centered at 0.31 meV [6]. In the present study, we investigated the low-energy spin dynamics of $Ce_3Pd_{20}Si_6$ using single-crystal INS spectroscopy. To be able to resolve low-energy excitations, a spectrometer with a

good resolution and high flux was required. Additionally we used sub-Kelvin temperatures, and the 4F2 spectrometer available at LLB in combination with a dilution refrigerator perfectly met these criteria.

Figure 2(a) shows INS spectra measured in the paramagnetic state just above T_Q. One sees a quasielastic magnetic scattering (QEMS) below 1 meV, which can be described by a Lorentzian line shape [7]. This signal has a nearly identical energy profile at different wave vectors, but its intensity varies strongly in Q space, excluding a CEF line at 0.31 meV as was suggested in Ref. [8]. Two constant-energy scans measured at 0.25 meV along equivalent Brillouin zone (BZ) diagonals, as presented in figure 2(b), demonstrate a broad Q-space distribution of the quasielastic intensity, peaked at the (111) wave vector. A more complete picture of the quasielastic intensity distribution in Q space is given by figure 3, showing a constant-energy map of the low-temperature QEMS response at 0.25 meV over the entire (*HHL*) scattering plane. From the fact that the quasielastic line shape remains essentially unchanged with Q, as follows from figure 3, we can conclude that such an intensity map is also representative of the total energy-integrated spectral weight distribution in momentum space. It shows a broad anisotropic hump of intensity centered at (111) with weaker side lobes extending along the (110) and (001) directions.

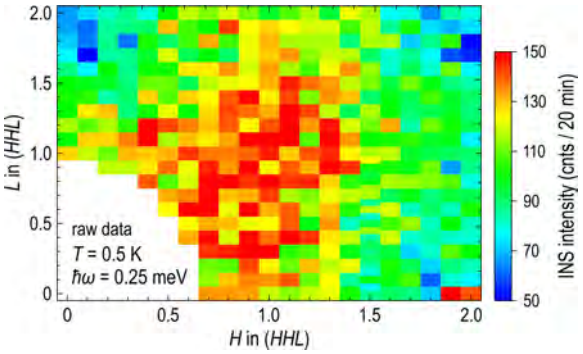

***Figure 3**: Momentum dependence of the low-T QEMS intensity in the (HHL) scattering plane, measured at an energy transfer of 0.25 meV.*

In the large BZ corresponding to the Ce 8c simple-cubic sublattice, this wave vector would coincide with the zone corner (*R* point), matching with the AFQ propagation vector of CeB_6 where a similarly broad local maximum of the QEMS intensity was also found above T_N.

In figure 4 we present the temperature dependence of the QEMS response near its maximum at the (111) wave vector. Here, all but the lowest-temperature datasets were measured in the closed-cycle ^{4}He refrigerator. As this cryostat produced a different background from the one observed with the ^{3}He/^{4}He dilution fridge, the data in figure 4 are plotted after subtraction of the corresponding constant background levels (taken equal for all data measured under the same conditions). Upon warming, we can observe a monotonic suppression and broadening of the quasielastic

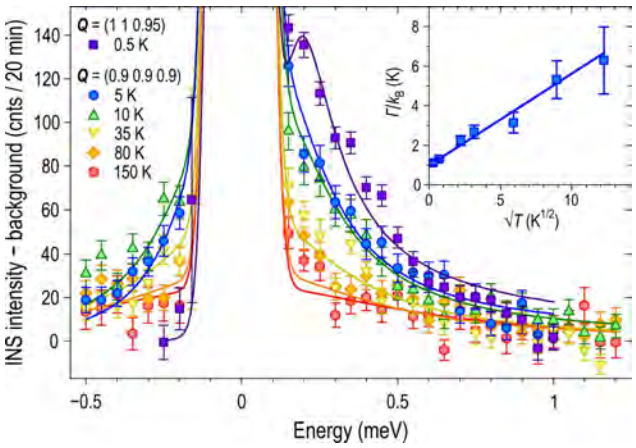

***Figure 4**: Temperature evolution of the background-subtracted QEMS intensity, fitted to the sum of a quasielastic Lorentzian and the incoherent elastic line. The inset shows the T dependence of the normalized quasielastic linewidth.*

signal. The temperature dependence of the quasielastic linewidth $\Gamma(T)$, presented in the inset of figure 4, approximately follows a $T^{1/2}$ law [9] characteristic for Kondo ions, as found previously for a number of Ce compounds in the $T > T_K$ regime [10],

$$\Gamma(T)/k_B = \Gamma_0/k_B + A \cdot T^{1/2}.$$

From the residual width at T = 0, a characteristic Kondo temperature $T_K = \Gamma_0/k_B$ = (0.97 ± 0.07) K can be inferred. The measurements thus show the presence of low-energy dynamical magnetic correlations in the paramagnetic state of $Ce_3Pd_{20}Si_6$. According to their Q-space symmetry, they are associated with the simple-cubic Ce 8c sublattice. This suggests that the remaining Ce 4a ions are magnetically inactive, which could be due to the frustration on the face-centered-cubic sublattice, strong Kondo screening of their magnetic moments, or both. From the presence of strong quasielastic scattering at the BZ corner, which coincides with the propagation vector of the AFQ phase in CeB_6, we may tentatively surmise that the AFQ phase in $Ce_3Pd_{20}Si_6$ also resides at the same wave vector in the large BZ, q_{AFQ} = (111).

References

1. G. Friemel et al., Nature Commun. **3**, 830 (2012).
2. H. Jang et al., Nature Materials **13**, 682–687 (2014).
3. . Custers et al., Nature Materials **11**, 189–194 (2012).
4. Lorenzer K.-A., Ph.D. thesis, Fakultät für Physik, Technischen Universität Wien (2012).
5. N. Takeda et al., J. Phys. Soc. Jpn. **64**, 387–390 (1995).
6. S. Paschen et al., Physica B **403**, 1306 (2008).
7. P. Y. Portnichenko et al., Phys. Rev. B **91**, 094412 (2015).
8. P. P. Deen et al., Phys. Rev. B **81**, 064427 (2010).
9. R. A. Robinson, in Magnetism in Heavy Fermion Systems, edited by H. B. Radousky (World Scientific, Singapore, 2000).
10. N. E. Bickers et al., Phys. Rev. B **36**, 2036 (1987).

Localized Ag^+ vibrations at the origin of ultralow thermal conductivity in layered thermoelectric $AgCrSe_2$

Mostly studied for its superionic conductivity, $AgCrSe_2$ is a naturally layered compound, which achieves very low thermal conductivity at room temperature, and is considered a promising thermoelectric. Here we report low temperature inelastic neutron scattering experiments on $AgCrSe_2$. We observe a very low frequency mode at 3 meV, ascribed to large anharmonic displacements of the Ag^+ ions in the $[Ag]_\infty$ layer. The low thermal conductivity of $AgCrSe_2$ is attributed to acoustic phonon scattering by a regular lattice of Ag^+ ions oscillating in quasi-2D potential wells. These findings highlight a new way to achieve localized phonon modes in a perfectly crystalline solid.

F. Damay[a], S. Petit[a], S. Rols[b], M. Braendlein[a], R. Daou[c], E. Elkaïm[d], F. Fauth[e], F. Gascoin[c], C. Martin[c] and A. Maignan[c]

a Laboratoire Léon Brillouin CEA/CNRS UMR 12, Gif sur Yvette, France
b Institut Laue-Langevin, GRENOBLE CEDEX 9, France
c Laboratoire CRISMAT, CNRS UMR 6508 ENSICAEN, CAEN, France
d Synchrotron Soleil, Saint-Aubin GIF-SUR-YVETTE, France
e Synchrotron ALBA, Carretera BP 1413, 08290 Cerdanyola del Vallès, BARCELONA, Spain

francoise.damay@cea.fr

In materials science, the substructure approach consists in imagining complex materials in which a particular property is associated with a distinct structural feature, so as to combine different chosen physical characteristics which otherwise have little chance to coexist. Applied to the control of charge carrier concentration in Cu-O planes through a charge reservoir layer, it has led to superconductivity, and in thermoelectric materials [1] it has been used to achieve simultaneously low thermal conductivity through specific structural disorder (phonon-glass) and high electric conductivity (electron-crystal).

$AgCrSe_2$ is a naturally layered compound, made of stacked $[Ag]_\infty$ and $[CrSe_2]_\infty$ layers. The Ag^+ ions actually form a pseudo two-dimensional puckered honeycomb lattice made of two interpenetrating triangular sublattices (Figure 1). Below the order-disorder transition temperature T_{OD} = 475 K, only one of these sublattices is fully occupied [2], while above, Ag^+ ions are disordered between both with equal probability, and high *ionic* conductivity is observed. The Cr atoms of the $[CrSe_2]_\infty$ layer bear a spin S = 3/2. Magnetic ordering of the Cr spins is observed [3] below T_N = 55 K, and is characterized by long wavelength antiferromagnetic cycloids.

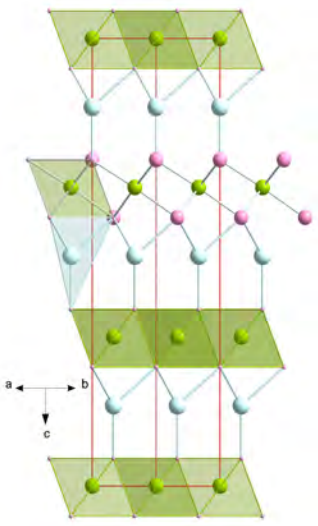

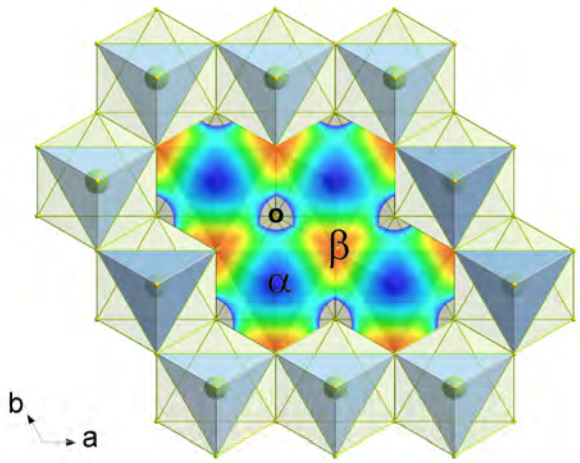

***Figure 1** : (left) R3m crystal structure of $AgCrSe_2$. Ag, Cr and Se atoms are drawn in light blue, green and pink, respectively. Coordination polyhedra, octahedral for Cr and tetrahedral for Ag, are shown. (right) Compact $CrSe_2$ layer on which is superimposed the energy map of the effective potential surrounding Ag^+ in its tetrahedron. O indicates octahedral (empty) sites. α and β label the two Ag^+ triangular sublattices, full and empty, respectively, in the R3m structure.*

$AgCrSe_2$ was revisited recently for its thermoelectric properties above room temperature [4] : above T_{OD}, its *thermal* conductivity is extremely low (~ 0.2-0.5 $W.K^{-1}.m^{-1}$) and nearly temperature independent, a fact related to the disordering of the silver layer.

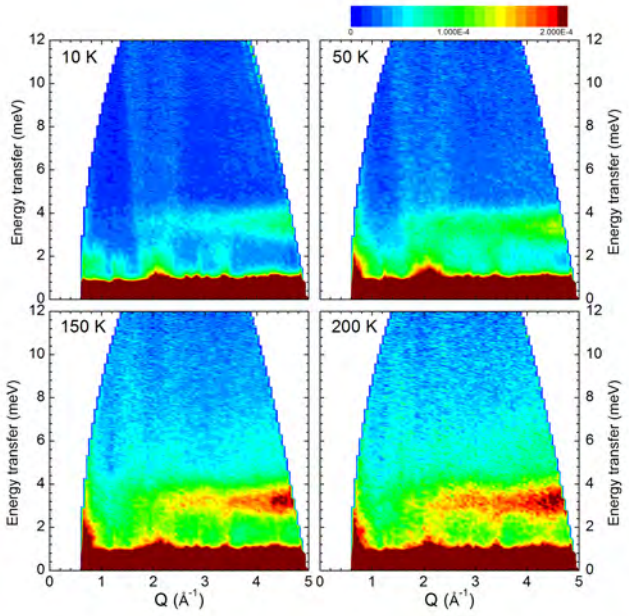

***Figure 2** : Temperature evolution of the inelastic neutron scattering powder spectrum of $AgCrSe_2$, showing the localized lattice mode at 3.3 meV (IN4@ILL time-of-flight data, λ_i = 2.2 Å). The dispersive signal at Q = 2 Å^{-1} is of magnetic origin.*

Below T_{OD}, i.e., in the ordered state, the thermal conductivity of $AgCrSe_2$ still remains extremely low. To investigate in more details this intriguing property, inelastic neutron scattering experiments [5] were performed between 10 K and 200 K, as illustrated on Figure 2. Over the whole temperature range, the main feature of the excitation spectra is clearly a non-dispersive inelastic signal near 3.3 meV. The increasing intensity of this excitation when temperature increases is characteristic of a bosonic mode. Its existence up to room temperature attests that it is a lattice vibrational mode, while the lack of dispersion shows its localized character. In parallel, Rietveld refinement of synchrotron diffraction data at 300 K show that the atomic motion of Ag^+ is anomalously large and strongly anisotropic, confined within the *ab* plane. Ab-initio molecular dynamics (AIMD) calculations indicate in addition that the main contribution to the 3.3 meV intensity comes from Ag^+ vibrations within the *ab* plane. This result confirms therefore that the 3 meV mode in $AgCrSe_2$ originates from vibrations of the loosely bound silver ions, parallel to the triangular planes. This motion is increasingly anharmonic as temperature increases and nears the order-disorder transition T_{OD}. Accordingly, AIMD results show that at the temperature of the simulation T = 150 K, some Ag^+ ions still perform jumps between adjacent positions in the same layer, in contrast with the Cr and Se atoms, whose displacement clouds are localized around equilibrium positions.

The low value of the thermal conductivity in $AgCrSe_2$ indicates that the phonon mean free path in this compound is extremely short, even below the order-disorder transition. Because the heat carrying phonons are the long-wavelength (or low energy) ones, efficient phonon scattering can be expected from the interaction between acoustic phonons and the 3 meV mode characterizing the Ag^+ vibration, and can be considered as a plausible explanation to account for the low thermal conductivity of $AgCrSe_2$. This low energy mode actually appears to be an intrinsic feature of the tetrahedral sites in this structural type, as it has been reported for other isostructural compounds. Further first-principle studies would be necessary to apprehend the acoustic phonon scattering mechanism induced by an array of anharmonic potentials, and how it compares with the mechanism based on a wideband three-phonon scattering process proposed for rattlers in clathrates, which leads to a severe reduction of the acoustic phonon average relaxation time, rather than of their velocity.

References

*1. G. J. Snyder and E. S. Toberer, Nature Materials **7**, 105 (2008).*

*2. A. Van der Lee and G.A. Wiegers, J. Solid State Chem. **82**, 216 (1989).*

*3. P. F. Bongers, C. VanBrugg, J. Koopstra, W. P. F. Omloo, G. A. Wiegers and F. Jellinek, J. Phys. Chem. Solids **29**, 977 (1968).*

*4. A. Maignan, E. Guilmeau, F. Gascoin, Y. Breard, and V. Hardy, Science and Technology of Advanced Materials **13**, 053003 (2012)*

*5. F. Damay, S. Petit, S. Rols, M. Braendlein, R. Daou, E. Elkaïm, F. Fauth, F. Gascoin, C. Martin and A. Maignan, Sci. Rep. **6**, 23415 (2016).*

Magnetic anisotropy mapping in molecular materials

In order to reach ultimate level of integration at the nanoscale, new molecular materials are developed for data storage and spintronics. One of the properties being required for such molecular systems is a strong magnetic anisotropy. It is therefore essential to understand how to control and predict the magnetic anisotropy for a better rationalization of advanced molecular materials. Here we show that Polarized Neutron Diffraction (PND) permits to correlate in a direct way the local magnetic anisotropy with the molecular structure and therefore provides a crucial test of quantum chemistry (QC) methods for predicting the magnetic anisotropy of molecular complexes.

K. Ridier,[a] A. Mondal,[b] C. Boilleau,[c] O. Cador,[c] B. Gillon,[a] G. Chaboussant,[a] B. Le Guennic,[c] K. Costuas,[c] R. Lescouëzec[b]

a Laboratoire Léon Brillouin, UMR 12, CEA-CNRS, France
b Institut Parisien de Chimie Moléculaire (IPCM), UMR8232, Université Pierre et Marie Curie (UPMC)
c Institut des Sciences Chimiques de Rennes, UMR6226, Rennes.

beatrice.gillon@cea.fr

The synthesis of the so-called SMMs (Single Molecule Magnets) in the nineties has paved the way for future applications in high-density data storage. SMMs behave like a magnet, i.e. possess a remnant magnetization, at the molecular scale. SMMs are generally polynuclear complexes of transition metal ions built from anisotropic molecular precursors. The archetype of such compounds is Mn_{12} [1] for which the quantum tunneling effect of the magnetization was first evidenced (Figure 1).

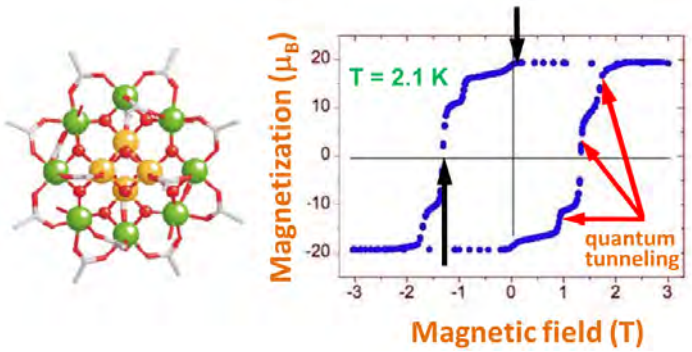

Figure 1: *Mn_{12} molecule and hysteresis cycle at 2.1 K from [2]. Remnant magnetization and coercive field are indicated by black arrows*

The relaxation time of the remnant magnetization at zero field depends on the magnetic moment (S) and the axial magnetic anisotropy (D) which must be as large as possible. However this behavior was observed until now at low temperature only (below 10K). It has been shown that the increase of the working temperature is critically linked to the increase of the magnetic anisotropy. The challenge for the chemists is then to understand how to geometrically combine local magnetic anisotropies of the molecular building blocks in order to obtain the highest axial magnetic anisotropy as possible for the SMM candidate.

Only few experimental techniques are available for establishing magneto-structural relationships, on single crystals: angle-resolved magnetometry, torque magnetometry, Electron Paramagnetic Resonance (EPR) which provides the hyperfine tensors (g) or X-ray magnetic circular dichroism (XMCD) which gives access to the local magnetic moments. However these techniques present some restrictions on the crystalline symmetry and require a preliminary knowledge of the precise orientation of the crystal. Polarized neutron diffraction (PND) has the advantage to contain both structural and magnetic information and therefore provides a unique and direct experimental determination of magneto-structural correlations in paramagnetic complexes.

In this seminal study we have selected the mononuclear low-spin (LS) *fac*-$[Fe^{III}(L)(CN)_3]$ building block (L is a ligand of the Tp family, with Tp=tris(pyrazolyl)borate) which has been widely used to synthesize functional magnetic materials [3]. This complex possess a S = 1/2 spin ground state, with a first order orbital magnetic momentum and a distorted octahedral symmetry. The monoclinic crystal structure of the $PPh_4[Fe^{III}\text{-}(Tp)(CN)_3]\cdot H_2O$ compound exhibits two different molecular orientations in the unit cell. PND data collections were performed at low temperature in the paramagnetic state for three orthogonal directions of the applied field, moderate enough to ensure a linear magnetization regime.

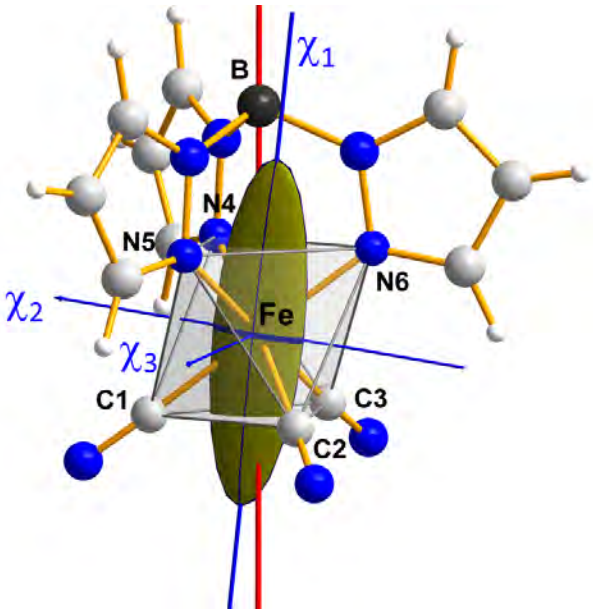

***Figure 2**: Local susceptibility tensor of the Fe^{III} ion (in green) in the $Fe(Tp)(CN)_3^-$ complex. The local magnetic axes χ_i are reported in blue and the direction Fe-B is in red.*

The local susceptibility tensor of the Fe^{III} ion was determined from the PND data thanks to the previously developed approach [4]. The associated magnetic ellipsoid is drawn in Figure 2, which directly evidences the correlation between the Fe^{III} local easy magnetization axis and the direction of the Fe-B bond, which is a trigonal pseudo-axis of the complex (in red). Figure 3 displays the respective orientation of the molecular tensors in the monoclinic cell, a information that cannot be provided by other techniques like magnetometry or EPR.

The confrontation between theoretical calculations and PND observations shows that it is necessary to use sophisticated ab initio methods (CASSCF/SO-SI/PT2) to obtain a reliable prediction of the local anisotropy directions. Both prediction and observation agree with the conclusion: the magnetic anisotropy of the fac-$[Fe^{III}(Tp)(CN)_3]^-$ complex is governed by the trigonal elongation axis of the Fe^{III} coordination octahedron.

We demonstrate here that PND gives access to the local magnetic principal directions, as well as the associated susceptibility values, regardless of the complexity of the crystal structure. This work opens new perspectives in the field of molecular magnetism for a better understanding of magnetic anisotropy and, in particular, with the aim of determining the structural and chemical characteristics, which induce a strong molecular anisotropy for the rational synthesis of functional magnetic materials.

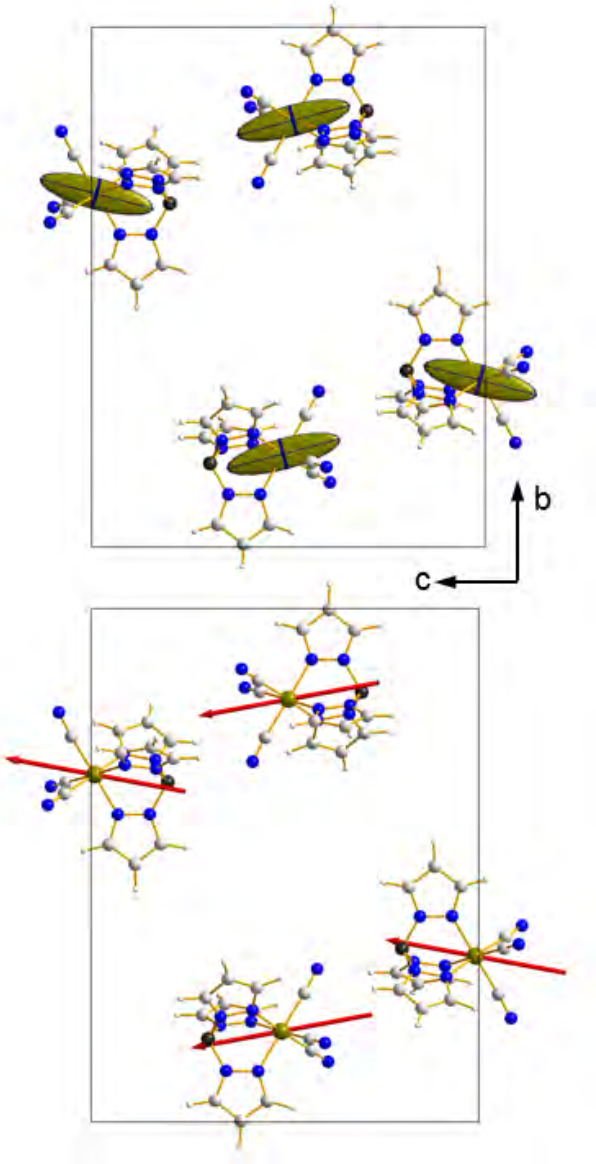

***Figure 3**: Projection of the cell along the a-axis. Top: magnetic ellipsoids from PND; bottom: theoretical component g_z of the hyperfine tensor from ab initio calculations*

References

*1. R. Sessoli, D. Gatteschi, A. Caneschi, M. A. Novak, Nature **365**, 141-143, 1993.*
*2. M. Verdaguer, A. Bleuzen, R. Lescouëzec, V. Marvaud, C. Train, L'actualité chimique **290-291**, 45, 2005.*
*3. K. Ridier, A. Mondal, C. Boilleau, O. Cador, B. Gillon, G. Chaboussant, B. Le Guennic, K. Costuas, R. Lescouëzec, Angew. Chem. **55**, 3963–3967, 2016.*
*4. A. Gukasov and P.J. Brown, J. Phys.: Condens. Matter **14**, 8831–8839, 2002.*

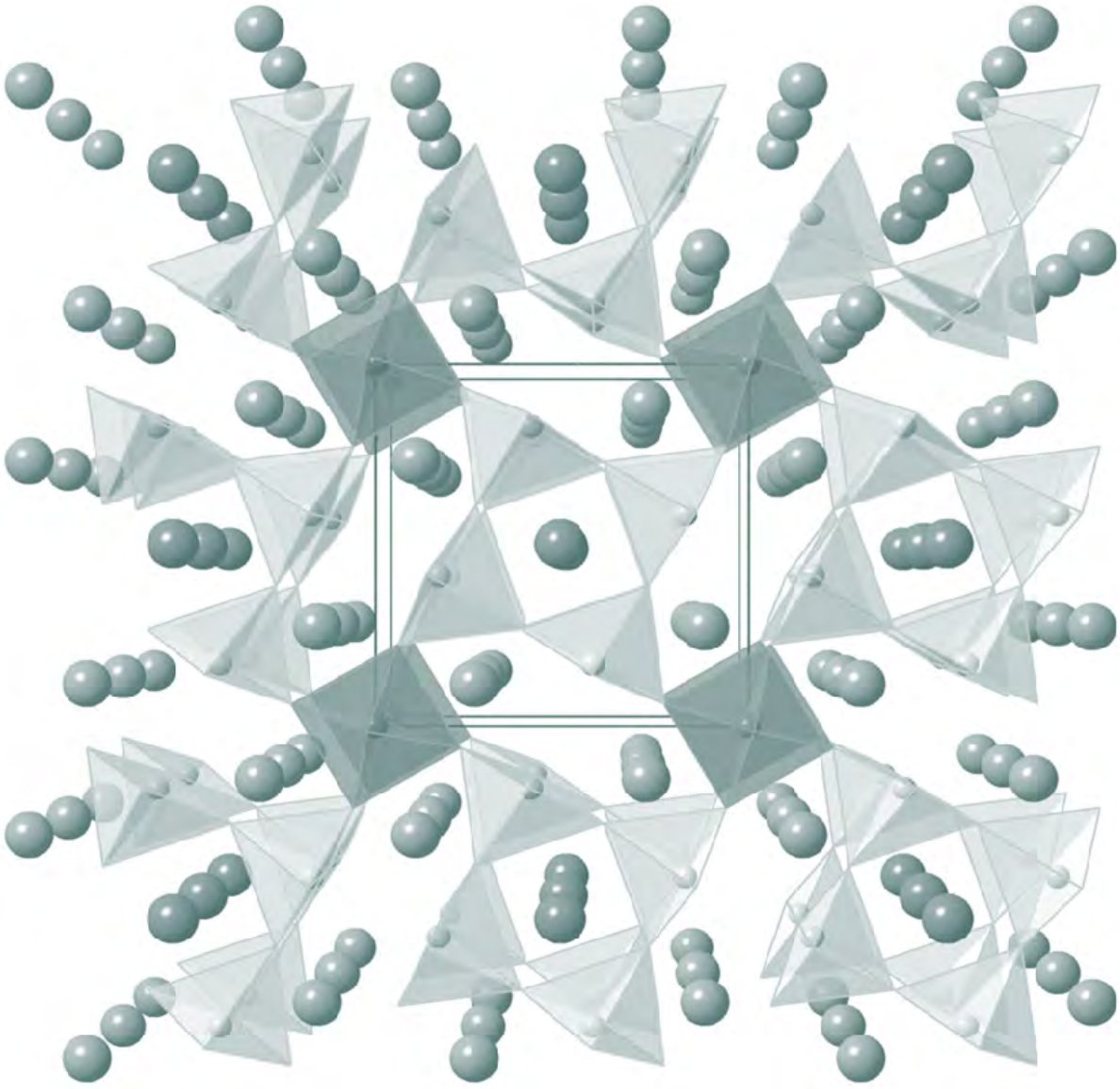

Material and Nanosciences, Fundamental Studies and Applications

Materials Science activity at the LLB covers a variety of research fields including metals, alloys, polymers, geological materials, nanocomposites, organic materials, thin films... They are at the frontier of chemistry, physics and engineering sciences. The objectives of these studies are to understand and predict how parameters such as the chemical composition, the atomic structure and the microstructure determine the properties measured in materials at the macroscopic scale. Most of these studies have direct applications in technology and industry. Neutron scattering provides a wide range of tools, unique to perform such studies:

Neutron diffraction to study either the local order in materials such as glasses or diffraction to probe long range order. This is illustrated in the case of metallic glasses.

Small Angle Neutron Scattering (SANS) and reflectometry are key tools to study materials at the nanoscale: thin films, precipitates, pores, cavities, meso and nano porous structure…, ranging in size between 1 and 100 nm. This was used to probe the fractal structure of graphite over a ultra-wide range of length-scales.

Texture and strain scanning: the strong penetration of the neutrons allows an analysis in volume, and thus to obtain information representative of the whole materials.

Neutron radiography and tomography is used to probe in-situ the evolution or operation of systems. It is mostly sensitive to hydrogenated materials. It proves especially useful in the in-situ control of fuel cells operation.

- **Bringing to light hidden long-range solid-like correlations in the liquid state**
  P. Kahl, P. Baroni, J.F. Bardeau, L. Noirez
- **Thermal stability and TEC of $La_4BaCu_3Co_2O_{13+\delta}$ compound**
  M.V. Sandoval, M.A. Macías, L. Suescun, P. Roussel, F. Porcher and G. Gauthier
- **Characterization of water management in a micro fuel cell using in plane neutron radiography**
  E. Coz, J.Théry, P.Boillat, V.Faucheux, D. Alincant, P. Capron, G. Gébel
- **Atomic structure and formation of CuZrAl bulk metallic glasses and composites**
  I. Kabana, P. Jóvári, B. Escher, D.T. Tran, G. Svensson, M.A. Webb, T.Z. Regier, V. Kokotin, B. Beuneu, T. Gemming, J. Eckert
- **From nanopores to macropores: Fractal morphology of graphite**
  Zhou Zhou, Wim G. Bouwman, Henk Schut, Sylvain Desert, Jacques Jestin, Stefan Hartmann, Catherine Pappas

Bringing to light hidden long-range solid-like correlations in the liquid state

A liquid behaviour is identified by its irreversible deformation (flow behaviour) while the solid-like behaviour is characterized by a linear, reversible response. Today a series of experiments carried out at the mesoscopic-scale, seems to indicate that liquids possess in addition to bulk elasticity, shear elasticity at low frequency. On the assumption of elastic intermolecular correlations, the liquid phase of ordinary liquid crystals is used to highlight this elastic field. A low frequency optical birefringence is revealed in the isotropic phase proving that this so far little interest phase can behave elastically and works as a low frequency optical oscillator, a property unknown in physics of liquids.

P. Kahl[a], P. Baroni[a], J.F. Bardeau[b], L. Noirez[a]

a Laboratoire Léon Brillouin CEA/CNRS UMR 12, Gif sur Yvette, France

b Institut des Molécules et Matériaux du Mans, UMR6283, Université du Maine, Le Mans, France

laurence.noirez@cea.fr

On the basis of a Maxwell gas model (1867), it has long been suspected that liquids exhibit shear-elasticity at sufficiently high solicitation frequencies (MHz or GHz) only. Recent experimental improvements carried out at the Laboratoire Léon Brillouin, indicate that liquids exhibit also shear elasticity at very low frequency (typically below 0.1 to 10Hz). This property is of utmost importance since it means that liquids possess a finite elastic threshold below which they are solid-like. The elastic property has been identified at sub-millimeter scale, both on simple liquids and complex fluids (polymer melts, molecular glass formers, Van der Waals liquids, ionic liquids, H-bond liquids) pointing out the generic characteristic [1-6]. This solid-like property invalidates the single molecular approach of the viscoelasticity. It implies that molecules in the liquid state may not be dynamically free but long range elastically correlated.

The observation of low frequency shear elasticity can be equally made in the isotropic phase of liquid crystals [6-8]. Above a first order transition, the isotropic phase is an ordinary liquid following the crystallography, rheology or thermodynamic criteria. But this liquid presents a specific interest since pretransitional fluctuations, which are clusters of pre-oriented molecules, persist above the clearing point and coexist with the isotropic liquid. Using the birefringent properties of these swarms as a probe, we show that it is possible to visualize the "hidden" shear-elastic correlations. For the first time, a synchronized birefringent optical response in the isotropic phase is highlighted at frequencies as low as 0.01 Hz and at temperatures far away from any phase transition [8-9] (figure 1). The low-

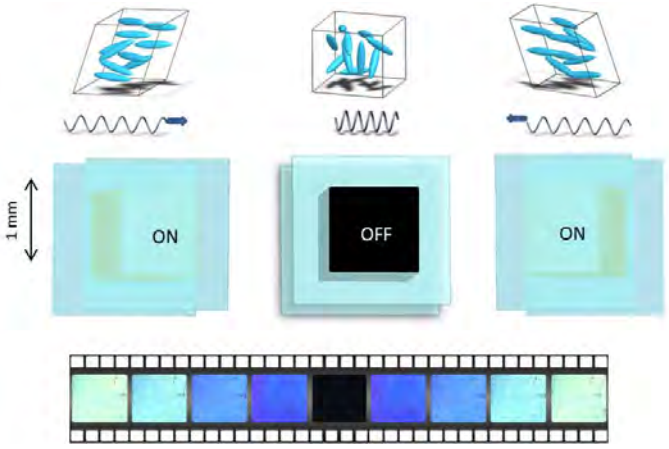

Figure 1*: Assuming long range elastic correlations in the liquid state, for the first time a low frequency synchronized optical birefringence is observed in the isotropic phase of liquid crystals. The photographs show that the liquid under stretching reversibly transits from a black to a bright state, revealing an elastic behaviour (snapshots recorded on a 250µm thick sample between crossed polarizers with a polychromatic light for a period of 0.5 Hz and 10 % strain amplitude. At rest, the isotropic liquid appears black.*

frequency birefringence exhibits a strain dependence similar to the shear elasticity; the optical signal is in-phase at low strain amplitudes in agreement with an elastic response while it is $\pi/2$ phase-shifted at larger strain amplitudes similarly to a viscous signal (figure 2). This birefringent response is strong, defect-free, reversible and points out a collective effect and a long-range ordering (see figure) which is confirmed by wide-angle scattering analysis [10].

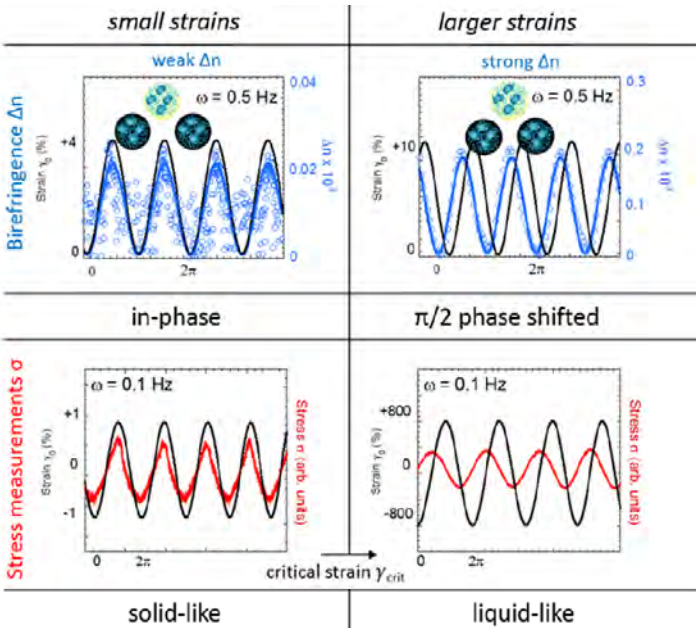

***Figure 2**: Analogous low frequency stress and optical behaviours highlighted in the liquid phase of liquid crystals:*

- *At small strain amplitudes, both stress and optical waves are in-phase with the applied shear-strain. The behaviour is solid-like (elastic response).*
- *Above a critical strain amplitude, the elastic behaviour is converted in a π/2 phase shifted behaviour. The π/2 stress behaviour indicates a viscous flow behaviour while the optical birefringence tells that a long-range ordering is established. Viscous-like and π/2 shifted optical behaviours are interpreted as resulting from a non-linear state of the shear elasticity. Data recorded in the isotropic phase of a liquid crystal at +1 °C above the transition [8].*

This ordering rules out the condition of a low frequency viscous state and its synchronized response highlights the existence of elastic solid-like correlations.

The identification of an optical signal, harmonic with the shear strain, is opposite to a flow (dissipative) behaviour but indicates a partial conservation of the momentum transfer at low frequency; i.e. the persistence of long range collective interactions. The shear elasticity gives rise asymptotically (at large strain or large scales) to flow birefringence and to the conventional viscoelastic behaviour. Rare theoretical developments consider long range continuum in the liquid state [11] or can predict the shear modulus and its scale-length dependence [12].

The shear elasticity is usually hidden in conventional viscoelastic measurements since a narrow gap and a strong wetting are required to reinforce the interactions between the molecules and the substrate. It is facilitated by increasing the surface energy as mica [3], treated quartz surfaces [4] or zero-porosity alumina [5-7]. In the last wetting conditions are reached (top inset Fig.3). The wetting mechanisms are hardly understood at the nanoscale. The attraction potential between the molecules of the liquid and the atoms at the solid wall is deeply modified without inducing structural or chemical change (Fig.3).

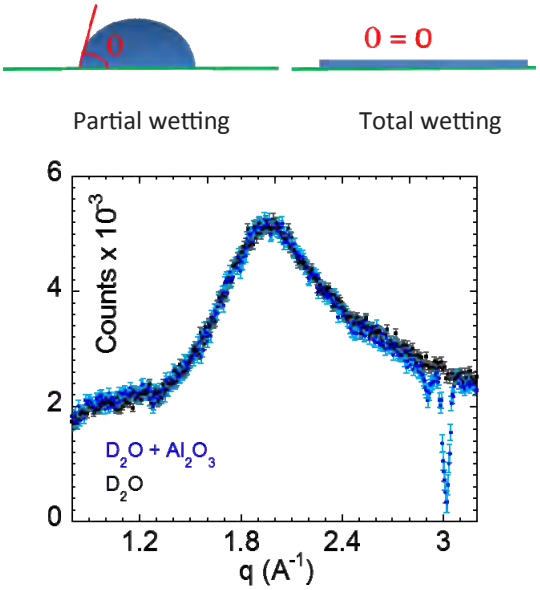

***Figure 3**: Top: Differences between partial and total wetting. Bottom: First correlation peak of liquid D_2O, in bulk and saturated with Alumina powder. The invariance indicates that the powder does not interact structurally or chemically with the liquid (3T1 spectrometer).*

References

1. *B.V. Derjaguin, U. B. Bazaron, Kh. D. Lamazhapova, B. D. Tsidypov, PRA **42**, 2255 (1990)*
2. *M. L. Gee, P. M. McGuiggan, J.N. Israelachvili, J. Chem. Phys **93**, 1895 (1990)*
3. *H.-W. Hu, S. Granick, Science **258**, 1339 (1992)*
4. *D. Collin, P. Martinoty, Physica A **320**, 235 (2003)*
5. *H. Mendil, P. Baroni, L. Noirez, The European Physical Journal E **19**, 77 (2005)*
6. *L. Noirez, P. Baroni, J. of Physics: Condensed Matter **24**, 372101 (2012)*
7. *P. Kahl, P. Baroni, L. Noirez, Phys Rev E **88**, 50501 (2013)*
8. *P. Kahl, P. Baroni, L. Noirez, Appl. Phys. Lett. **107**, 084101 (2015)*
9. *P. Kahl, P. Baroni, L. Noirez, PloS ONE **11** (2016) DOI: 10.1371/journal.pone.0147914*
10. *in preparation*
11. *A.V. Granato, Materials Science and Engineering A **521**: 6-11 (2009)*
12. *F. Volino F. Théorie visco-élastique non-extensive, Annales de Physique, **22** n°1 & 2 (1997)*

Thermal stability and TEC of $La_4BaCu_3Co_2O_{13+\delta}$ compound

Solid Oxide Fuel Cells (SOFC) are energy generation devices that convert chemical energy of fuels, such as hydrogen or methane, into electricity without combustion processes. In comparison with other energy sources, SOFCs reduce the emission of greenhouse effect gases such as CO_2, one of the principal sources of global warming. It is of current interest to develop new SOFC systems that could operate at lower temperature, the so-called Intermediate Temperature SOFCs (IT-SOFC). This has driven researchers to explore new electrocatalysts with high chemical activity and thermomechanical stability. With this purpose, we present a neutron diffraction study of $La_4BaCu_3Co_2O_{13+\delta}$, carried out between room temperature and 850°C, that aims to evaluate the thermal stability and the evolution of oxygen content, the latter being related to electrochemical properties.

M.V. Sandoval[a], M.A. Macías[a,b*], L. Suescun[b], P. Roussel[c], F. Porcher[d] and G. Gauthier[a*]

a Universidad Industrial de Santander, INTERFASE, Bucaramanga, Colombia.

b Universidad de la República, Facultad de Química, Cryssmat-Lab/Cátedra de Física/DETEMA, Montevideo, Uruguay.

c Université de Lille, CNRS UMR 8181, Unité de Catalyse et Chimie du Solide (UCCS), ENSCL, Lille, France.

d Laboratoire Léon Brillouin CEA/CNRS UMR 12, Gif sur Yvette, France

mariomacias@fq.edu.uy *gilgau@uis.edu.co*

Solid Oxide Fuel Cells (SOFC) are considered an important and efficient alternative energy source. Considering that the state of the art electrolyte materials, Gd_2O_3 and Sm_2O_3 doped CeO_2 (CGO and CSO) is known for showing adequate ionic conductivity at temperatures as low as 600°C, current research efforts are focused on lowering the operation of SOFCs to the so-called Intermediate Temperature range (600-800°C). Aiming to developed new compatible materials, we have studied $La_4BaCu_{5-x}Co_xO_{13+\delta}$ compounds, interesting members of the Co-doped cuprate family with an oxygen-vacancy-ordered perovskite structure.

In order to evaluate its thermal stability and study oxygen behavior regarding to vacancy filling and mobility to use it as cathode material for IT-SOFCs, the mixed Cu/Co (3:2) composition was studied in a thermodiffraction experiment. The main structural feature in this oxygen-deficient perovskite is the presence of tunnels associated with the existence of vacancies, which are organized around the mixed-valent Cu/Co ions coordinated in square-based pyramids (Fig. 1).

$La_4BaCu_3Co_2O_{13+\delta}$ compound was synthesized by a modified Pechini route with final sintering temperature at 950°C in air for 5 hours [1]. Thermodiffraction experiments were carried out in air from room temperature to 850°C (5°C/min) on the High Resolution Powder Diffractometer 3T2 using λ= 1.225Å over the 2θ range from 3° to 120°and a step size of 0.05° at the LLB, Saclay, France. The data analysis was performed by the Rietveld method using the Jana-2006 program [2].

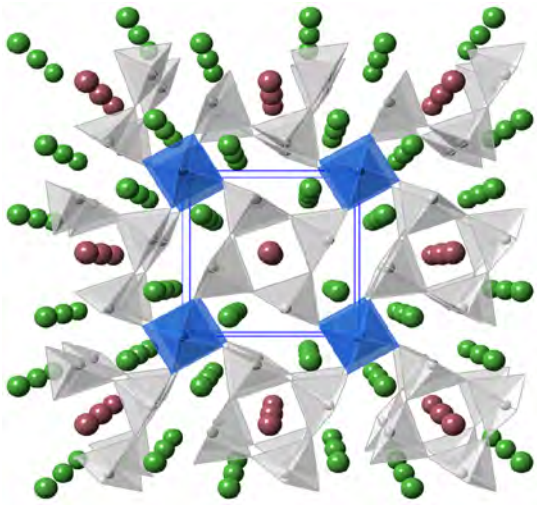

***Figure 1**: Graphical representation along [001] of the $La_4BaCu_3Co_2O_{13+\delta}$ compound*

Rietveld refinement using collected data confirms that the compound crystallizes in the tetragonal *P*4/*m* space group with cell parameters values of *a*=*b*=~8.6 Å and *c*=~3.89 Å [3] at all temperatures, in contrast with $La_4BaCu_{5-x}Co_xO_{13+\delta}$ cuprates with x>3 which exhibit a vacancy disordered orthorhombic *Pnma* or rhombohedral *R*3*C* structure. This contradicts previous reports that suggest the highest Co content that allows for an oxygen-vacancy-ordered phase is x=1.1 [4], probably due to the Pechini-type gel combustion method employed in our study. This compound shows no phase transition or structural variations over the temperature range used in the thermodiffraction experiments. However, as observed in Fig. 2, as temperature increases, the occur-

rence of a secondary phase is detected which corresponds to a high temperature crystal structure of $BaCO_3$ with space group *R*-3*m*. This indicates a probable tendency of this Cu/Co-perovskite to decompose due to the thermally induced reduction of the Co ion, considering that the cuprate $La_4BaCu_5O_{13+\delta}$ does not exhibit such a tendency.

The evolution of cell parameters with temperature (Fig. 2) shows an isotropic behavior with an apparent thermal expansion coefficient (TEC) of 16.7 $x10^{-6}$ K^{-1} which is similar to the value of 17.3 $x10^{-6}$ K^{-1} calculated for $La_4BaCu_5O_{13+\delta}$ but not as high as those observed for other Co-based perovskites which are often about 20 $x10^{-6}$ K^{-1} [5] or even higher such as for $La_{0.4}Ba_{0.6}CoO_{3-\delta}$ (LBCo) with TEC=26.0 $x10^{-6}$ K^{-1} (30-900 °C) [6].

Through Rietveld refinements, the oxygen content was calculated from the occupancy factors, giving a δ value of 0.472 for the room temperature structure which is in agreement with the values calculated for $La_4BaCu_4CoO_{13.35}$ [7]. As temperature increases, the oxygen content decreases until a δ value of 0.389 for the structure at 850°C. Current efforts are being conducted in order to understand the oxygen mobility dynamics in the structure and its possible diffusion process at high temperatures, as ionic conductivity is particularly important for the application. For this purpose, future refinements using anharmonic treatments will be of great importance in order to determine the paths of oxygen diffusion and even estimate activation energies for ionic diffusion.

References

1. *Macias, M.A., Sandoval, M.V., Martinez, N.G., Vázquez-Cuadriello, S., Suescun, L., Roussel, P., Świerczek, K., Gauthier, G.H., Solid State Ionics 2016, 288, 68–75*
2. *Petricek, V., Dusek, M., Palatinus, L., The Crystallographic Computing System, Jana 2006, Institute of Physics, Praha, Czech Republic, 2006 (http://jana.fzu.cz/).*
3. *Michel, C., Er-Rakho, L., Hervieu, M., Pannetier, J., Raveau, B., J. Solid State Chem. 1987, 68, 143–152.*
4. *Anderson, P.S., Kirk, C.A., Skakle, J.M.S., West, A.R., J. Solid State Chem. 2003, 170, 1–8.*
5. *Uhlenbruck, S., Tietz, F., Mater. Sci. Eng. B 2004, 107, 277–282.*
6. *Setevich, C.F., Mogni, L.V., Caneiro, A., Prado, F.D., Int. J. Hydrog. Energy 2012, 37, 14895–14901.*
7. *Shivakumara, C., Hegde, M.S., Rajagopal, H., Sequiera, A., Materials Research Bulletin 2000, 35, 2063–2068 .*

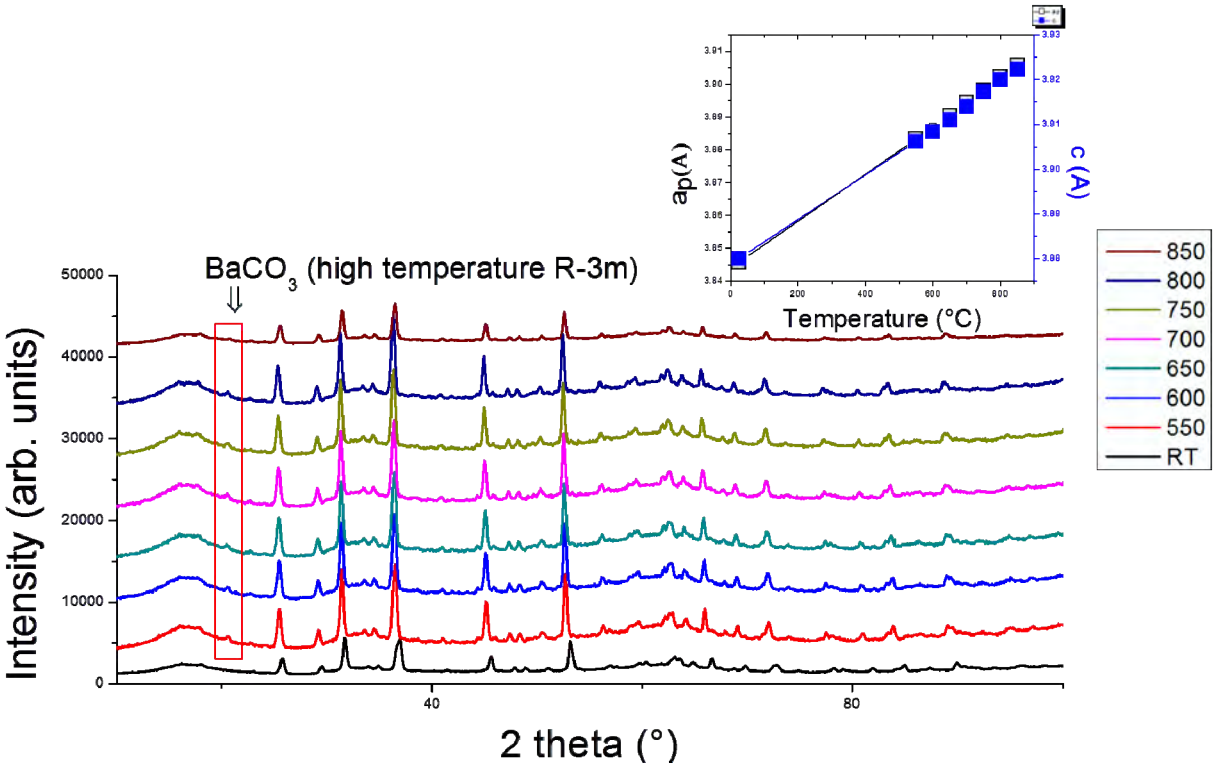

***Figure 2**: In situ high-temperature ND patterns in air and evolution in air as a function of temperature of refined cell parameters for $La_4BaCu_5O_{13+\delta}$*

Characterization of water management in a micro fuel cell using in plane neutron radiography

Planar breathing Proton exchange membrane fuel cells are promising systems for nomad applications. They however differ strongly from the classical stack structure. These cells are in particular subject to "flooding" that is the formation of liquid water which leads to a drop of performances. Neutron imaging has been used to follow the formation of liquid water in a planar fuel cell. We have observed that temperature gradients are one of the key parameter to optimize the water management.

E. Coz[a,b], J.Théry[b,*], P.Boillat[b,c], V.Faucheux[b], D. Alincant[b], P. Capron[b], G. Gébel[b]
a Université Grenoble Alpes, 621 avenue Centrale, 38400 Saint Martin d'Hères
b CEA Liten/DTNM/SENCI/LMSE, 17 rue des Martyrs, 38054 Grenoble Cedex 9 (France)
c Paul Scherrer Institut -CH-5232 Villigen PSI (Switzerland)

jessica.thery@cea.fr

Planar breathing Proton exchange membrane fuel cells are promising systems for nomad applications. Indeed, part of the management devices such as valves, pumps and humidifiers can be withdrawn leading to lightened systems. To reach current/voltage levels compatible with electronic devices, various interconnection strategies can be used, all implying design modifications. The planar breathing array involved in this study strongly differs from the classical stack structure. The interconnection to have several connected fuel-cells is made in – plane using a printed circuit board technology, leading to differences that can notably affect the behavior with respect to water nucleation.

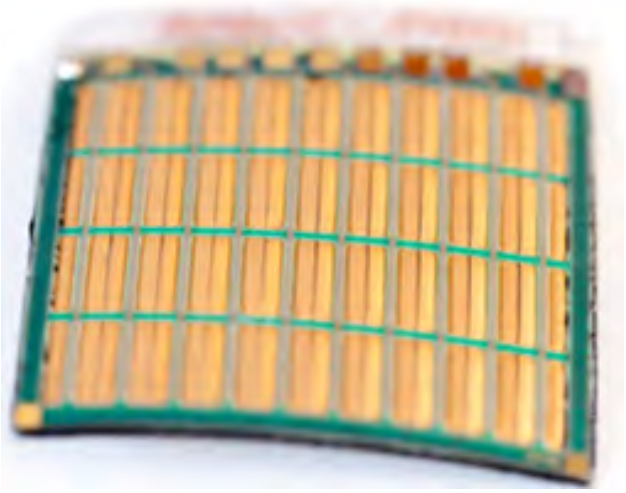

***Figure 1**: Planar micro fuel cell (size 50x50mm²)*

To develop water management solutions, it is of particular interest to be able to understand accurately the mechanisms that are driving the nucleation of liquid water domains. The presence of these domains limits the access of the reactants to the electrode, thus leading to performance decrease, known as flooding. Several studies have proven the efficiency of neutron radiography to visualize and quantify water in an operating PEMFC [1, 2]. Materials without hydrogen atoms are almost transparent to neutrons, on the contrary of water, which is responsible of a heavy attenuation. The neutron radiography is based on this principle, cold neutrons providing the contrast necessary to image the hydrogen (and water) in a PEMFC, as well as a broad field of view to visualize the entire active surface.

Neutron imaging was performed on the IMAGINE beamline of the Leon Brillouin Laboratory (LLB Saclay, France) [3]. In-plane water distribution was correlated with the design of the fuel cell and the thermic gradients. Through-plane repartition has been estimated from the shape of the water domains and fuel cell design considerations.

For proper hydrogen utilization, it is interesting for a fuel cell to work at high yield, and the operating point was chosen at 0.7V/cell. Figure 1 shows the water patterns during a step at <0.7V/cell>.

At the beginning, a grid pattern appears (A), indicating the condensation of water on the closed surface of the metal grid (which is a packaging element). Then liquid water domains nucleate along the current collectors (B): two shapes of water domains are seen, a stretch of water superimposed on the current collector and small droplets of water along the same current collectors. Water droplets correspond to the condensation on the hydrophobic wall of the anodic chamber. Finally the formation of larger liquid water do-

mains appears first from the border of the fuel cell, then grows to mask active zones (C). The nucleation of liquid domains along current collectors is probably driven by the temperature gradient, the collecting element being 4-5°C colder than the active surface. The performance decrease appears after 10 minutes, leading to a power drop of 50% after 10 h.

In order to evaluate the amount of water present respectively at the cathode and at the anode side, the fuel cell has been weighted before and after flooding. Then the cathode was dried with compressed air, in order to measure the water mass remaining in the anode chamber. These results indicate that 25% of the liquid water mass was found on the breathing cathode side and 75% in the anodic chamber.

Water domains with a thickness up to 1.5 mm are measured between ribs. These thick domains of liquid water result mainly from the condensation of water in the anodic chamber. The thickness of the chamber between the MEA and the anodic chamber being far below 1.5 mm, the observation of these water zones reveals a huge swelling of the membrane, caused by the pressure gradient (0.4 bar) between the anode and cathode sides.

The water being produced at the cathode side, this study pointed out the importance of water back-diffusion to the anode and the possibility to use in-plane neutron radiography to validate design evolutions (water management layers, fuel cell materials). For planar breathing fuel cells, water back-diffusion was not expected [4], but we observed that the presence of interconnection elements, acting as cold elements, favors the back diffusion.

Complementary SANS experiments will provide pieces of information on the correlation between liquid water on the electrodes and local membrane hydration.

References

1. *D. Kramer, J. Zhang, R. Shimoi, E. Lehmann, A. Wokaun, K. Shinohara, G. G. Scherer, Electrochimica Acta* ***50*** *(2005) 2603–2614*
2. *M. A. Hickner, N. P. Siegel, K. S. Chen, D. N. McBrayer, D. S. Hussey, D. L. Jacobson, M. Arif, Journal of The Electrochemical Society,* ***153*** *(2006) 902-A908*
3. *F. Ott, C. Loupiac, S. Désert, A. Hélary, P. Lavie, Physics Procedia* **69** (2015) 67-70
4. *S. Hamel, L. G. Fréchette, Journal of Power Sources* ***196*** *(2011) 6242–6248*

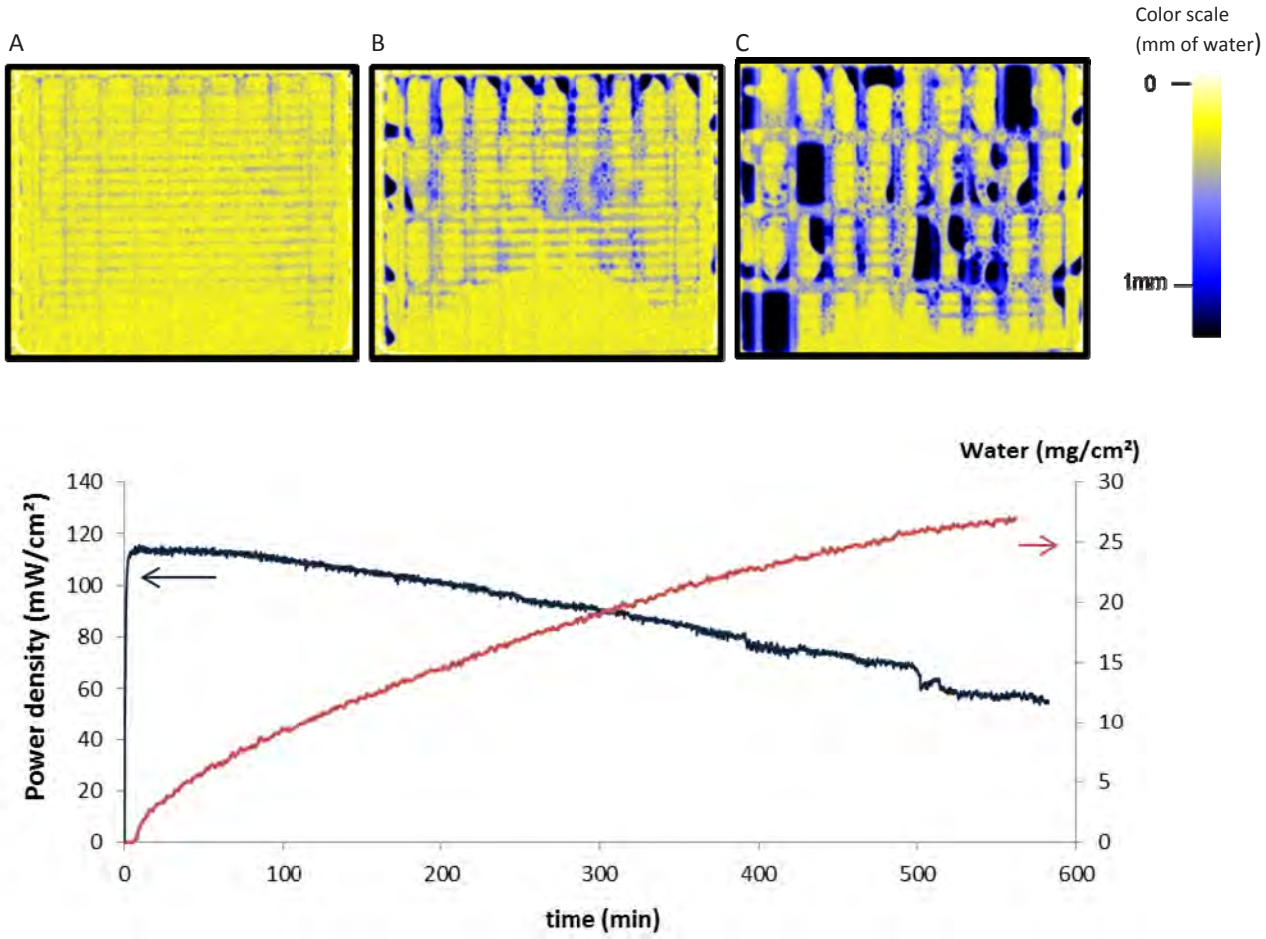

Figure 2*: Water accumulation (red) and power density evolution (blue) during a flooding step, and the corresponding neutron images*

Atomic structure and formation of CuZrAl bulk metallic glasses and composites

$Cu_{47.5}Zr_{47.5}Al_5$ metallic glass is studied experimentally by high-energy X-ray diffraction, neutron diffraction with isotopic substitution, electron diffraction and X-ray absorption spectroscopy. The atomic structure of the glass is modeled by reverse Monte-Carlo and molecular dynamics simulations. RMC modeling of seven experimental datasets enabled reliable separation of all partial pair distribution functions for $Cu_{47.5}Zr_{47.5}Al_5$ metallic glass. A peculiar structural feature of the ternary alloy is the formation of the strong Al–Zr bonds, which are supposed to determine its high viscosity and enhance bulk glass formation. Analysis of the local atomic order in $Cu_{47.5}Zr_{47.5}Al_5$ glass and $Cu_{10}Zr_7$, $CuZr_2$ and CuZr B2 crystalline structures elucidates their similarities and differences explaining the phase formation sequence by devitrification of the glass.

I. Kaban[a,b], P. Jóvári[c], B. Escher[a,b], D.T. Tran[d], G. Svensson[d], M.A. Webb[e], T.Z. Regier[e], V. Kokotin[f], B. Beuneu[g], T. Gemming[b], J. Eckert[a,b]

a TU Dresden, Institut für Werkstoffwissenschaft, 01062 Dresden, Germany
b IFW Dresden, Institute for Complex Materials, Helmholtzstr. 20, 01069 Dresden, Germany
c Institute of Solid State Physics, Wigner Research Centre for Physics, Budapest H-1525, Hungary
d Stockholm University, Department of Materials & Environmental Chemistry, 10691 Stockholm, Sweden
e Canadian Light Source, 44 Innovation Blvd, Saskatoon, SK, Canada
f ThyssenKrupp Steel Europe AG, Duisburg, Germany
g Laboratoire Léon Brillouin CEA/CNRS UMR 12, Gif sur Yvette, France
i.kaban@ifw-dresden.de

Bulk metallic glasses (BMG) and bulk metallic glass matrix composites (BMGMC) have received high attention due to their potential use as advanced structural materials. In particular, the idea of combining the large elastic strain and high yield strength characteristic of metallic glasses with the plasticity of crystalline alloys has induced extensive research in this field. It is expected that metallic glass matrix composites can be fabricated either directly by casting from liquid state (in-situ) or through special treatment of metallic glass (ex-situ). In this view, the glass forming ability (GFA) and stability of the glassy matrix and the formation of desired crystalline phase(s) are the main issues to be understood in order to control the microstructure and tailor the functional properties of BMGMC. CuZrAl bulk metallic glass matrix composites with CuZr B2 phase show plasticity in compression and tension. By casting at an appropriate cooling rate, it is possible to obtain CuZr B2 phase in a glassy matrix, but with an undesirable heterogeneous spatial and size distribution. Recently, $Cu_{47.5}Zr_{47.5}Al_5$ glassy ribbons were rapidly annealed by Joule-heating. This enabled designing metallic glass matrix composites with uniformly dispersed CuZr B2 microcrystals, which exhibited a high fracture strength and remarkable tensile ductility. Knowledge

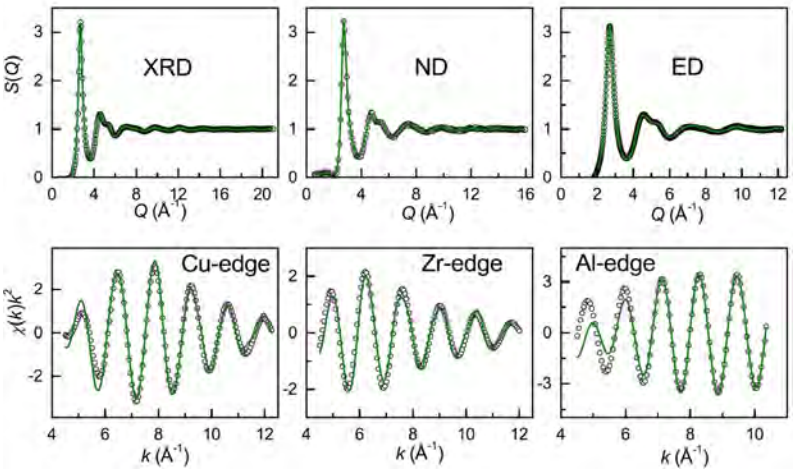

***Figure 1**: RMC fits to the experimental datasets measured on $Cu_{47.5}Zr_{47.5}Al_5$ metallic glasses (neutron diffraction data for the sample prepared with ^{63}Cu isotope is not shown).*

of the structure of $Cu_{47.5}Zr_{47.5}Al_5$ metallic glass and its relationship with the structure of precipitating crystalline phases can help in understanding the crystallization sequences and controlling phase formation by fabrication of bulk metallic glass matrix composites. One of the main problems of structural studies of multicomponent non-crystalline alloys is that the number of available diffraction datasets is usually less than the number of partial pair distribution functions (PDF). Indeed, in order to determine all partial PDF's characterizing an alloy, the same number of independent diffraction measurements is

required. Extended X-ray absorption fine structure spectroscopy (EXAFS) is a powerful source of structural information. It has been shown in studies of different glasses that combination of X-ray diffraction, neutron diffraction and EXAFS data in the frame of the reverse Monte Carlo (RMC) simulation technique enables determination of the partial pair distribution functions. To gain detailed information about the atomic arrangement in $Cu_{47.5}Zr_{47.5}Al_5$ metallic glass we performed X-ray diffraction, electron diffraction (ED), neutron diffraction with Cu-isotopic substitution and EXAFS measurements at the K-absorption edges of all components, and modelled them simultaneously using RMC.

Figure 1 shows a very good agreement of the experimental diffraction and EXAFS data for $Cu_{47.5}Zr_{47.5}Al_5$ metallic glass with the corresponding Reverse Monte Carlo (RMC) curves. The partial pair correlation functions $g_{ij}(r)$ extracted from the RMC configuration box are plotted in Figure 2. The mean interatomic distances (bond lengths) r_{ij} were determined by a Gaussian fit of the first peak on $g_{ij}(r)$ curves.

The partial pair distribution functions and structural parameters of $Cu_{47.5}Zr_{47.5}Al_5$ metallic glass obtained by Molecular Dynamics simulation are compared with the RMC results (Fig. 2). It is noteworthy that there is a very good agreement for the Cu–Cu, Cu–Zr and Zr–Zr functions, but remarkable differences are observed for the pair correlation functions involving Al atoms. The situation is clear for the $g_{AlAl}(r)$ distribution function, where the main difference is appearance of the first peak at r_{AlAl} = 2.84 Å in the MD model, whereas this bond was forbidden by RMC simulation as discussed above. However, there is also notable discrepancy on Al–Cu and Al–Zr $g_{ij}(r)$ functions, indicating significant difference of these distributions in the RMC and MD models. To check this, we performed a RMC simulation trying to fit the experimental data for $Cu_{47.5}Zr_{47.5}Al_5$ metallic glass using Al–Cu and Al–Zr partial pair distribution functions from the MD model as the constraints. The quality of the fits of the diffraction data (ND, XRD, ED) remained almost unchanged and they are therefore not shown here. However, the fits of the EXAFS data in the constrained RMC simulation become worse, especially the Al-edge fit (Fig. 4 in [1]), showing inconsistency of the MD simulated Al–Cu and Al–Zr partial pair distribution functions with experiment. This also emphasizes the high importance of the Al-edge EXAFS data for the determination of these distributions.

The following can be concluded after analysis of the structural models obtained by reverse Monte-Carlo and Molecular Dynamics simulations:

(i) RMC and MD models of the $Cu_{47.5}Zr_{47.5}Al_5$ metallic glass show a very good agreement for the Cu–Cu, Cu–Zr and Zr–Zr partial pair distribution functions, but there are notable discrepancies for the atomic pairs involving Al atoms;

(ii) Al–Al bonds are not needed for a good fit of the experimental data for $Cu_{47.5}Zr_{47.5}Al_5$ glass;

(iii) Al shows preference for formation of Al–Zr bonds over Al–Cu bonds;

(iv) formation of the Al–Cu and particularly strong Al–Zr bonds is supposed to determine high viscosity and enhanced bulk glass forming ability of CuZrAl alloys;

(v) structural constraints of $Cu_{47.5}Zr_{47.5}Al_5$ metallic glass favor the following crystallization sequence by devitrification: $Cu_{10}Zr_7$, $CuZr_2$, CuZr B2.

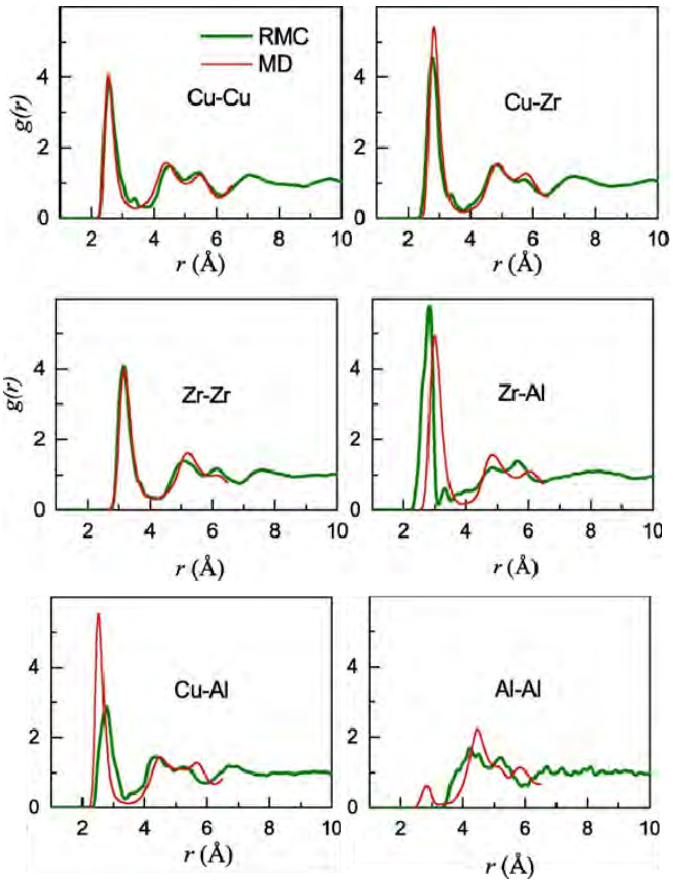

***Figure 2**: Partial radial distribution functions for $Cu_{47.5}Zr_{47.5}Al_5$ metallic glass compared to $Cu_{10}Zr_7$, CuZr B2 and $CuZr_2$ crystal structures.*

References

1. *I. Kaban, P. Jovari, B. Escher et al, Acta Materialia **100** (2015) 369-376.*
2. *I. Kaban, P. Jóvári, V. Kokotin et al, Acta Materialia **61** (2013) 2509–2520.*
3. *I.V. Okulov, I.V. Soldatov, M.F. Sarmanova et al, Nature Communications **6** (2015) 7932 (6 pages).*
4. *O. Gereben, P. Jóvári, L. Temleitner, L. Pusztai, Journal of Optoelectronics and Advanced Materials **9** (2007) 3021–3027.*

From nanopores to macropores: Fractal morphology of graphite

A comprehensive structural characterization of two different highly pure nuclear graphites that compasses all relevant length scales from nanometers to sub-mm was performed. This has been achieved by combining several experiments and neutron techniques: Small Angle Neutron Scattering (SANS), high resolution Spin Echo SANS (SESANS) and neutron imaging. In this way it was possible to probe an extraordinary broad range of six orders of magnitude in length from microscopic to macroscopic length scales. The results reveal a fractal structure that extends from ~0.6 nm to 0.6 mm and has surface and mass fractal dimensions both very close to 2.5, a value found for percolating clusters and fractured ranked surfaces in 3D.

Zhou Zhou[a], Wim G. Bouwman[a], Henk Schut[a], Sylvain Desert[b], Jacques Jestin[b], Stefan Hartmann[c], Catherine Pappas[a]

a Delft University of Technology, Faculty of Applied Sciences, Mekelweg 15, 2629JB, Delft, The Netherlands
b Laboratoire Léon Brillouin CEA/CNRS UMR 12, Gif sur Yvette, France
c Laboratory for Neutron Scattering and Imaging, Paul Scherrer Institute, CH-5232 Villigen PSI, Switzerland

Z.Zhou-1@tudelft.nl

Graphite has been used as a neutron moderator in several types of nuclear reactors from the Chicago Pile 1 in 1942 to the more recent Very High Temperature Reactor (VHTR) and High Temperature Gas-cooled Reactors (HTGR). This synthetic polygranular material has a very high chemical purity and a complex microstructure, which affects the mechanical properties under extreme conditions and irradiation damage. The crystallite structure and disorder of graphite at the atomic level can be investigated by neutron or X-ray diffraction [1], and the microstructure by TEM, SEM or optical microscopy. On the other hand, the bulk mesoscopic structure of the pores can be explored by small angle scattering of X-rays (SAXS) or neutrons (SANS). Very first SANS measurements on non-irradiated and irradiated nuclear graphites were performed in the 1960s [2] and 1970s [3-5]. These results have been reinterpreted recently [6] to disclose a surface fractal structure from ~0.2 to 300 nm, i.e. over three orders of magnitude in length. However, the graphite inhomogeneities can be seen with an optical microscope or even with naked eye. Therefore an exploration over a larger range of length scales is necessary and for this purpose we have combined three neutron-based techniques: SANS, Spin Echo SANS (SESANS) and imaging to cover lengths from nm to mm. We investigated two different highly pure nuclear graphites, and the results show a fractal structure over an extraordinary large scale of lengths that spans 6 orders of magnitude and has fractal dimensions close to 2.5. This value is expected for several cases of percolating clusters and in the most general case of fractured ranked surfaces.

The samples were disk-shape specimens with a thickness of 0.5 mm and a diameter of 16 mm cut from two types of nuclear graphite, designated as RID and PGA. The RID

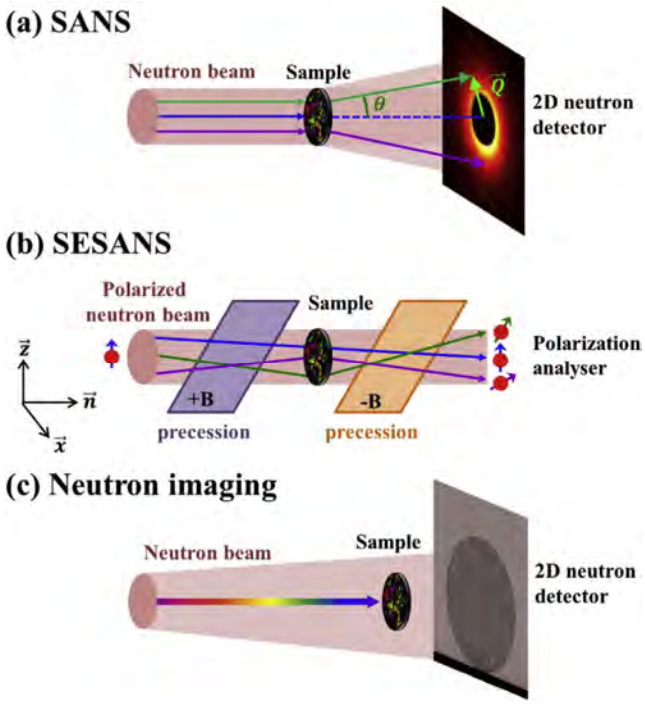

***Figure 1**: The 3 neutron scattering/transmission techniques used to probe length-scale over an ultra-wide range.*

graphite was manufactured by Pechiney SA in the 1960's by baking a paste made of oil coke and pitch, graphitized by electrical heating. The PGA (Pile Grade A) graphite was manufactured by British Acheson Electrodes, Ltd. and Anglo Great Lakes, from needle shaped coke particles derived from the petroleum industry. It was used in the early gas cooled reactors in UK. PGA was manufactured by extrusion, which leads to aligned coke particles and thus to the anisotropic properties.

In this work SANS measurements were performed at two instruments, the medium resolution PAXE and the high resolution TPA of the Laboratoire Léon Brillouin (LLB), CEA Sac-

lay, France. The experiments on TPA were done at λ = 0.6 nm, covering the Q range 6 x 10^{-3} < Q < 1 x 10^{-1} nm^{-1}, and on PAXE at λ = 0.37, 0.6 and 1.7 nm, respectively, covering the Q range 3 x 10^{-2} < Q < 5 nm^{-1}. The PAXE data for λ = 0.6 nm were brought to absolute units by normalization to the incident beam and were then used to normalise all other data using the large overlap in the Q-ranges illustrated by Fig. 2a for the case of PGA1. The measured absolute scattering cross section follows a power law with exponent 3 < β < 4, revealing a surface fractal structure. Multiple scattering in this study does not affect the power law as demonstrated in Fig. 2(b-d).

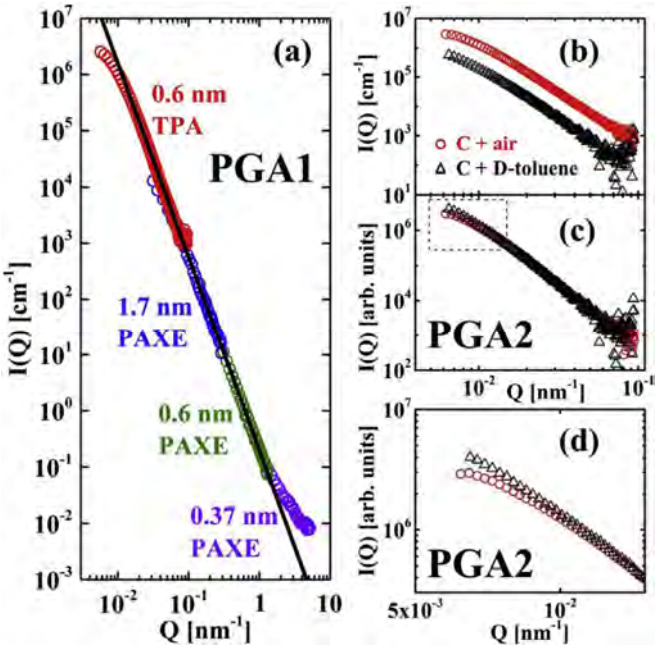

Figure 2: *(a) Absolute scattering cross section I(Q) of PGA1 The power law $I(Q) \propto Q^{-\beta}$ with β=3.45 is the black line. (b)-(d) Contrast variation experiments to investigate the effect of multiple scattering: (b) I(Q) of PGA2 in air (red circles) and of the same sample embedded in deuterated toluene (black triangles). The data are vertically shifted to overlap in (c). A slight difference is found at the very low-Q range, which is enlarged in (d).*

The characterization at longer lengthscales was performed using SESANS which gives access to micrometer lengthscales. The SESANS experiments were performed at the dedicated instrument of the Reactor Institute Delft [7] at λ = 0.2nm and covered length scales from 30 nm to 20 µm. Longer lengthscales were probed by neutron imaging at the cold neutron facility, ICON, of the Paul Scherrer Institute, Switzerland [8]. The samples were placed as close as possible to the detector and a resolution of ~30 µm was obtained. Figure 3 summarizes the aggregated results. that are interpreted using a fractal model. The fractal dimensions found in this work are comparable to those expected for percolating clusters. The porosity values indicate a topology close to that of a percolating cluster. The identity $D_m = D_s \sim 2.5$ is not a coincidence but the consequence of the high degree of disorder, ramification and connectivity of the pore structure. Under neutron irradiation surface fractality disappears [6], and similar behaviour may be expected for the oxidised samples.

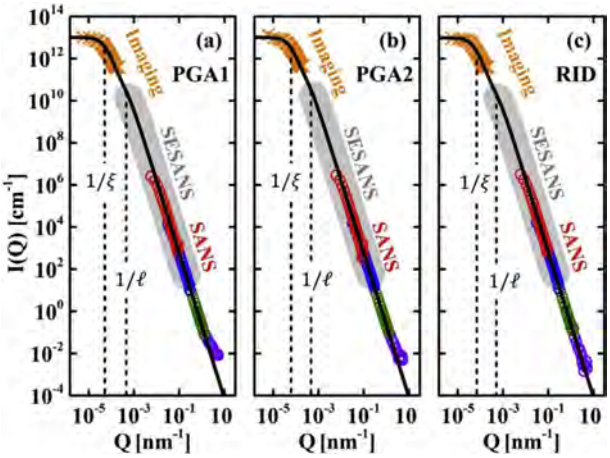

Figure 3*: Scattering curves for (a) PGA1 (b) PGA2 and (c) RID over for the whole Q range investigated.*

The methodology developed in this work thus can be applied to further investigate the effect of irradiation damage and/or oxidation on the structural properties of graphite. Fractal scattering has also been reported for carbon nanopores, rocks or cement. The particularity of this work is in the extraordinarily broad length scale of six orders of magnitude over which fractal scaling is quantitatively valid. The combination of several techniques, from imaging to scattering and the methods can be applied to the investigation of other complex systems with a hierarchy of length scales such as biological materials, concrete and rocks, materials for CO_2 sequestration, Li batteries, fuel cells or solar cells.

References

1. *Z. Zhou, W.G. Bouwman, H. Schut, C. Pappas, Carbon 69 (2014) 17-24*
2. *D.G. Martin, R.W. Henson, Phil. Mag. 9 (100) (1964) 659-672*
3. *D.G. Martin, J. Caisley, Carbon 15 (4) (1977a) 251-255*
4. *D.G. Martin, J. Caisley, J. Nucl. Mater. 67 (3) (1977b) 318-319*
5. *D.G. Martin, J. Caisley, Carbon 16 (3) (1978) 199-203*
6. *Z. Mileeva, D.K. Ross, S.M. King, Carbon 64 (2013) 20-26*
7. *M.T. Rekveldt, J. Plomp, W.G. Bouwman, et al, Rev. Sci. Instrum. 76 (3) (2005)*
8. *A.P. Kaestner, S. Hartmann, G. Kuhne, G. Frei, C. Grunzweig, L. Josic, et al., NIMA 659 (1) (2011) 387-393.*

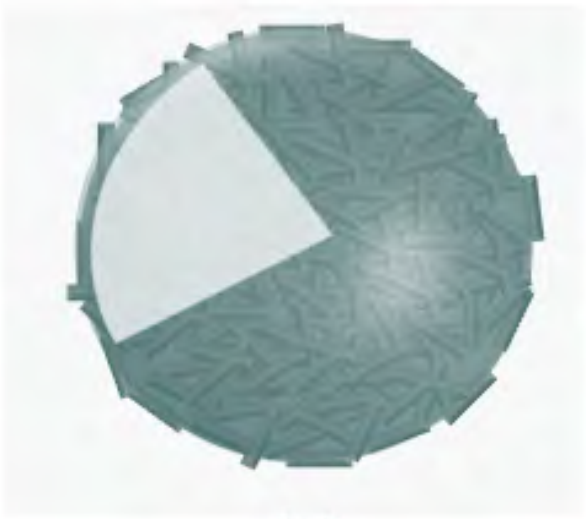

(a)

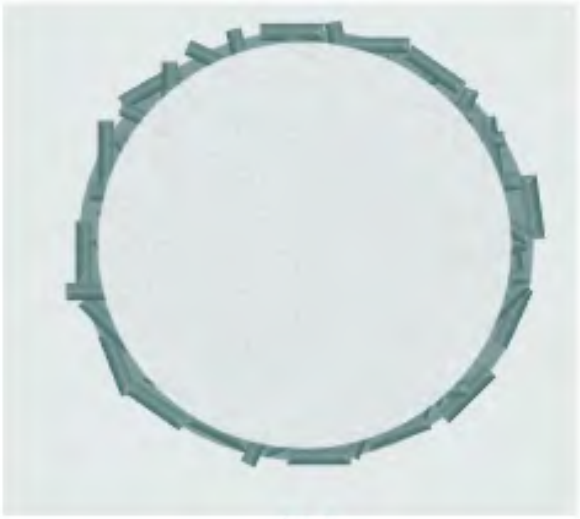

(b)

(c)

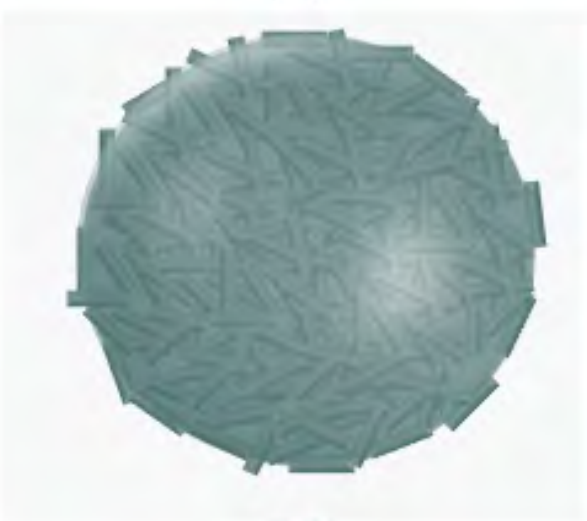

(d)

Soft Complex Matter and Biophysics

"Soft Complex Matter and Biophysics" deals with systems made of individual building blocks (colloidal nanoparticles, polymers, surfactants, proteins and phospholipids) whose characteristic sizes lay in the 0.1–10 nm range. In such systems, the delicate balance of interactions (of the order of kBT) can lead to the formation of large self-assembled complex architectures showing specific dynamics, kinetics or lifetime. Understanding the underlying mechanisms of their self-assembly and dynamics is then the key to control and tune the very specific properties of inert, functional or biological matter at the nanometer scale (1-100 nm). In this framework, the neutron scattering techniques combined with H/D isotopic labeling are a unique tool to characterize the systems at the relevant spatial and temporal scales of the systems. In particular, they make it possible to get a refined picture of the behavior of the building blocks in specific physicochemical conditions such as self-assembled surfactants in ionic liquids (Dourdain et al), polymer brushes under stretching (Chennevière et al) or within complex architectures such as ultrastable foams (Salonen et al) or cellulose-based Pickering emulsions (Capron et al). Finally, the recent development of neutron imaging techniques enables to solve the structure of systems up to the macroscopic scale, as illustrated by the description of the meat under cooking (Scussat et al).

- **Aggregation in synergistic solvent extraction: Solvent effect from alkanes to ionic liquids**
  S. Dourdain, J. Rey, T. Sukhbaatar, J. Jestin, R. Turgis, G. Arrachart, S. Pellet-Rostaing, T. Zemb
- **Direct molecular evidence of the origin of slip of polymer melts on grafted brushes**
  A. Chennevière, F. Cousin, F. Boué, E. Drockenmuller, K. R. Shull, L. Léger, F. Restagno
- **Ultrastable and thermostimulable foams made from simple soaps and salts**
  L. Zhang, A. Mikhailovskaya, P. Yazhgur, F. Muller, F. Cousin, D. Langevin, N. Wang, A.Salonen.
- **Unraveling the mechanisms of stabilization of Pickering emulsions by cellulose nanocrystals by SANS**
  F. Cherhal, F. Cousin, I. Capron
- **Neutron imaging of meat during cooking**
  S. Scussat, F. Ott, A. Helary, S. Desert, Olivier Gaiffe, Christian Pierralli, Bruno Wacogne, P. Cayot C. Loupiac

Aggregation in synergistic solvent extraction: Solvent effect from alkanes to ionic liquids

Looking at aggregation effects on solvent extraction, we showed that the intensity of the unexplained synergy peak is strongly dependent on the "penetrating" or "non penetrating" nature of the alkanes used as diluent. This experimental determination allowed us to attribute the synergy to a combination of entropic effects favoring extraction and extractant film bending energy, opposed to perturbation of the first coordination sphere by penetration.

Having many favorable properties over conventional diluents, ionic liquids are more and more considered in solvent extraction. They provide environmentally benign feature, adjustable polarity and in some cases higher extraction performances, that remain however not predictable. With the same approach as with alkanes, we evidenced the supramolecular aggregation of extractant molecules in ionic liquid, expected to bring new insights on the different solvent extraction mechanisms observed in ionic liquids.

S. Dourdain,[a] J. Rey,[a] T. Sukhbaatar,[a] J. Jestin,[b] R. Turgis,[a] G. Arrachart,[a] S. Pellet-Rostaing,[a] T. Zemb[a]
a ICSM, CEA/CNRS/UM2/ENSCM UMR5257, Site de Marcoule, Bagnols sur Cèze, France
b Laboratoire Léon Brillouin CEA/CNRS UMR 12, Gif sur Yvette, France

sandrine.dourdain@cea.fr

Solvent extraction is a hydrometallurgical process, commonly used for ores exploitation, wastes separation or for decontamination of polluted phases. By contacting the aqueous phase that needs to be treated, to an organic phase containing some "extractant" molecules, the elements of interest can be selectively transferred to the organic phase.

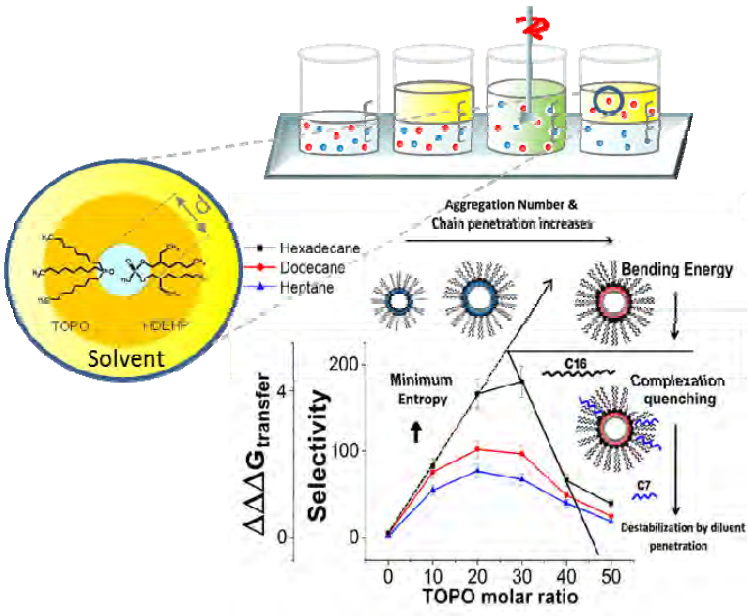

Figure 1*. Effect of alkanes chain length on Ion transfer on the synergistic system HDEHP/TOPO.*

It is now established that the mechanisms underlying these processes are based not only on the molecular chelation properties of the extractant molecules, but also on their ability to form supra-molecular aggregates due to their amphiphilic nature [1,2].

Playing first with conventional alkanes we investigated the physical origin of the "diluent effect" on synergistic extraction. As diluents are traditionally expected to modify aggregation without perturbing chelation mechanisms, this study aimed at evaluating the importance of aggregation in the synergistic extraction mechanisms, our driving question being:" How do diluents affect the relative values of extraction free energy and aggregate formation free energy?". This question remains marginal: in the historical approach used since the seventies, one considers the extractions as the result of well-defined competing complexes, where the balance reactions used do consider ligand activity in the diluent, but one does not consider the activities of diluent. Different diluent with different chain lengths, from heptane to hexadecane, were tested on the solvent extraction system containing extractants, Di-(2-ethylhexyl)phosphoric acid (HDEHP) and tri-octyl phosphine oxide (TOPO) in various ratios. The combination of these two molecules is known to allow a synergistic extraction of uranium in a ratio 4:1 [3]. The results obtained for 3 diluents are sketched in Figure 1. We showed that these synergistic properties are related to a favored aggregation,[2] and combined SAXS and SANS measurements pointed out the solvent polarity influence on this system: complete fit of the data evidenced the presence of core shell reverse-micelle like aggregates, into which the penetration of diluent having shorter chain length was found to induce lower extraction efficiency. In presence of conventional alkanes, configurational entropy and curvature free energy of the aggregates were therefore shown to monitor the synergy as well as the diluent effect on extraction [4].

A recent challenge in solvent extraction is today to replace conventional organic solvents (often toxic and volatile), with ionic liquids (IL).[5] Depending on the extraction systems tested, these new solvents show better efficiency than the conventional ones.[6] Although some assumptions based on ions exchanges have been proposed in the literature,[5,6] the involved mechanisms are still poorly understood. So far, no study was conducted to evaluate the IL effect on the aggregation properties of the extractant molecules, even though ILs are known to modify the curvature radii of surfactant microemulsions.[7]

Investigating the HDEHP/TOPO system described previously, in Omim[Ntf2] ionic liquid as diluent, very different extraction properties were observed as a synergistic peak shifted to 50% of TOPO ratio. Aggregates signals similar to the ones observed in conventional diluents were evidenced from SAXS measurements (Figure2). However the strong structural peaks of the IL prevent a proper fit analysis. Therefore the synthesis of fully deuterated IL was proposed, allowing the measurement of SANS spectra with no structural peak [8].The IL's deuteration enables full characterization of the aggregates (Table 1).

The trend observed with increasing TOPO percentages is similar to the one obtained in deuterated dodecane. Considering a core-shell model as in the common organic diluents, the increase of scattered intensity observed in IL could be interpreted in terms of aggregation number (Nag) and of penetration of the diluent in the apolar shell. This behavior will be fully quantified in a further study thanks to a complete fit of the data, and related to an estimation of the important thermodynamic driving force of extraction, such as configurational entropy and binding energy of aggregates [4].

	in [OMim][NTf_2]			in dodecane		
TOPO (%)	0	50	100	0	20	50
R_{SAXS} (nm)	1.1	1.0	0.9	0.2	0.3	0.4
R_{SANS} (nm)	1.4	1.5	1.5	0.6	0.7	0.9

***Table 1** : Estimations of the aggregates radii derived from a guinier analysis (average uncertainty: ± 0.2nm)*

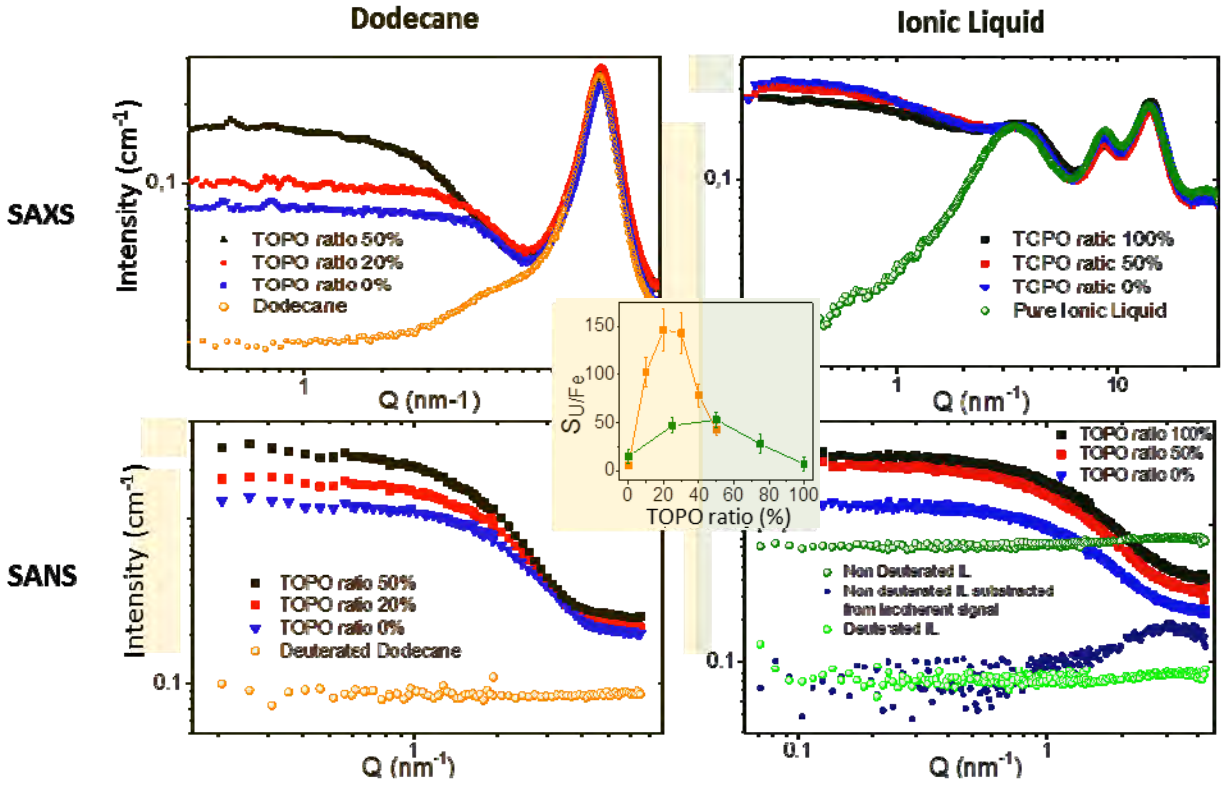

***Figure 2** : X ray and neutron scattering curves at different TOPO ratios in [OMim][NTf_2] Ionic Liquid and Dodecane*

References

1. K. Osseo-Asare, Adv. Colloid Interface Sci. 1991, 37, 123-173.

2. S. Dourdain, I. Hofmeister, O. Pecheur, J-F. Dufrêche, R. Turgis, A. Leydier, J. Jestin, F. Testard, S. Pellet-Rostaing, T. Zemb, Langmuir 2012, 28, 11319.

3. F.J. Hurst, D.J. Crouse, K. B. Brown, Ind. Eng. Chem. Process Des. Develop, 1972, 11, 12.

4. Rey, J.; Dourdain, S.; Berthon, L.; Jestin, J.; Pellet-Rostaing, S.; Zemb, T., Langmuir, 31 (2015) 7006.

5. S.J. Yoon, J.G. Lee, H. Tajima, A. Yamasaki, F. Kiyono, T. Nakazato, H. Tao, J. Ind. Eng. Chem., 16 (2010) 350.

6. M.L. Dietz, D.C. Stepinski, Talanta, 75, 2 (2008) 598.

7. 5 O. Zech. S. Thomaier, P. Bauduin, T. Rück, D.Touraud, W. Kunz, J. Phys. Chem. B, 113 (2009) 465.

8. T. Sukhbaatar, S. Dourdain, R. Turgis, J. Rey, G. Arrachart and S. Pellet-Rostaing, Chem. Commun. 51 (2015) 15960.

Direct molecular evidence of the origin of slip of polymer melts on grafted brushes

Surface anchored polymer chains were found to present many interesting physical properties that gave rise to intensive theoretical and experimental studies. For example, these "polymer brushes" can modify the mechanical properties of composite materials by tuning the adhesion and friction properties of the numerous polymer interfaces. The situation where a molten polymer in contact with a grafted surface is subjected to a steady plane shear stress is one of the model situations of stress transmission on such interfaces. In this study, we used neutron reflectivity to probe at a molecular scale the influence of a plane-Couette flow on the conformation of end-grafted polymer chains immersed in a chemically identical polymer melt.

A. Chennevière[a,b], F. Cousin[a], F. Boué[a], E. Drockenmuller[b], K. R. Shull[c], L. Léger[d], F. Restagno[d]

a Laboratoire Léon Brillouin CEA/CNRS UMR 12, Gif sur Yvette, France
b Ingénierie des Matériaux Polymères, CNRS, UMR 5223, Université Lyon 1, Villeurbanne, France
c Department of Materials Science and Engineering, Northwestern University, Evanston, USA
d Laboratoire de Physique des Solides, CNRS, UMR 8502, Université Paris-Sud, Orsay, France

alexis.chenneviere@cea.fr

Surface velocimetry measurements performed on a polymer melt flowing onto a polymer brush have shown a transition from low wall slip to high wall slip above a shear rate threshold [1]. This transition has been interpreted in terms of stretching and disentanglement of the grafted chains from the melt chains due to the shear forces [2]. However, there is up to date no direct experimental proof of the change in conformation of the grafted chains. Here we describe a series of neutron reflectivity experiments that allowed us to probe directly the influence of shear on the conformation of grafted polymer chains and test the relevance of this stretching and disentanglement mechanism.

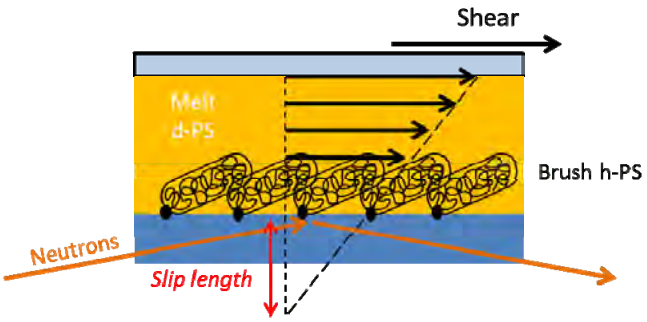

Figure 1: *Schematic representation of d-PS melt flowing onto a h-PS polymer brush.*

The experimental system is composed of hydrogenated polystyrene chains (h-PS) grafted onto a silicon wafer in contact with a thick (around 140 µm) deuterated polystyrene (d-PS) melt [3] as depicted in figure 1. In order to shear these samples in the melt state, we designed a specific experimental setup (Fig. 2).

This setup allows heating the sample above the glass transition temperature of polystyrene (T_g = 100°C) and displacing the upper plate at a constant velocity. In order to freeze the disordered conformation of the grafted chains, the sample was then rapidly quenched below T_g by a cold water jet.

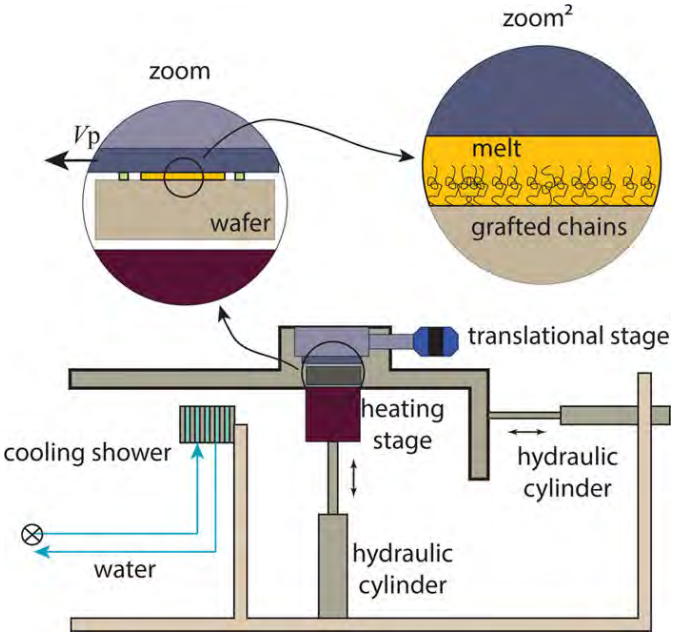

Figure 2*: Schematic representation of the shear and rapid quenching setup. It is composed of a linear translational stage, a sample holder, a heating cylinder and a cooling shower. After exerting a constant shear rate above T_g, the sample is then quenched below T_g by the cooling shower.*

Figure 3 presents the reflectivity data of one sample sheared with an upper plate velocity V_p = 7 µm/s either immediately after the shear or after annealing the sample or 7 hours at 140°C allowing the equilibration of the grafted

chains. Here, we observe a significant increase in the reflectivity for wave vectors ranging from 0.01 to 0.03 $Å^{-1}$. This is a clear a direct indication that the interface between the melt and the grafted chains is sharper for the sheared sample than for the annealed one.

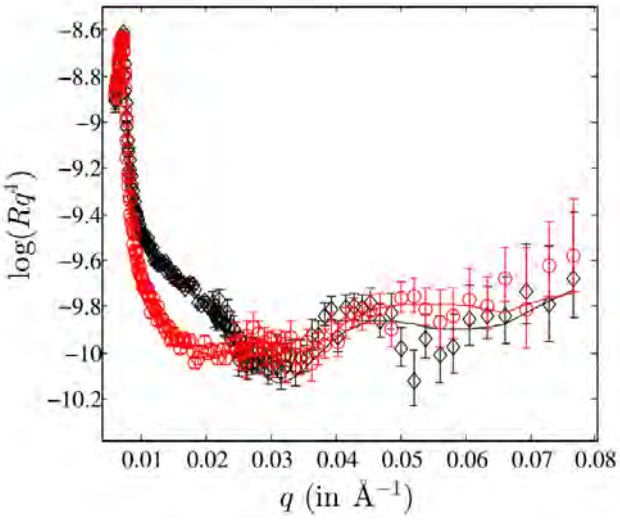

***Figure 3**: Neutron reflectivity spectra of a h-PS brush immersed in a d-PS melt (◇) immediately after the shear and after 7h of annealing at 140 °C (O) . The solid lines correspond to the best fits.*

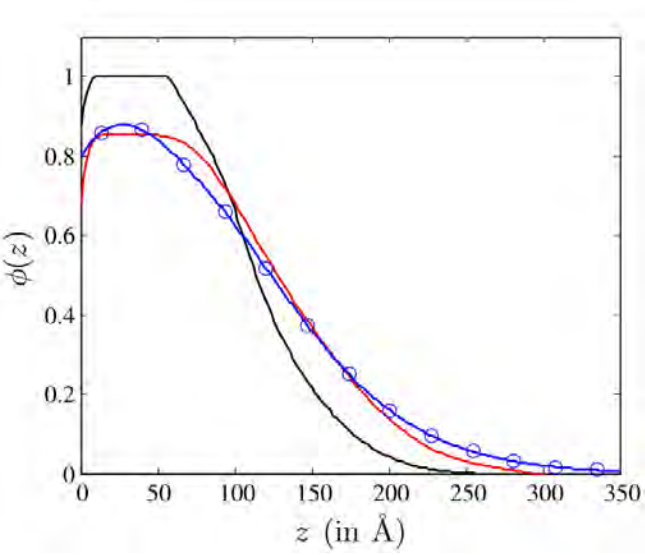

Figure 4: Monomer density profiles obtained from the fits of data presented in figure 3: (black solid line) after the shear and (red solid line) after 7h of annealing at 140°C. The blue open circle line corresponds to the equilibrium density profile computed by SCF.

To go further in the analysis, we fitted the neutron reflectivity spectra in order to obtain the concentration profile of monomers belonging to the surface-anchored chains denoted Φ(z) and compare them to the predictions of equilibrium profile obtained through self-consistent field theory [4] (SCF). The density profiles issued from the fit of the data are plotted in figure 4 where they are compared with the prediction of SCF. They show two main results. First, we observe that the density profile of the annealed sample is very close from the SCF predictions which show that a 7 hours annealing at 140°C is long enough to recover he equilibrium conformation of the grafted chains. Thus, the shear has nor cleaved, nor detached such grafted chains. Second, regarding the segmental density profile just after the shear and quenching steps, we observe that it is less extended from the solid wall and much sharper than the equilibrium profile. Moreover, the monomer volume fraction close to solid wall is significantly higher and reaches 1 over more than 6 nm from the wall. This clearly shows that the shear has expelled the free chains from the brush while collapsing the grafted chains on the solid substrate. Such decoupling between the grafted and melt chains is assumed to occur above the marginal friction regime.

According to the scaling law model of Brochard and de Gennes [1], this transition should occur above the critical shear rate $\dot{\gamma}^* = \frac{\Sigma k_B T}{\eta\sqrt{N_e}a}$ with η the bulk viscosity, Σ the dimensionless grafting density, N_e the average number of monomers between two entanglements and a the monomer size. In our experimental conditions, this threshold is estimated to be: $\dot{\gamma}^* \approx 4\ 10^{-5}\ s^{-1}$. This is three orders of magnitude below the smallest apparent shear rate used in the experiment:

$\dot{\gamma}_{app} > 1.4\ 10^{-2}\ s^{-1}$. It is then fully plausible to admit that the sample has been sheared well above the slip transition for which neutron reflectivity provided a direct proof at the molecular scale of the decoupling between the grafted chains and the melt chains.

References

1. Durliat, E., Hervet, H. & Leger, L. , Europhys. Lett. EPL 38, 383–388 (1997).

2. Brochard-Wyart, F., Gay, C. & De Gennes, P. G. , Macromolecules 29, 377–382 (1996).

3. Chennevière, A. et al., Macromolecules (2016).

4. Shull, K. R. , J. Chem. Phys. 94, 5723 (1991).

Ultrastable and thermostimulable foams made from simple soaps and salts

How to form long-lived foam from conventional and cheap materials, and whose stability can be modulated by external stimuli? In seeking to answer this question we had the idea of adding salt (NaCl or KCl) in large quantities to a foam formed from one of the most common soaps, sodium dodecyl sulfate (SDS). Without salt, the foam destabilizes within hours whereas above a threshold concentration of salt, the life of the foam is extended for more than six months! This is due to the presence of salt that induces the formation of soap crystals within the foam. The crystals are also found on the bubble surfaces, where they make the bubbles very stable. In addition, if such "ultrastable" foam is heated above the melting point of the crystals (~ 50°C), it regains its original properties and collapses within hours.

L. Zhang[a,b], A. Mikhailovskaya[a], P. Yazhgur[a], F. Muller[c,d], F. Cousin[c], D. Langevin[a], N. Wang[b], A.Salonen[a].

a Laboratoire de Physique des Solides, Orsay, France
b Key Laboratory of Space Applied Physics and Chemistry Northwestern Polytechnical University, Xi'an, China
c Laboratoire Léon Brillouin CEA/CNRS UMR 12, Gif sur Yvette, France
d Laboratoire des Interfaces Complexes et de l'Organisation Nanométrique, Paris, France

anniina.salonen@u-psud.fr

Foams are found in a wide variety of applications in industry and personal life, such as firefighting, enhanced oil recovery, mineral flotation, food processing, and personal care products. In some of these applications good foam stability is extremely important. All foams are thermodynamically unstable and are destined to disappear [1]. To prolong their life, various types of stabilizing agents are used, such as surfactants, polymers, proteins, or particles. These stabilizing agents adsorb onto the surfaces of the bubbles and slow down the different mechanisms by which foams age: the drainage of the liquid in the foam under the effect of gravity and the disappearance of the smaller bubbles in favor of larger ones under the combined action of ripening (the small droplets are emptied into large due to the difference in Laplace pressure) and coalescence.

The properties of foams depend strongly on the stabilizers used. If using small surfactants such as soaps, the foamability, *i.e.* the amount of gas that it is possible to incorporate during the foam formation, will be very good because these small molecules rapidly migrate to the interfaces to help stabilize them. Foams have however a short life with such surfactants. On the contrary, if nanoparticles are used, they will adsorb in an almost irreversible way onto the interfaces and very stable foams are obtained because such interfaces become very elastic. On the other hand, the foamability of these nanoparticles-based foams is generally poor.

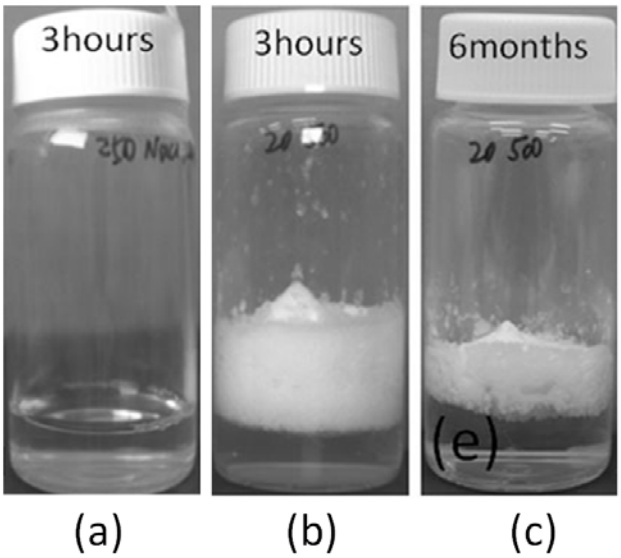

***Figure 1** : Pictures of foams made from aqueous solutions of SDS: (a) no added salt, 3 hours after foam formation; (b) with 500 mM KCl, 3 hours after foam formation; (c) with 500 mM KCl, 6 months after formation.*

We have merged these two approaches to make foams with a perfect foamability while being "ultrastable" with a good foamability with a very simple idea [2] : an addition of a large amount of salt (NaCl or KCl) in a foam formed based on one of the most common soaps, sodium dodecyl

sulfate (SDS) [1]. Without salt, the foam destabilizes within hours whereas above a threshold concentration of salt, the life of the foam is extended for more than six months (see Fig. 1)! This is because the presence of salt causes the formation of soap crystals within the foam. These crystals are found on the surfaces of the bubbles, and they block both coalescence and ripening. Their accumulation in the liquid channels also limits drainage.

The formation of such crystals was demonstrated by SANS experiments performed directly within the foam containing respectively either NaCl or KCl (Fig 2).

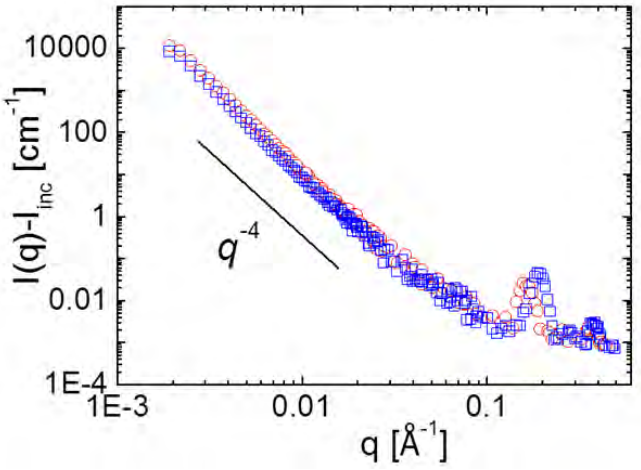

***Figure 2**: The scattered intensity as a function of the scattering wavevector for a foam prepared with 69 mm SDS and 500 mm NaCl (red circles) and 500 mm KCl (blue squares).*

The scattered intensity shows a q^{-4} decay at low q that is typical of sharp interfaces, such as the surfaces of the bubbles and the crystallites (Porod law). At large q, there are two peaks arising from the crystal structure in Figure 3b. With NaCl, the first peak is at q*=0.16 $Å^{-1}$ and the second at 0.32 $Å^{-1}$, thus twice the first; with KCl, q*=0.19 $Å^{-1}$ and the second order is at 0.38 $Å^{-1}$. The structure of SDS crystals has been previously measured [3]; they have been shown to have a lamellar structure where the interplanar distance d ($2\pi/q^*$) depends on the degree of chain tilt and hydration. The value measured for the SDS crystals crystallized from water (precipitated with NaCl or KCl) are similar to those we measured in foams.

Moreover, if this foam is heated above the Krafft temperature, i.e. the melting temperature of the soap crystals, around 50 ° C, it regains its original properties. Indeed, owing to the disappearance of crystals, it collapsed again in a few hours. The foam is therefore not only highly stable at room temperature but also thermostimulable.

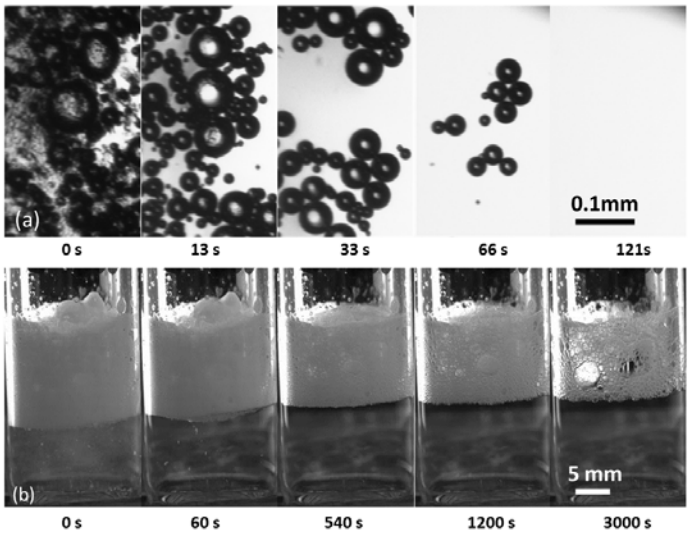

***Figure 3**: a) Bubbles and b) foams prepared with 69 mm SDS and 500 mm KCl heated suddenly to 51°C*

References

1. (a) D. Weaire, S. Hutzler, The Physics of Foams, OxfordUniversity Press, Oxford, 1999; b) I. Cantat, S. Cohen-Addad,F. Elias, F. Graner, R. Hçhler, O. Pitois, F. Rouyer, A. SaintJalmes, Les Mousses: Structure et Dynamique, Belin, 2011.

*2. L. Zhang, A. Mikhailovskaya, P. Yazhgur, F. Muller, F. Cousin, D. Langevin, N. Wang, A. Salonen, Angew. Chem. Int. Ed,. **127(33)**, 9669–9672, 2015.*

*3. AL. A. Smith, A. Duncan, G. B. Thomson, K. J. Roberts, D. Machin, G. McLeod, J. Cryst. Growth, **263**, 480 – 490, 2004.*

Unraveling the mechanisms of stabilization of Pickering emulsions by cellulose nanocrystals by SANS

In order to probe the mechanisms of stabilization of Pickering by cellulose nanocrystals, we performed SANS experiments with various contrasts to obtain a refined description of the interface. Remarkably, we showed that the thickness of the interfacial layer calculated from the SANS measurements revealed a 7 nm thickness, irrespective of the amount of CNCs, which exactly corresponds to the thickness of a nanocrystal. This demonstrates that only a single monolayer is formed at the water/oil interface.

F. Cherhal[a], F. Cousin[b], I. Capron[a]

a UR1268 Biopolymères Interactions Assemblages, Nantes, France
b Laboratoire Léon Brillouin CEA/CNRS UMR 12, Gif sur Yvette, France

isabelle.capron@ nantes.inra.fr

Increasing environmental awareness is prompting scientists and manufacturers to develop strategies for environmental sustainability by using processes and materials with low cost, low energy consumption and low toxicity, together with high biodegradability. In this framework, biobased nanoparticles are good candidates to stabilize emulsions, replacing commonly used surfactants that are generally derived from the petrochemical industry and only a small fraction is of plant origin [1]. This would be of great interest since emulsions are widely used in various application domains such as food, cosmetics, pharmaceuticals, and coatings. It is known that solid particles of colloidal size can be strongly adsorbed at oil/water interfaces, forming the so-called Pickering emulsions, or more generally, solid-stabilized emulsions. Among the particles generally used, non-spherical nanoparticles (e.g., rods, sheets, wedges, disk-like, and needle -like particles, etc.) are sparsely used whereas they can be more efficient in stabilizing emulsions than spherical ones.

Here, we aim at stabilizing emulsions by cellulose nanocrystals (CNCs) obtained from the hydrolysis of cellulose fibers, one of the main available biodegradable and sustainable molecules existing in nature. The CNCs are crystalline solid nanometer-sized rod-like particles. In the case of cotton, CNCs are composed of 3−4 laterally associated elementary crystallites and their thickness is that of one crystallite. Their overall dimensions values are around are 195 nm in length, 22 nm in width, and 6 nm in thickness, as measured by SANS [2].

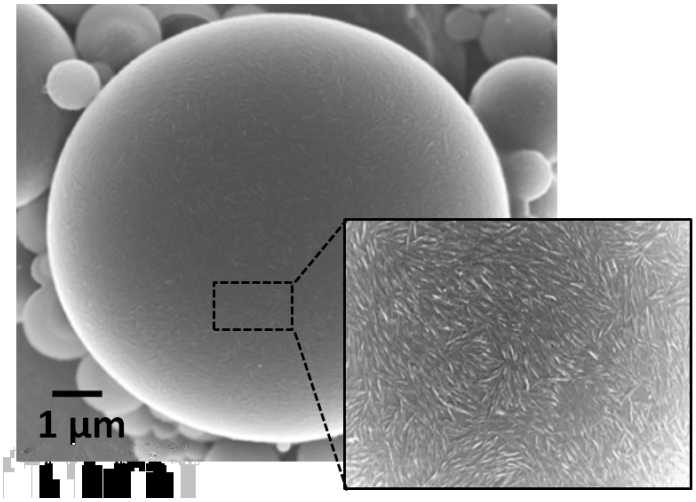

Figure 1 *: Powder SEM images of polymerized styrene-in-water emulsions based on CNCs at two different magnifications.*

Recent work showed that highly stable oil-in-water Pickering emulsions may be stabilized using such cellulose CNCs that form a dense 2D interfacial network, as shown in Figure 1. The adsorption process of the CNCs at the oil−water interface was attributed to the (200) crystalline edge plane that is the more hydrophobic face of the CNC and orients toward the oil phase. The properties of these systems in terms of stability and mechanical behavior are due to the irreversible particle adsorption and steric barrier to coalescence. However, it is still not clear the way CNCs adsorb at the interface and the way they assemble to provide a steric barrier that avoids coalescence.

In order to get an insight of the process of absorption of CNCs, we made SANS experiments directly on emulsions.

The droplets having characteristic sizes that are much greater than those that can be probed to neutrons (5 to 10 µm in diameter), the signal measured depends only on their interface. The characterization is then based on the idea of using three different contrasts to depict this interface in three different ways [3] (Fig 2).

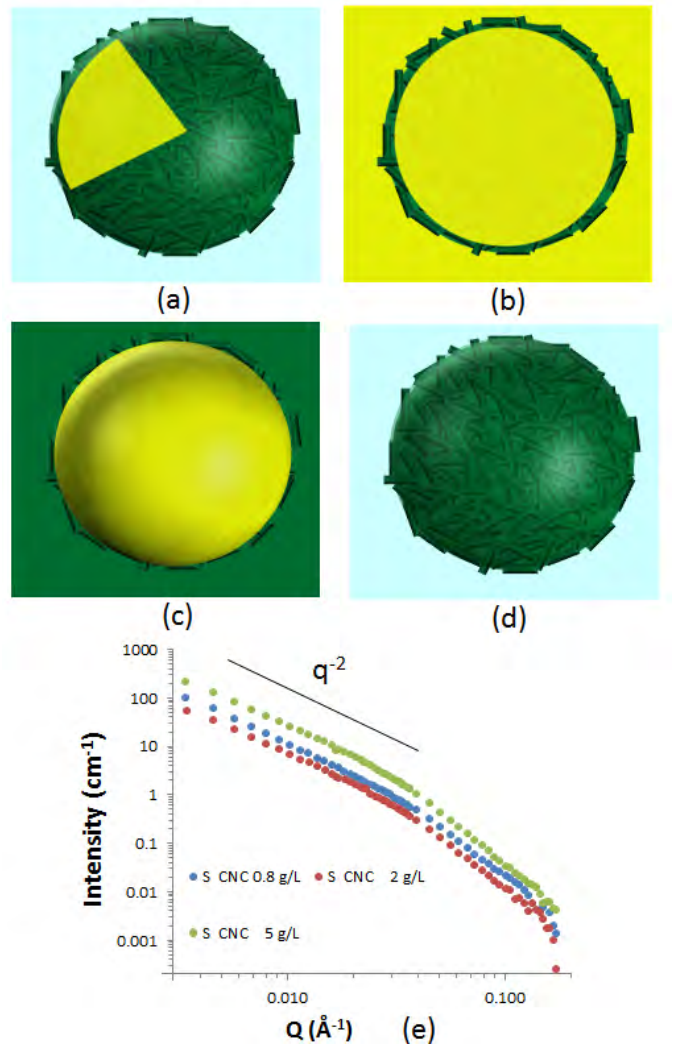

***Figure 2**: Concept of contrast variation applied to emulsion geometry: (a) schematic representation of the system, water is in blue, oil in yellow and CNCs in green; (b) the water and oil have similar SLD values; (c) the CNCs are contrast-matched to water; (d) the CNCs are contrast-matched to oil; (e) typical SANS scattering in the "water=oil" case).*

First, the contrast of the water is adjusted to that of oil. The interface is then seen as an infinite plane from neutrons point of view, the signal thereby presenting an overall decay like q^{-2}. A Guinier approximation is then used to directly determine the film thickness. The other two measurements are variations around the Porod's law. The contrast of the water or the contrast of oil are respectively adjusted to that of CNCs, then the signal comes from the scattering by the surface of the droplets. It is then possible to determine whether, for each of these two conditions, the interface is perfectly smooth, i.e. if the signal decays like q^{-4}, or is rough, in order to establish whether the CNCs plunge into one or both liquid phases.

Various emulsions were probed including different CNC concentrations in water from 0.8 to 5 g/L, and for CNCs that are either neutral or bearing some charges at their surface [4]. For the charged CNCs, the thickness of the interfacial layer calculated from the SANS measurements revealed a 7 nm thickness, irrespective of the amount of CNCs, which exactly correspond to the formation of a single monolayer. This suggests the following mechanism for the emulsion formation: at low CNCs' content, the size of the emulsions droplet radius decreases when increasing the CNCs' concentration at fixed surface coverage in order to account for the increase of specific surface associated to the monolayer formation. When the radius has reached the minimal value allowing the rod-like CNC to accommodate the curvature, there is a densification of the interface that might correspond to a local orientation/alignment of the CNCs. More aggregated neutral CNCs led to a more porous and heterogeneous surface, 18 nm thick, due to densification of the larger aggregates and resulting in a more rigid armor. Finally, the measurements in Porod conditions demonstrate that the CNCs do not dive into oil.

References

*1. P. Fratzl, R. Weinkamer, Prog. Mater. Sci., **52 (8)**, 1263–1334, 2007.*

*2. F. Cherhal, F. Cousin, I. Capron, Langmuir, **31**(20), 5596–5602, 2015.*

*3. J.Jestin, S. Simon, L. Zupancic, I. Barre, L. Langmuir, **23**, 10471–10478 2007.*

*4. F.Cherhal, F.Cousin, I.Capron, Biomacromolecules, **17 (2)**, 496–502, 2016.*

Neutron imaging of meat during cooking

The main aim of the present study was to follow the impact of temperature during meat cooking at molecular scale by spectroscopy (mainly fluorescence and visible), describing biochemical reactions occurring among muscle proteins, to correlate them to organoleptic characteristics (texture, color). To provide structural information at a microscopic scale (currently > 100 µm), we performed neutron-imaging experiments on the new LLB neutron imaging station (IMAGINE). We observed hemeproteins denaturation during online cooking. Thanks to coupled measurements obtained by neutron imaging and visible spectroscopy, we were able to link the denaturation of myoglobin to previous myofibrils contraction and water migration.

S. Scussat[a], F. Ott[b], A. Helary[b], S. Desert[b], Olivier Gaiffe[c], Christian Pierralli[c], Bruno Wacogne[c], P. Cayot [a], C. Loupiac[a,b]

a AgroSup Dijon, Université de Bourgogne-Franche Comté, Dijon, France
b Laboratoire Léon Brillouin CEA/CNRS UMR 12, Gif sur Yvette, France
c Laboratoire FEMTO-ST, UMR 6174, Université de Bourgogne-Franche Comté, CNRS, Besançon, France

camille.loupiac@agrosupdijon.fr

Open Food System (OFS) is an industrial innovation project having as one main goal the development of "smart" domestic appliances, which can pilot cooking process of meat and fish without any human intervention. Previous studies on muscle cooking have often only observed their macroscopic changes (texture, colour, flavour) and validate the levels of cooking through sensorial analysis. However, it is well known that during cooking, several structural changes can take place in the meat, such as protein denaturation and the increase in the fraction of free water contributing to drip loss.

The purpose of the project has been to study the impact of heating on beef meat at molecular scale, observing conformational changes of proteins (myofibril, collagen and myoglobin) due to temperature application, with spectroscopic methods (visible and fluorescence) and at microscopic scale, by neutron imaging. Finally, we have been able to correlate structural information got from these technics to macroscopic analysis (texture, colour, flavour).

An oven has been equipped with an optical fiber to perform fluorescence and visible spectroscopy and positioned in the neutron imaging beamline during heating process. Slices of beef (2mm in thickness) have been placed in an aluminium cell equipped with quartz windows to allow the spectroscopic measurements. During the cooking process, neutron imaging acquisition is realised. Figure 1 shows an example of collected image.

Morphology changes have been determined by analyzing number of pixels related to the sample of each image acquired during the process. Figure 2 presents the ratio of pixel between an image at a specific temperature (Pixel Im (i)) and the first image (Pixel Im(0)).

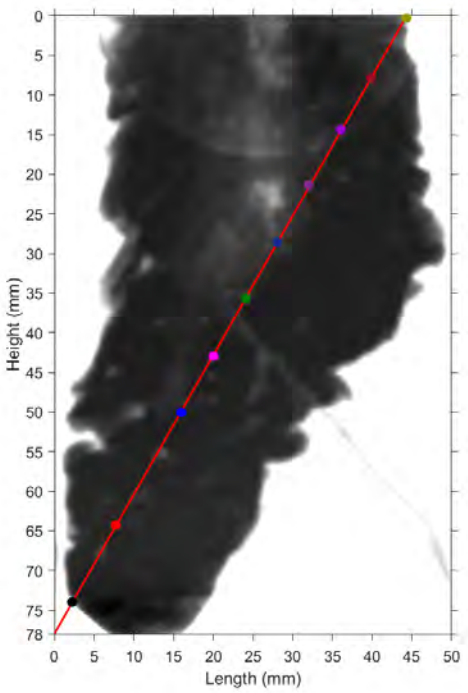

***Figure 1** : Example of normalized neutron image of a 2mm thick slice of beef presented in transmission mode. The image presents a half circle representing the window where spectroscopic measurements are realized. Each color dots on sample diagonal have been chosen to follow attenuation evolution during the cooking process.*

Morphological analysis highlights a slight contraction of the samples in temperature range between 50 and 60 °C which can be associated with myosin denaturation (around 45 °C

[1]) and the consequent lateral shrinkage of fibers. Larger loss in surface is observed over 80 °C, after denaturation of collagen (between 55 and 68 °C) and longitudinal muscular fibre contractions [2].

Thanks to the optical fiber positioned in the oven, visible

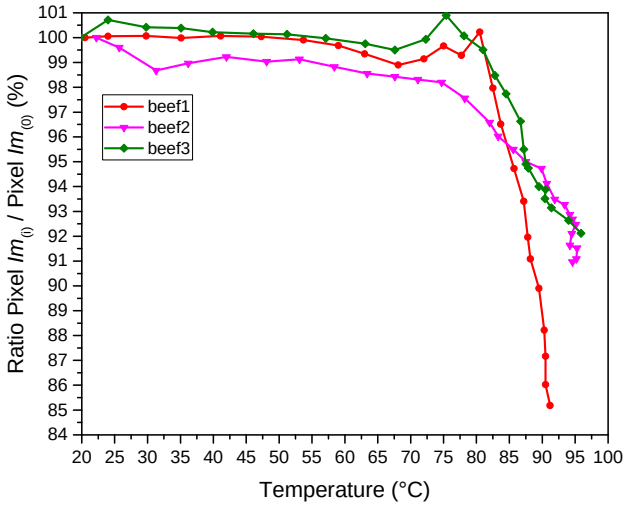

***Figure 2**: Morphology evolution of three samples of beef as function of the temperature.*

reflectance spectra have been recorded on the same sample during cooking process (Figure 3).

The two characteristic bands (544 and 580 nm) of oxymyoglobin can be observed on these spectra from 20°C to 75°C. Increasing cooking temperature, myoglobin denaturation occurs, producing met- myoglobin, therefore intensity of 580 nm band decreases. In fact, precise analy-

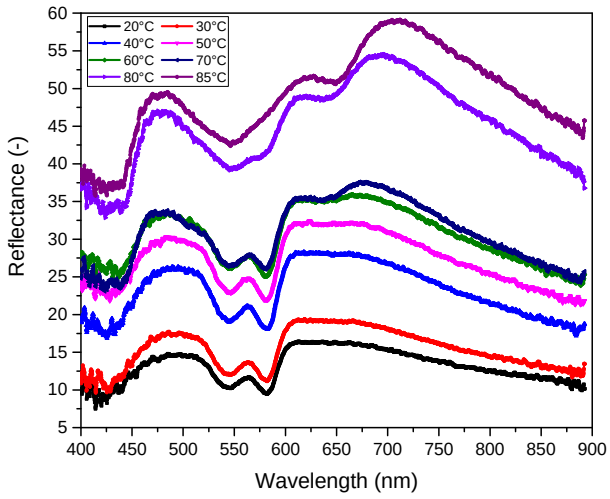

Figure 3: Collected visible spectra (reflection mode) on beef slice. Data collection is realised during the cooking process placing the optical fibre inside the oven cavity.

sis of the spectra highlights slight changes of the oxymyoglobin bands as soon as 50 °C.

In fact, as observed with the two instruments (neutron imaging and visible spectroscopy), by increasing temperature, gradually cellular microstructure tends to reorganize itself becoming tighter. Water is forced to get out from internal microstructure towards outside following loss of internal spaces. Following these fibers denaturation, hemeproteins are released with the juice and their denaturation occurs.

Neutron imaging is a technique that allows working with large objects (about 10 cm x 6 cm), but not very thick, especially if their hydrogen content is high [3]. Moreover, neutron imaging easily permits installation of a particular real sample environment, here a semi-professional oven (55 cm x 54.5 cm x 38 cm). Furthermore, neutron imaging allows performing coupled analysis. We used an optical fiber installed in the oven cavity to follow evolution of a second sample probe (myoglobin) during the process of meat cooking.

References

1. D.J. Wright, I.B. Leach, P. Wilding, J. Science of Food and Agriculture, 28, 557, 1977

2. J.R. Bendall, D.J. Restall, Meat Science,8, 93, 1983

3. S. Scussat, F. Ott, A. Hélary, S. Desert, P. Cayot, C. Loupiac, Food Biophysics, 2016

Publications

1 Abbas, S., **Desert, S.**, **Brulet, A.**, **Thevenot, V.**, **Permingeat, P.**, **Lavie, P.** & **Jestin, J.** On the design and experimental realization of a multislit-based very small angle neutron scattering instrument at the European Spallation Source. *Journal of Applied Crystallography* **48**, 1242-1253, (2015).

2 Akola, J., **Beuneu, B.**, Jones, R. O., Jovari, P., Kaban, I., Kolar, J., Voleska, I. & Wagner, T. Structure of amorphous Ag/Ge/S alloys: experimentally constrained density functional study. *Journal of Physics-Condensed Matter* **27**, (2015).

3 Al Saghir, K., Chenu, S., Veron, E., Fayon, F., Suchomel, M., Genevois, C., **Porcher, F.**, Matzen, G., Massiot, D. & Allix, M. Transparency through Structural Disorder: A New Concept for Innovative Transparent Ceramics. *Chemistry of Materials* **27**, 508-514, (2015).

4 Anoufa, M., **Kiat, J. M.** & Bogicevic, C. Electrocaloric effect in core-shell ferroelectric ceramics: Theoretical approach and practical conclusions. *Applied Physics Letters* **107**, (2015).

5 Arnould, A., Gaillard, C. & Fameau, A. L. pH-responsive fatty acid self-assembly transition induced by UV light. *Journal of Colloid and Interface Science* **458**, 147-154, (2015).

6 Arnould, A., Perez, A. A., Gaillard, C., Douliez, J. P., **Cousin, F.**, Santiago, L. G., Zemb, T., Anton, M. & Fameau, A. L. Self-assembly of myristic acid in the presence of choline hydroxide: Effect of molar ratio and temperature. *Journal Of Colloid And Interface Science* **445**, 285-293, (2015).

7 Assifaoui, A., Lerbret, A., Uyen, H. T. D., Neiers, F., Chambin, O., **Loupiac, C.** & **Cousin, F.** Structural behaviour differences in low methoxy pectin solutions in the presence of divalent cations (Ca^{2+} and Zn^{2+}): a process driven by the binding mechanism of the cation with the galacturonate unit. *Soft Matter* **11**, 551-560, (2015).

8 **Audonnet, F.**, **Brodie-Linder, N.**, Morineau, D., Frick, B. & **Alba-Simionesco, C.** From the capillary condensation to the glass transition of a confined molecular liquid: Case of toluene. *Journal Of Non-Crystalline Solids* **407**, 262-269, (2015).

9 Azzam, F., Moreau, C., **Cousin, F.**, **Menelle, A.**, Bizot, H. & Cathala, B. Reversible Modification of Structure and Properties of Cellulose Nanofibril-Based Multi layered Thin Films Induced by Postassembly Acid Treatment. *Langmuir* **31**, 2800-2807, (2015).

10 Baum, M., Komarek, A. C., Holbein, S., Fernandez-Diaz, M. T., **Andre, G.**, Hiess, A., **Sidis, Y.**, Steffens, P., Becker, P., Bohaty, L. & Braden, M. Magnetic structure and multiferroic coupling in pyroxene $NaFeSi_2O_6$. *Physical Review B* **91**, 214415, (2015).

11 Belieres, M., Chouini-Lalanne, N. & Dejugnat, C. Synthesis, self-assembly, and catalytic activity of histidine-based structured lipopeptides for hydrolysis reactions in water. *Rsc Advances* **5**, 35830-35842, (2015).

12 Benoit, A., Paillard, P., Baudin, T., **Klosek, V.** & Mottin, J. B. Comparison of four arc welding processes used for aluminium alloy cladding. *Science and Technology of Welding and Joining* **20**, 75-81, (2015).

13 Besnard, L., Protat, M., Malloggi, F., Daillant, J., **Cousin, F.**, Pantoustier, N., Guenoun, P. & Perrin, P. Breaking of the Bancroft rule for multiple emulsions stabilized by a single stimulable polymer (vol 10, 7073, 2014). *Soft Matter* **11**, 1026-1026, (2015).

14 Betanda, Y. A., Helbert, A. L., Brisset, F., **Mathon, M. H.**, Waeckerle, T. & Baudin, T. Effect of microalloying elements on the Cube texture formation of Fe48% Ni alloy tapes. *17th International Conference On Textures Of Materials (Icotom 17)* **82**, (2015).

15 Bettoschi, A., Bencini, A., Berti, D., Caltagirone, C., Conti, L., Demurtas, D., Giorgi, C., Isaia, F., Lippolis, V., Mamusa, M. & Murgia, S. Highly stable ionic liquid-in-water emulsions as a new class of fluorescent sensors for metal ions: the case study of Fe^{3+} sensing. *Rsc Advances* **5**, 37385-37391, (2015).

16 Bogicevic, C., Thorner, G., Karolak, F., Haghi-Ashtiani, P. & **Kiat, J. M.** Morphogenesis mechanisms in the solvothermal synthesis of $BaTiO_3$ from titanate nanorods and nanotubes. *Nanoscale* **7**, 3594-3603, (2015).

17 Bolloli, M., Alloin, F., Kalhoff, J., Bresser, D., Passerini, S., **Judeinstein, P.**, Lepretre, J. C. & Sanchez, J. Y. Effect of carbonates fluorination on the properties of LiTFSI-based electrolytes for Li-ion batteries. *Electrochimica Acta* **161**, 159-170, (2015).

18 Bonetti, M., Nakamae, S., Huang, B. T., Salez, T. J., Wiertel-Gasquet, C. & Roger, M. Thermoelectric energy recovery at ionic-liquid/electrode interface. *Journal of Chemical Physics* **142**, (2015).

19 Borisova, O. V., Billon, L., Cernochova, Z., **Lapp, A.**, Stepanek, P. & Borisov, O. V. Effect of Temperature on Self-Assembly of Amphiphilic Block-Gradient Copolymers of Styrene and Acrylic Acid. *Macromolecular Symposia* **348**, 25-32, (2015).

20 Boudvillain, M., **Arluison, V.** & Taghbalout, A. in *RNA Remodeling Proteins* Vol. 1259 *Methods in Molecular Biology* 87-101 (Springer New York, 2015).

21 Bouyrie, Y., Candolfi, C., Pailhes, S., Koza, M. M., Malaman, B., Dauscher, A., Tobola, J., Boisron, O., Saviot, L. & Lenoir, B. From crystal to glass-like thermal conductivity in crystalline minerals. *Physical Chemistry Chemical Physics* **17**, 19751-19758, (2015).

22 Boyer, M., Veron, E., Becerro, A. I., **Porcher, F.**, Suchomel, M. R., Matzen, G. & Allix, M. BaGa4O7, a new A(3)BC(10)O(20) crystalline phase: synthesis, structural determination and luminescence properties. *Crystengcomm* **17**, 6127-6135, (2015).

23 Caspi, E. a. N., Chartier, P., **Porcher, F.**, **Damay, F.** & Cabioc'h, T. Ordering of (Cr,V) Layers in Nanolamellar $(Cr_{0.5}V_{0.5})_{n+1}AlC_n$ Compounds. *Materials Research Letters* **3**, 100, (2015).

24 **Cayrol, B.**, **Fortas, E.**, Martret, C., Cech, G., Kloska, A., **Caulet, S.**, Barbet, M., Trepout, S., Marco, S., Taghbalout, A., Busi, F., Wegrzyn, G. & **Arluison, V.** Riboregulation of the bacterial actin-homolog MreB by DsrA small noncoding RNA. *Integrative Biology* **7**, 128-141, (2015).

25 Ceretti, M., Wahyudi, O., **Cousson, A.**, Villesuzanne, A., Meven, M., Pedersen, B., Bassat, J. M. & Paulus, W. Low temperature oxygen diffusion mechanisms in Nd_2NiO^{4+}delta and Pr2NiO4+delta via large anharmonic displacements, explored by single crystal neutron diffraction. *Journal of Materials Chemistry A* **3**, 21140-21148, (2015).

26 Charbonnier, V., Zhang, J. X., Monnier, J., Goubault, L., Bernard, P., Magen, C., Serin, V. & Latroche, M. Structural and Hydrogen Storage Properties of Y_2Ni_7 Deuterides Studied by Neutron Powder Diffraction. *Journal of Physical Chemistry C* **119**, 12218-12225, (2015).

27 Chattopadhyay, S., Baledent, V., Auban-Senzier, P., Pasquier, C., Doubroysky, C., Greenblatt, M. & Foury-Leylekian, P. Thermodynamic and neutron diffraction studies on multiferroic $NdMn_2O_5$. *Physica B-Condensed Matter* **460**, 214-217, (2015).

28 Chebaane, A., Hammami, F., Nasr, S., Bahri, M. & **Bellissent-Funel, M.-C.** H-bonding network in fully deuterated N-methylformamide-water mixtures as studied by neutron scattering. Complementarity to X-ray study. *European Physical Journal E* **38**, 5, (2015).

29 Cherhal, F., **Cousin, F.** & Capron, I. Influence of Charge Density and Ionic Strength on the Aggregation Process of Cellulose Nanocrystals in Aqueous Suspension, as Revealed by Small-Angle Neutron Scattering. *Langmuir* **31**, 5596-5602, (2015).

30 Cippo, E. P., Croci, G., Muraro, A., **Menelle, A.**, Albani, G., Cavenago, M., Cazzaniga, C., Claps, G., Grosso, G., Murtas, F., Rebai, M., Tardocchi, M. & Gorini, G. A GEM-based thermal neutron detector for high counting rate applications. *Journal of Instrumentation* **10**, P10003 (10009 pp.)-P10003 (10009 pp.), (2015).

31 Cippo, E. P., Croci, G., Muraro, A., Menelle, A., Albani, G., Cavenago, M., Cazzaniga, C., Claps, G., Grosso, G., Murtas, F., Rebai, M., Tardocchi, M. & Gorini, G. A GEM-based thermal neutron detector for high counting rate applications. *Journal of Instrumentation* **10**, (2015).

32 Colmont, M., Bucataru, G., Borowiec, A., Capron, M., Dumeignil, F., Huve, M., Capet, F., **Damay, F.**, Mentre, O. & Roussel, P. Novel La3Fe(MoO4)(6) phase: magnetic properties and ethanol reactivity. *Dalton Transactions* **44**, 14444-14452, (2015).

33 Coursault, D., Blach, J. F., Grand, J., Coati, A., Vlad, A., Zappone, B., Babonneau, D., Levi, G., Felidj, N., Donnio, B., Gallani, J. L., **Alba, M.**, Garreau, Y., Borensztein, Y., Goldmann, M. & Lacaze, E. Tailoring Anisotropic Interactions between Soft Nanospheres Using Dense Arrays of Smectic Liquid Crystal Edge Dislocations. *Acs Nano* **9**, 11678-11689, (2015).

34 Cuvier, A. S., Babonneau, F., Berton, J., Stevens, C. V., **Fadda, G. C.**, Genois, I., Le Griel, P., Pehau-Arnaudet, G. & Baccile, N. Synthesis of Uniform, Monodisperse, Sophorolipid Twisted Ribbons. *Chemistry-an Asian Journal* **10**, 2419-2426, (2015).

35 Cuvier, A. S., Babonneau, F., Berton, J., Stevens, C. V., **Fadda, G. C.**, Pehau-Arnaudet, G., Le Griel, P., Prevost, S., Perez, J. & Baccile, N. Nanoscale Platelet Formation by Monounsaturated and Saturated Sophorolipids under Basic pH Conditions. *Chemistry-a European Journal* **21**, 19265-19277, (2015).

36 **Damay, F.** Neutrons and magnetic structures: analysis methods and tools. *Journal of Physics D: Applied Physics* **48**, 504005 (504008 pp.)-504005 (504008 pp.), (2015).

37 **Damay, F.**, Bazin, D., Daudon, M. & **André, G.** Neutron diffraction as a probe for the characterization of biological entities. *Comptes Rendus Chimie*, (2015).

38 **Damay, F.**, Poienar, M., Hervieu, M., Guesdon, A., **Bourgeois, J.**, Hansen, T., Elkaim, E., Haines, J., Hermet, P., Konczewicz, L., Hammouda, T., Rouquette, J. & Martin, C. High-pressure polymorph of $LuFe_2O_4$ with room-temperature antiferromagnetic order. *Physical Review B* **91**, 214111, (2015).

39 Dammak, A., Moreau, C., Azzam, F., Jean, B., **Cousin, F.** & Cathala, B. Influence of cellulose nanocrystals concentration and ionic strength on the elaboration of cellulose nanocrystals-xyloglucan multilayered thin films. *Journal of Colloid and Interface Science* **460**, 214-220, (2015).

40 Dao, T. P. T., Fernandes, F., Er-Rafik, M., Salva, R., Schmutz, M., **Brulet, A.**, Prieto, M., Sandre, O. & Le Meins, J. F. Phase Separation and Nanodomain Formation in Hybrid Polymer/Lipid Vesicles. *Acs Macro Letters* **4**, 182-186, (2015).

41 de Lima, B. S., da Luz, M. S., Oliveira, F. S., Alves, L. M. S., dos Santos, C. A. M., Jomard, F., **Sidis, Y.**, **Bourges, P.**, Harms, S., Grams, C. P., Hemberger, J., Lin, X., Fauque, B. & Behnia, K. Interplay between antiferrodistortive, ferroelectric, and superconducting instabilities in $Sr_{1-x}Ca_xTiO_{3-d}$. *Physical Review B* **91**, 045108 (2015).

42 Desmarchelier, A., Raynal, M., Brocorens, P., Vanthuyne, N. & Bouteiller, L. Revisiting the assembly of amino ester-based benzene-1,3,5-tricarboxamides: chiral rods in solution. *Chemical Communications* **51**, 7397-7400, (2015).

43 Deutsch, M., Hansen, T. C., Fernandez-Diaz, M. T., Forget, A., Colson, D., **Porcher, F.** & **Mirebeau, I.** Pressure-induced commensurate phase with potential giant polarization in YMn_2O_5. *Physical Review B* **92**, (2015).

44 Diou, O., Greco, S., Beltran, T., **Lairez, D.**, Authelin, J. R. & Bazile, D. A method to Quantify the Affinity of Cabazitaxel for PLA-PEG Nanoparticles and Investigate the Influence of the Nano-Assembly Structure on the Drug/Particle Association. *Pharmaceutical Research* **32**, 3188-3200, (2015).

45 Dirany, M., Ayzac, V., Isare, B., Raynal, M. & Bouteiller, L. Structural Control of Bisurea-Based Supramolecular Polymers: Influence of an Ester Moiety. *Langmuir* **31**, 11443-11451, (2015).

46 Echevarria-Bonet, C., Rojas, D. P., Espeso, J. I., Fernandez, J. R., Rodriguez, M. D., Barquin, L. F., Fernandez, L. R., Gorria, P., Blanco, J. A., Fdez-Gubieda, M. L., Bauer, E. & **Damay, F.** Magnetic phase diagram of superantiferromagnetic $TbCu_2$ nanoparticles. *Journal of Physics-Condensed Matter* **27**, (2015).

47 El Bahoui, A., Cadel, E., **Ott, F.**, Bordel, C. & Ledue, D. Interface local chemistry and magnetic asymmetry in (Fe/Mn) multilayers. *Physica B-Condensed Matter* **468**, 76-80, (2015).

48 El Haitami, A., Goldmann, M., **Cousin, F.**, Dosseh, G. & Cantin, S. From Homogeneous to Segregated Structure of Poly(dimethylsiloxane)/Cellulose Derivative Mixed Langmuir Films Depending on Composition: An in Situ Neutron Reflectivity Study. *Langmuir* **31**, 6395-6403, (2015).

49 Estrader, M., Lopez-Ortega, A., Golosovsky, I. V., Estrade, S., Roca, A. G., Salazar-Alvarez, G., Lopez-Conesa, L., Tobia, D., Winkler, E., Ardisson, J. D., Macedo, W. A. A., Morphis, A., Vasilakaki, M., Trohidou, K. N., **Gukasov, A.**, **Mirebeau, I.**, Makarova, O. L., Zysler, R. D., Peiro, F., Baro, M. D., Bergstrom, L. & Nogues, J. Origin of the large dispersion of magnetic properties in nanostructured

oxides: Fe_xO/Fe_3O_4 nanoparticles as a case study. *Nanoscale* **7**, 3002-3015, (2015).

50 Exare, C., **Kiat, J. M.**, Guiblin, N., **Porcher, F.** & Petricek, V. Structural evolution of ZTA composites during synthesis and processing. *Journal Of The European Ceramic Society* **35**, 1273-1283, (2015).

51 Fameau, A. L., Arnould, A., Lehmann, M. & von Klitzing, R. Photoresponsive self-assemblies based on fatty acids. *Chemical Communications* **51**, 2907 -2910, (2015).

52 Fathi, S., Gonzalez, M. A., Bahri, M., Nasr, S. & **Bellissent-Funel, M. C.** Structural investigation of liquid formic acid by X-ray and neutron scattering, ab initio calculations and molecular dynamics simulations. *Journal of Molecular Liquids* **207**, 125-135, (2015).

53 **Fortas, E.**, Piccirilli, F., **Malabirade, A.**, Militello, V., Trepout, S., Marco, S., Taghbalout, A. & **Arluison, V.** New insight into the structure and function of Hfq C-terminus. *Bioscience reports* **35**, e00190, (2015).

54 Fuchs, E. C., Bitschnau, B., Wexler, A. D., Woisetschlager, J. & Freund, F. T. A Quasi-Elastic Neutron Scattering Study of the Dynamics of Electrically Constrained Water. *Journal of Physical Chemistry B* **119**, 15892-15900, (2015).

55 Fuhrman, W. T., Leiner, J., Nikolic, P., Granroth, G. E., Stone, M. B., Lumsden, M. D., DeBeer-Schmitt, L., Alekseev, P. A., **Mignot, J. M.**, Koohpayeh, S. M., Cottingham, P., Phelan, W. A., Schoop, L., McQueen, T. M. & Broholm, C. Interaction Driven Subgap Spin Exciton in the Kondo Insulator SmB_6. *Physical Review Letters* **114**, 036401, (2015).

56 Fumagalli, M., Lyonnard, S., Prajapati, G., Berrod, Q., Porcar, L., Guillermo, A. & Gebel, G. Fast Water Diffusion and Long-Term Polymer Reorganization during Nafion Membrane Hydration Evidenced by Time-Resolved Small-Angle Neutron Scattering. *Journal of Physical Chemistry B* **119**, 7068-7076, (2015).

57 Garanger, E., MacEwan, S. R., Sandre, O., **Brulet, A.**, Bataille, L., Chilkoti, A. & Lecommandoux, S. Structural Evolution of a Stimulus-Responsive Diblock Polypeptide Micelle by Temperature Tunable Compaction of its Core. *Macromolecules* **48**, 6617-6627, (2015).

58 Grenier, B., **Petit, S.**, Simonet, V., Canevet, E., Regnault, L. P., Raymond, S., Canals, B., Berthier, C. & Lejay, P. Longitudinal and Transverse Zeeman Ladders in the Ising-Like Chain Antiferromagnet $BaCo_2V_2O_8$. *Physical Review Letters* **114**, 017201 (2015).

59 Guidi, T., **Gillon, B.**, Mason, S. A., Garlatti, E., Carretta, S., Santini, P., Stunault, A., Caciuffo, R., van Slageren, J., Klemke, B., Cousson, A., Timco, G. A. & Winpenny, R. E. P. Direct observation of finite size effects in chains of antiferromagnetically coupled spins. *Nature Communications* **6**, (2015).

60 **Guitteny, S.**, **Mirebeau, I.**, de Reotier, P. D., Colin, C. V., Bonville, P., **Porcher, F.**, Grenier, B., Decorse, C. & **Petit, S.** Mesoscopic correlations in $Tb_2Ti_2O_7$ spin liquid. *Physical Review B* **92**, (2015).

61 Hayem-Ghez, A., Ravaud, E., Boust, C., Bastian, G., Menu, M. & **Brodie-Linder, N.** Characterizing pigments with hyperspectral imaging variable false-color composites. *Applied Physics a-Materials Science & Processing* **121**, 939-947, (2015).

62 Hervieu, M., **Damay, F.**, Maignan, A. & Martin, C. Rare earth ferrites $LuFe_2O^{4\ +/-\ x}$ polymorphism, polytypism and metastable phases. *Solid State Sciences* **48**, A1-A16, (2015).

63 Hiraoka, Y., Ikeue, T., Sakiyama, H., Guegan, F., Luneau, D., **Gillon, B.**, Hiromitsu, I., Yoshioka, D., Mikuriya, M., Kataoka, Y. & Handa, M. An unprecedented up-field shift in the C-13 NMR spectrum of the carboxyl carbons of the lantern-type dinuclear complex TBA Ru-2(O_2CCH_3)(4)Cl-2 (TBA(+) = tetra(n-butyl)ammonium cation). *Dalton Transactions* **44**, 13439-13443, (2015).

64 Holbein, S., Steffens, P., Finger, T., Komarek, A. C., **Sidis, Y.**, Link, P. & Braden, M. Field and temperature dependence of electromagnon scattering in $TbMnO_3$ studied by inelastic neutron scattering. *Physical Review B* **91**, 014432 (2015).

65 Hui, G., **Brulet, A.**, Rajamohanan, P. R., Marcellan, A., Sanson, N. & Hourdet, D. Influence of topology of LCST-based graft copolymers on responsive assembling in aqueous media. *Polymer* **60**, 164-175, (2015).

66 Ikeuchi, K., Kobayashi, Y., Suzuki, K., Itoh, M., Kajimoto, R., **Bourges, P.**, Christianson, A. D., Nakamura, H., Machida, M. & Sato, M. Phonons of Fe-based superconductor $Ca_{10}Pt_4As_8(Fe_{1-x}Pt_x As)_{10}$. *Journal of physics. Condensed matter : an Institute of Physics journal* **27**, 465701, (2015).

67 Ivanov, S. A., Tellgren, R., **Porcher, F.**, **Andre, G.**, Ericsson, T., Nordblad, P., Sadovskaya, N., Kaleva, G., Politova, E., Baldini, M., Sun, C., Arvanitis, D., Kumar, P. A. & Mathieu, R. Structural and magnetic properties of nickel antimony ferrospinels. *Materials Chemistry And Physics* **158**, 127-137, (2015).

68 Jensen, M. H., Alba-Simionesco, C., Niss, K. & Hecksher, T. A systematic study of the isothermal crystallization of the mono-alcohol n-butanol monitored by dielectric spectroscopy. *Journal of Chemical Physics* **143**, (2015).

69 Ji, P. F., Yang, Z. Y., Zhang, J., Zheng, L., Ji, V. & **Klosek, V.** Residual stress distribution and microstructure in the friction stir weld of 7075 aluminum alloy. *Journal of Materials Science* **50**, 7262-7270, (2015).

70 Jiang, K., Zhang, C., Guttula, D., Liu, F., van Kan, J. A., Lavelle, C., **Kubiak, K.**, **Malabirade, A.**, **Lapp, A.**, **Arluison, V.** & van der Maarel, J. R. C. Effects of Hfq on the conformation and compaction of DNA. *Nucleic Acids Research* **43**, 4332-4341, (2015).

71 Jovari, P., Cui, S., Nazabal, V., Kaban, I., **Beuneu, B.**, Dussauze, M., Boussard-Pledel, C. & Bureau, B. Network Rearrangement in AgI-Doped $GeTe_4$ Glasses. *Journal Of The American Ceramic Society* **98**, 1034-1039, (2015).

72 Kaban, I., Jovari, P., Escher, B., Tran, D. T., Svensson, G., Webb, M. A., Regier, T. Z., Kokotin, V., **Beuneu, B.**, Gemming, T. & Eckert, J. Atomic structure and formation of CuZrAl bulk metallic glasses and composites. *Acta Materialia* **100**, 369-376, (2015).

73 **Kahl, P.**, **Baroni, P.** & **Noirez, L.** Harmonic strain-optical response revealed in the isotropic (liquid) phase of liquid crystals. *Applied Physics Letters* **107**, (2015).

74 Kozhevnikov, S. V., Ignatovich, V. K., Nikitenko, Y. V., **Ott, F.** & Petrenko, A. V. System of neutron microbeams from a planar waveguide. *Jetp Letters* **102**, 1-6, (2015).

75 Krannich, S., **Sidis, Y.**, **Lamago, D.**, Heid, R., **Mignot, J. M.**, von Lohneysen, H. V., Ivanov, A., Steffens, P., Keller, T., Wang, L., Goering, E. & Weber, F. Magnetic moments induce strong phonon renormalization in FeSi. *Nature Communications* **6**, (2015).

76 Lagorce-Tachon, A., Karbowiak, T., **Loupiac, C.**, Gaudry, A., **Ott, F.**, **Alba-Simionesco, C.**, Gougeon, R. D., Alcantara, V., Mannes, D., Kaestner, A., Lehmann, E. & Bellat, J. P. The cork viewed from the inside. *Journal Of Food Engineering* **149**, 214-221, (2015).

77 Lange, F., **Judeinstein, P.**, Franz, C., Hartmann-Azanza, B., Ok, S., Steinhar, M. & Saalwachter, K. Large-Scale Diffusion of Entangled Polymers along Nanochannels. *Acs Macro Letters* **4**, 561-565, (2015).

78 Larbi, F. H., Azzeddine, H., Baudin, T., **Mathon, M.-H.**, Brisset, F., Helbert, A.-L., Kawasaki, M., Bradai, D. & Langdon, T. G. Microstructure and texture evolution in a Cu-Ni-Si alloy processed by equal-channel angular pressing. *Journal Of Alloys And Compounds* **638**, 88-94, (2015).

79 **Le Caeur, C.**, **Combet, S.**, **Carrot, G.**, Busch, P., **Teixeira, J.** & **Longeville, S.** Conformation of the Poly (ethylene Glycol) Chains in DiPEGylated Hemoglobin Specifically Probed by SANS: Correlation with PEG Length and in Vivo Efficiency. *Langmuir* **31**, 8402-8410, (2015).

80 Le Floch, S., Balima, F., Pischedda, V., Legrand, F. & San-Miguel, A. Small angle scattering methods to study porous materials under high uniaxial strain. *Review of Scientific Instruments* **86**, (2015).

81 Leguy, A. M. A., Frost, J. M., McMahon, A. P., Sakai, V. G., Kochelmann, W., Law, C. H., Li, X. E., Foglia, F., Walsh, A., O'Regan, B. C., Nelson, J., Cabral, J. T. & Barnes, P. R. F. The dynamics of methylammonium ions in hybrid organic-inorganic perovskite solar cells. *Nature Communications* **6**, (2015).

82 **Leroy, M. A.**, **Bataille, A. M.**, Wang, Q., Fitzsimmons, M. R., Bertran, F., Le Fevre, P., Taleb-Ibrahimi, A., Vlad, A., Coati, A., Garreau, Y., Hauet, T., Gatel, C., **Ott, F.** & Andrieu, S. Enhanced magnetization at the Cr/MgO(001) interface. *Applied Physics Letters* **107**, 251602 (251605 pp.)-251602 (251605 pp.), (2015).

83 Lhotel, E., **Petit, S.**, **Guitteny, S.**, Florea, O., Hatnean, M. C., Colin, C., Ressouche, E., Lees, M. R. & Balakrishnan, G. Fluctuations and All-In -All-Out Ordering in Dipole-Octupole Nd2Zr2O7. *Physical Review Letters* **115**, (2015).

84 Li, M., Bresson, B., **Cousin, F.**, Fretigny, C. & Tran, Y. Submicrometric Films of Surface-Attached Polymer Network with Temperature-Responsive Properties. *Langmuir* **31**, 11516-11524, (2015).

85 Livi, S., Bugatti, V., Marechal, M., Soares, B. G., Barra, G. M. O., Duchet-Rumeau, J. & Gerard, J.-F. Ionic liquids-lignin combination: an innovative way to improve mechanical behaviour and water vapour permeability of eco-designed biodegradable polymer blends. *Rsc Advances* **5**, 1989-1998, (2015).

86 Louhichi, A., Tamborini, E., Oberdisse, J., Cipelletti, L. & Ramos, L. Viscoelasticity of colloidal polycrystals doped with impurities. *Physical Review E* **92**, (2015).

87 Louisfrema, W., Rotenberg, B., Porcher, F., Paillaud, J. L., Massiani, P. & Boutin, A. Cation redistribution upon dehydration of Na58Y faujasite zeolite: a joint neutron diffraction and molecular simulation study. *Molecular Simulation* **41**, 1371-1378, (2015).

88 Luneville, L., Largeau, L., Deranlot, C., Ribis, J., **Ott, F.**, Moncoffre, N., Baldinozzi, G. & Simeone, D. Interdiffusion processes at irradiated Cr/Si interfaces. *Journal Of Alloys And Compounds* **626**, 65-69, (2015).

89 Malikova, N., Rollet, A. L., Cebasek, S., Tomsic, M. & Vlachy, V. On the crossroads of current polyelectrolyte theory and counterion-specific effects. *Physical Chemistry Chemical Physics* **17**, 5650-5658, (2015).

90 Mamusa, M., Sirieix-Plenet, J., Perzynski, R., **Cousin, F.**, Dubois, E. & Peyre, V. Concentrated assemblies of magnetic nanoparticles in ionic liquids. *Faraday Discussions* **181**, 193-209, (2015).

91 Manet, S., Cuvier, A. S., Valotteau, C., **Fadda, G. C.**, Perez, J., Karakas, E., Abel, S. & Baccile, N. Structure of Bolaamphiphile Sophorolipid Micelles Characterized with SAXS, SANS, and MD Simulations. *Journal of Physical Chemistry B* **119**, 13113-13133, (2015).

92 **Mangin-Thro, L.**, **Sidis, Y.**, Wildes, A. & **Bourges, P.** Intra-unit-cell magnetic correlations near optimal doping in $YBa_2Cu_3O_{6.85}$. *Nature Communications* **6**, (2015).

93 Marczak, W., Holaj-Krzak, J. T., Lodowski, P., Almasy, L. & **Fadda, G. C.** Hydrogen-bonded aggregates in the mixtures of piperidine with water: Thermodynamic, SANS and theoretical studies. *Chemical Physics Letters* **619**, 77-83, (2015).

94 Marechal, M., Niepceron, F., Gebel, G., Mendil-Jakani, H. & Galiano, H. Inside the structure of a nanocomposite electrolyte membrane: how hybrid particles get along with the polymer matrix. *Nanoscale* **7**, 3077, (2015).

95 Marechal, M., Niepceron, F., Gebel, G., Mendil-Jakani, H. & Galiano, H. Inside the structure of a nanocomposite electrolyte membrane: how hybrid particles get along with the polymer matrix. *Nanoscale* **7**, 3077-3087, (2015).

96 **Mathon, M. H.**, Perrot, M., Poirier, L., Ratti, M., Herve, N. & de Carlanc, Y. Development of new ferritic alloys reinforced by nano titanium nitrides. *Journal Of Nuclear Materials* **456**, 449-454, (2015).

97 Mbarek, S., **Baroni, P.** & **Noirez, L.** Highlighting delayed elastic processes at zero stress in a polymer glass. *Polymer International* **64**, 1303-1308, (2015).

98 Mengucci, P., **Andre, G.**, Auffray, E., Barucca, G., Cecchi, C., Chipaux, R., **Cousson, A.**, Davi, F., Di Vara, N., Rinaldi, D. & Santecchia, E. Structural, mechanical and light yield characterisation of heat treated LYSO:Ce single crystals for medical imaging applications. *Nuclear Instruments & Methods In Physics Research Section A-Accelerators Spectrometers Detectors And Associated Equipment* **785**, 110-116, (2015).

99 **Muller, F.**, Degousee, T., Degrouard, J., **Brulet, A.** & Salonen, A. Probing structure in submicronic aqueous assemblies of emulsified microemulsions and charged spherical colloids using SANS and cryo-TEM. *Journal of colloid and interface science* **446**, 114-121, (2015).

100 Nabi, E., Drechsler, M. & Gradzielski, M. Phase behaviour and vesicle formation in catanionic mixtures of Na oleate and alkyl trimethyl ammonium bromide and its salt-free version. *Colloid and Polymer Science* **293**, 3119-3130, (2015).

101 Nguyen, H. H., **Brulet, A.**, Goudouneche, D., Saint-Aguet, P., Lauth-de Viguerie, N. & Marty, J. D. The effect of polymer branching and average molar mass on the formation, stabilization and thermoresponsive properties of gold nanohybrids stabilized by poly(N-isopropylacrylamides). *Polymer Chemistry* **6**, 5838-5850, (2015).

102 Oster, M., Hebraud, A., Gallet, S., **Lapp, A.**, Pollet, E., Averous, L. & Schlatter, G. Star-Pseudopolyrotaxane Organized in Nanoplatelets for Poly(epsilon-caprolactone)-Based Nanofibrous Scaffolds with Enhanced Surface Reactivity. *Macromolecular Rapid Communications* **36**, 292-297, (2015).

103 **Ott, F.**, Kozhevnikov, S., Thiaville, A., Torrejon, J. & Vazquez, M. Shaping micron-sized cold neutron beams. *Nuclear Instruments & Methods In Physics Research Section A-Accelerators Spectrometers Detectors And Associated Equipment* **788**, 29-34, (2015).

104 Pan, F. J., Li, X. H., Lu, F. Q., Wang, X. M., Cao, J., Kuang, X. J., Veron, E., **Porcher, F.**, Suchomel, M. R., Wang, J. & Allix, M. Nonstoichiometric Control of Tunnel-Filling Order, Thermal Expansion, and Dielectric Relaxation in Tetragonal Tungsten Bronzes $Ba_{0.5-x}TaO_{3-x}$. *Inorganic Chemistry* **54**, 8978-8986, (2015).

105 Parshall, D., Pintschovius, L., Niedziela, J. L., **Castellan, J. P.**, **Lamago, D.**, Mittal, R., Wolf, T. & Reznik, D. Close correlation between magnetic properties and the soft phonon mode of the structural transition in $BaFe_2As_2$ and $SrFe_2As_2$. *Physical Review B* **91**, 134426, (2015).

106 Patureau, P., Josse, M., Dessapt, R., Mevellec, J. Y., **Porcher, F.**, Maglione, M., Deniard, P. & Payen, C. Incorporation of Jahn-Teller Cu2+ Ions into Magnetoelectric Multiferroic MnWO4: Structural, Magnetic, and Dielectric Permittivity Properties of $Mn_{1-x}Cu_xWO_4$ ($x <= 0.25$). *Inorganic Chemistry* **54**, 10623-10631, (2015).

107 Pauly, C. S., Genix, A. C., Alauzun, J. G., Sztucki, M., **Oberdisse, J.** & Mutin, P. H. Surface modification of alumina-coated silica nanoparticles in aqueous sols with phosphonic acids and impact on nanoparticle interactions. *Physical Chemistry Chemical Physics* **17**, 19173-19182, (2015).

108 Pengfei, J., Zhongyu, Y., Jin, Z., Lin, Z., Ji, V. & **Klosek, V.** Residual stress distribution and microstructure in the friction stir weld of 7075 aluminum alloy. *Journal of Materials Science* **50**, 7262-7270, (2015).

109 Pethes, I., Chahal, R., Nazabal, V., Prestipino, C., Trapananti, A., **Pantalei, C.**, **Beuneu, B.**, Bureau, B. & Jovari, P. Short range order in Ge-Ga-Se glasses. *Journal of Alloys and Compounds* **651**, 578-584, (2015).

110 **Petit, S.**, **Guitteny, S.**, **Robert, J.**, Bonville, P., Decorse, C., Ollivier, J., Mutka, H. & **Mirebeau, I.** Spin dynamics in highly frustrated pyrochlore magnets. *Qens/Wins 2014 - 11th International Conference On Quasielastic Neutron Scattering And 6th International Workshop On Inelastic Neutron Spectrometers* **83**, (2015).

111 Portnichenko, P. Y., Cameron, A. S., Surmach, M. A., Deen, P. P., Paschen, S., Prokofiev, A., **Mignot, J. M.**, Strydom, A. M., Telling, M. T. F., Podlesnyak, A. & Inosov, D. S. Momentum-space structure of quasielastic spin fluctuations in $Ce_3Pd_{20}Si_6$. *Physical Review B* **91**, (2015).

112 Pousthomis, M., Anagnostopoulou, E., Panagiotopoulos, I., Boubekri, R., Fang, W. Q., **Ott, F.**, Atmane, K. A., Piquemal, J. Y., Lacroix, L. M. & Viau, G. Localized magnetization reversal processes in cobalt nanorods with different aspect ratios. *Nano Research* **8**, 2231-2241, (2015).

113 Prokes, K., Hartwig, S., **Gukasov, A.**, Mydosh, J. A., Huang, Y. K., Niehaus, O. & Pottgen, R. Coexistence of different magnetic moments in CeRuSn probed by polarized neutrons. *Physical Review B* **91**, 014424 (2015).

114 Qureshi, N., Valldor, M., Weber, L., Senyshyn, A., **Sidis, Y.** & Braden, M. Magnetic spin-flop transition and interlayer spin-wave dispersion in $PrCaFeO_4$ revealed by neutron diffraction and inelastic neutron scattering. *Physical Review B* **91**, 224402, (2015).

115 **Rabot, E.**, Lacoste, M., Henault, C. & Cousin, I. Using X-ray Computed Tomography to Describe the Dynamics of Nitrous Oxide Emissions during Soil Drying. *Vadose Zone Journal* **14**, (2015).

116 Raneri, S., Barone, G., Crupi, V., Longo, F., Majolino, D., Mazzoleni, P., Tanasi, D., **Teixeira, J.** & Valentina, V. Technological analysis of Sicilian prehistoric pottery production through small angle neutron scattering technique. *Periodico Di Mineralogia* **84**, 1-22, (2015).

117 Recko, K., Wykowska, U., Olszewski, W., **Andre, G.**, Milczarek, J. J., Satula, D., Biernacka, M., Kalska-Szostko, B., Waliszewski, J. & Szymanski, K. Synthesis and magnetic properties of the multiferroic GaFeO3 of orthorhombic and hexagonal symmetry. *Journal of Optoelectronics and Advanced Materials* **17**, 1173-1178, (2015).

118 Rey, J., Dourdain, S., Berthon, L., **Jestin, J.**, Pellet-Rostaing, S. & Zemb, T. Synergy in Extraction System Chemistry: Combining Configurational Entropy, Film Bending, and Perturbation of Complexation. *Langmuir* **31**, 7006-7015, (2015).

119 **Ridier, K.**, **Gillon, B.**, **Andre, G.**, **Chaboussant, G.**, Catala, L., Mazerat, S. & Mallah, T. Small-angle neutron scattering study of the short-range organization of dispersed CsNi Cr(CN)(6) nanoparticles. *Journal of Applied Physics* **118**, (2015).

120 **Robert, J.**, **Damay, F.**, **Saito, K.**, **Bataille, A. M.**, **Porcher, F.**, **Andre, G.**, **Gukasov, A.**, **Mignot, J. M.**, Tanida, H. & Sera, M. Neutron diffraction study of magnetic order in $NdFe_2Al_{10}$. *Physical Review B* **90**, 224425 (2015).

121 **Robert, J.**, Lhotel, E., Remenyi, G., Sahling, S., **Mirebeau, I.**, Decorse, C., Canals, B. & **Petit, S.** Spin dynamics in the presence of competing ferromagnetic and antiferromagnetic correlations in $Yb_2Ti_2O_7$. *Physical Review B* **92**, (2015).

122 Rojas, D. P., Fernandez Barquin, L., Sanchez Marcos, J., Echevarria-Bonet, C., Espeso, J. I., Rodriguez Fernandez, J., Rodriguez Fernandez, L. & **Mathon, M. H.** Magnetic disorder in $TbAl_2$ nanoparticles. *Materials Research Express* **2**, 075001 (075009 pp.)-075001 (075009 pp.), (2015).

123 Rols, S., Pontiroli, D., Cavallari, C., Gaboardi, M., Aramini, M., Richard, D., Johnson, M. R., **Zanotti, J. M.**, Suard, E., Maccarini, M. & Ricco, M. Structure and dynamics of the fullerene polymer Li_4C_{60} studied with neutron scattering. *Physical Review B* **92**, (2015).

124 Rose, S., Marcellan, A., Narita, T., **Boue, F.**, **Cousin, F.** & Hourdet, D. Structure investigation of nanohybrid PDMA/silica hydrogels at rest and under uniaxial deformation. *Soft Matter* **11**, 5905-5917, (2015).

125 Rossi, B., Venuti, V., Paciaroni, A., Mele, A., **Longeville, S.**, Natali, F., Crupi, V., Majolino, D. & Trotta, F. Thermal fluctuations in chemically cross-linked polymers of cyclodextrins. *Soft Matter* **11**, 2183-2192, (2015).

126 Ruiz-Garcia, M., Bonilla, L. L. & Prados, A. Ripples in hexagonal lattices of atoms coupled to Glauber spins. *Journal of Statistical Mechanics-Theory and Experiment*, (2015).

127 Russo, D. & **Teixeira, J.** Mapping water dynamics in defined local environment: From hindered rotation to vibrational modes. *Journal Of Non-Crystalline Solids* **407**, 459-464, (2015).

128 Saha, D., Testard, F., Grillo, I., Zouhiri, F., Desmaele, D., Radulescu, A., **Desert, S.**, **Brulet, A.**, Couvreurc, P. & Spalla, O. The role of solvent swelling in the self-assembly of squalene based nanomedicines. *Soft Matter* **11**, 4173-4179, (2015).

129 Secret, E., Wu, C. C., Chaix, A., Galarneau, A., Gonzalez, P., Cot, D., Sailor, M. J., **Jestin, J.**, **Zanotti, J. M.**, Cunin, F. & Coasne, B. Control of the Pore Texture in Nanoporous Silicon via Chemical Dissolution. *Langmuir* **31**, 8121-8128, (2015).

130 Shi, L., **Buhler, E.**, **Boue, F.** & Carn, F. Shape-Tailored Colloidal Molecules Obtained by Self-Assembly of Model Gold Nanoparticles with Flexible Polyelectrolyte. *Langmuir* **31**, 5731-5737, (2015).

131 Singh, L. P., **Raihane, A.**, **Alba-Simionesco, C.** & Richert, R. Dopant effects on 2-ethyl-1-hexanol: A dual-channel impedance spectroscopy and neutron scattering study. *Journal Of Chemical Physics* **142**, 014501, (2015).

132 Slodczyk, A., Colomban, P., Upasen, S., Grasset, F. & **Andre, G.** Structural stability of anhydrous proton conducting $SrZr_{0.9}Er_{0.1}O_{3-\delta}$ perovskite ceramic vs. protonation/deprotonation cycling: Neutron diffraction and Raman studies. *Journal of Physics and Chemistry of Solids* **83**, 85-95, (2015).

133 **Songvilay, M.**, **Petit, S.**, Hardy, V., **Castellan, J. P.**, **Andre, G.**, Martin, C. & **Damay, F.** Random dilution effects in the frustrated spin chain β-$CaCr_{2-x}Sc_xO_4$. *Physical Review B* **91**, 054408 (2015).

134 Sood, R., Iojoiu, C., Espuche, E., Gouanve, F., Mendil-Jakani, H. & Lyonnard, S. Influence of different perfluorinated anion based Ionic liquids on the intrinsic properties of Nafion (R). *Journal of Membrane Science* **495**, 445-456, (2015).

135 **Teixeira, J.**, Magli, R. & Loupiac, C. Neutron scattering and imaging: a tool for archaeological studies. *European Journal of Mineralogy* **27**, 289-296, (2015).

136 Valiska, M., Pospisil, J., Stunault, A., Takeda, Y., **Gillon, B.**, Haga, Y., Prokes, K., Abd-Elmeguid, M. M., Nenert, G., Okane, T., Yamagami, H., Chapon, L., **Gukasov, A.**, **Cousson, A.**, Yamamoto, E. & Sechovsky, V. Gradual Localization of 5f States in Orthorhombic UTX Ferromagnets: Polarized Neutron Diffraction Study of Ru Substituted UCoGe. *Journal of the Physical Society of Japan* **84**, (2015).

137 Wahyudi, O., Ceretti, M., Weill, I., **Cousson, A.**, Weill, F., Meven, M., Guerre, M., Villesuzanne, A., Bassat, J. M. & Paulus, W. Growth of high quality single crystals of strontium doped (Nd,Pr)-nickelates, $Nd_{2-x}Sr_xNiO_{4+delta}$ and $Pr_{2-x}Sr_xNiO_{4+delta}$. *Crystengcomm* **17**, 6278-6285, (2015).

138 Wang, Q. C., Liu, S. B., Wang, X. M., Fu, H., Xu, J. G., Lu, F. Q., Veron, E., Allix, M., **Porcher, F.** & Kuang, X. J. Aliovalent-substitution defect chemistry, crystalline-glassy phase separation and ionic conductivity in fresnoite $Ba_2TiSi_2O_8$-based materials. *Solid State Ionics* **278**, 157-165, (2015).

139 Wasser, F., Schneidewind, A., **Sidis, Y.**, Wurmehl, S., Aswartham, S., Buchner, B. & Braden, M. Spin reorientation in $Ba_{0.65}Na_{0.35}Fe_2As_2$ studied by single-crystal neutron diffraction. *Physical Review B* **91**, 060505, (2015).

140 Xiang, Y. J., Moulin, E., Buhler, E., Maaloum, M., Fuks, G. & Giuseppone, N. Hydrogen-Bonded Multifunctional Supramolecular Copolymers in Water. *Langmuir* **31**, 7738-7748, (2015).

141 Yang, J., Pruvost, S., Livi, S. & Duchet-Rumeau, J. Understanding of Versatile and Tunable Nanostructuration of Ionic Liquids on Fluorinated Copolymer. *Macromolecules* **48**, 4581-4590, (2015).

142 Yokota, H., Nozue, T., Nakamura, S., Hojo, H., Fukunaga, M., Janolin, P. E., **Kiat, J. M.** & Fuwa, A. Ferroelectricity and weak ferromagnetism of hexagonal ErFeO3 thin films. *Physical Review B* **92**, (2015).

143 Younsi, K., Bez, R., Crivello, J. C., Paul-Boncour, V., Zehani, K. & Bessais, L. Structural and magnetic properties of $PrCo_{3-x}Fe_x$ by neutron powder diffraction and electronic structure investigations. *Journal of Solid State Chemistry* **230**, 19-25, (2015).

144 Zhang, L., Mikhailovskaya, A., Yazhgur, P., **Muller, F.**, **Cousin, F.**, Langevin, D., Wang, N. & Salonen, A. Precipitating Sodium Dodecyl Sulfate to Create Ultrastable and Stimulable Foams. *Angewandte Chemie-International Edition* **54**, 9533-9536, (2015).

145 Zhao, D., Ge, S. F., Senses, E., Akcora, P., **Jestin, J.** & Kumar, S. K. Role of Filler Shape and Connectivity on the Viscoelastic Behavior in Polymer Nanocomposites. *Macromolecules* **48**, 5433-5438, (2015).

146 **Zhong, S.-Y.**, Ribis, J., Lochet, N., De Carlan, Y., **Klosek, V.**, Ji, V. & **Mathon, M.-H.** The Effect of Y/Ti Ratio on Oxide Precipitate Evolution in ODS Fe-14 Wt Pct Cr Alloys. *Metallurgical And Materials Transactions A-Physical Metallurgy And Materials Science* **46A**, 1413-1418, (2015).

Software development

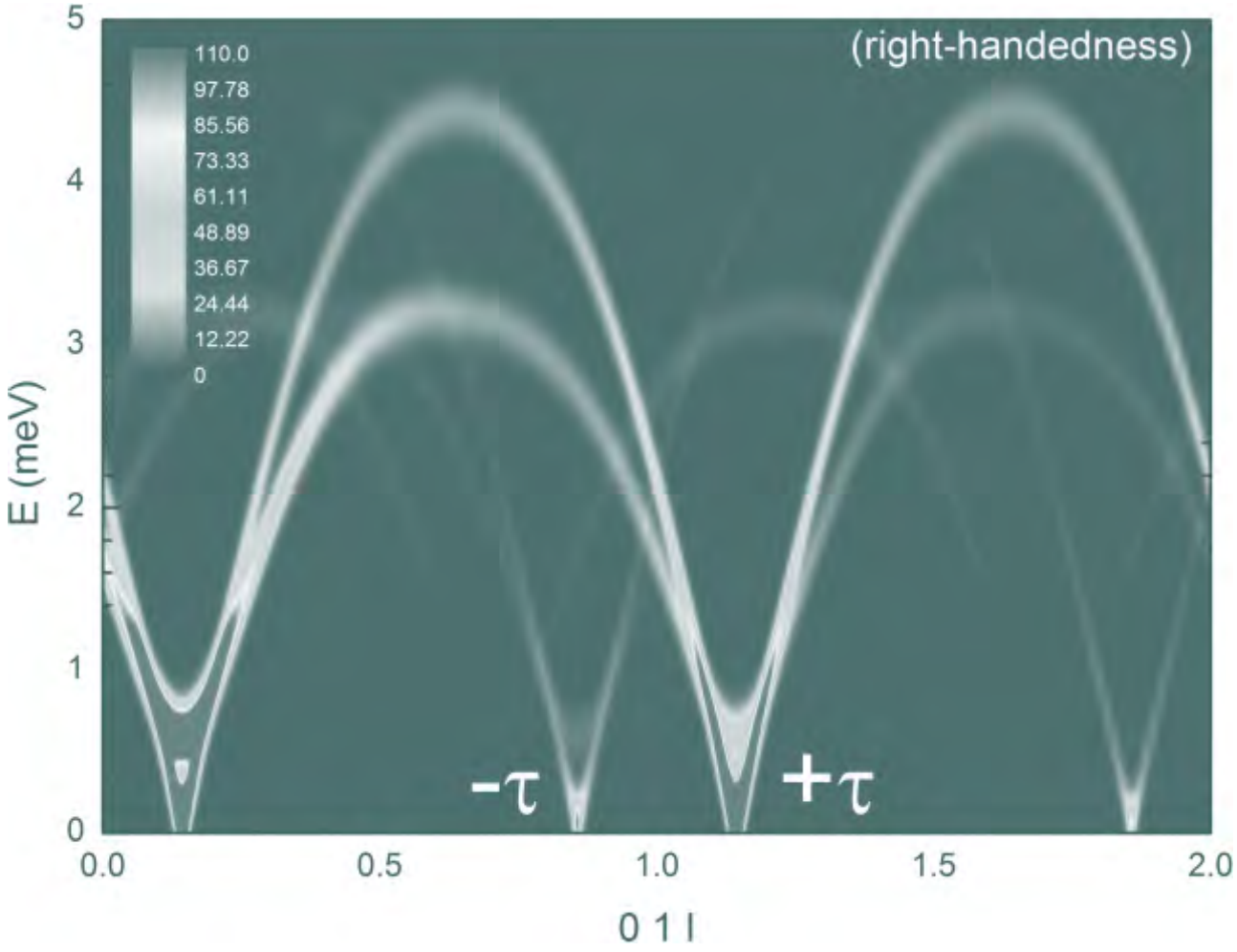

Public release of the *SpinWave* software

An easy-to-use and versatile software, SpinWave, to calculate spin waves in any arbitrary magnetic lattice, has been developed at Laboratoire Léon Brillouin and is now freely available.

S. Petit

Laboratoire Léon Brillouin CEA/CNRS UMR 12, Gif sur Yvette, France

sylvain.petit@cea.fr

Since the 1950's, spin wave theory has been of fundamental importance in condensed matter physics. Spin waves are obtained from the linearization of the equation of motion, and can be seen as precession modes of the magnetically ordered structure, with typical energies of a few meV. Spin wave dispersions are routinely measured by neutron spectroscopy, and provide information about the coupling between spins and magnetic anisotropy parameters.

The spin wave calculating code [1], *SpinWave*, developed at LLB, allows one to simulate the spin waves spectra of commensurate, as well as incommensurate magnetic structures, using linear spin-wave theory. Several types of magnetic exchanges, including Heisenberg, anisotropic, or Dzyaloshinskii-Moriya interactions, can be included in the Hamiltonian (Figure 1). In addition to the dispersion, spin-spin correlation functions, chiral correlations, with or without magnetic form factor, can be calculated. Calculations in any direction of the reciprocal space, and constant energy cut calculations in any plane of the reciprocal space are possible, as well as the calculation of the powder-averaged spin wave spectrum. *SpinWave* also features the possibility to use classical energy minimization to determine the ground state (single k) magnetic structure for a set of magnetic exchange and anisotropies.

SpinWave is developed and maintained by Dr. Sylvain Petit at LLB.

It can be downloaded at the following address : www-llb.cea.fr/logicielsllb/SpinWave/SW.html

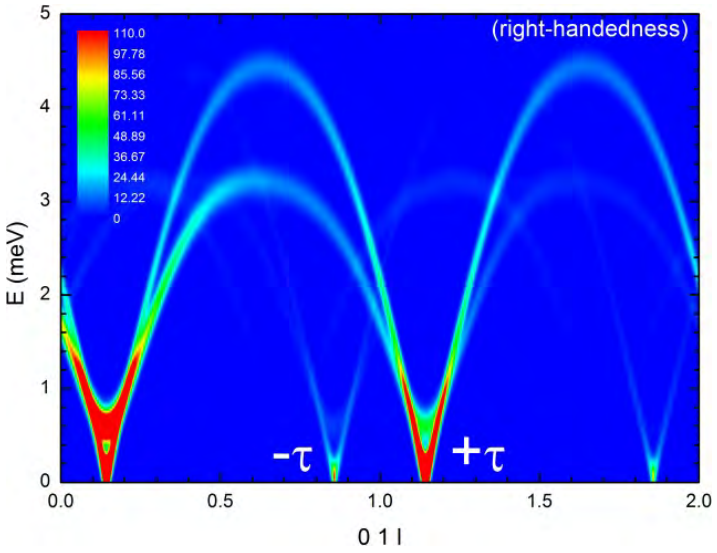

***Figure 1** : Dynamical structure factor S(Q, E) along (01l) of langasite $Ba_3NbFe_3Si_2O_{14}$, calculated with SpinWave. The calculation illustrated here has been performed for a right-handed crystal, using a Hamiltonian with 5 different exchanges, and an antisymmetric Dzyaloshinskii-Moriya (DM) term, whose vector is parallel to c. This DM term produces a gap in the lower branch of the dispersion and also selects the triangle magnetic chirality. The structural chirality is actually reflected [2] in the S(Q,E) : the asymmetric spectral weight of the branches emerging from the -τ and +τ satellites is inverted for the other eniantomeric form (left-handed) of $Ba_3NbFe_3Si_2O_{14}$.*

References:

1. S. Petit, Numerical simulation and magnetism, Collection SFN, ***12****, 105-121, 2011.*

2. M.Loire, V. Simonet, S. Petit, K. Marty, P. Bordet, P. Lejay, J. Ollivier, M. Enderle, P. Steffens, E. Ressouche, A. Zorko, and R. Ballou, Phys. Rev. Lett. ***106****, 207201, 2011.*

PINGOUIN: An open and generic software platform for the LLB neutron spectrometers

PINGOUIN is a software platform developed by IT team for data acquisition and control of all neutron spectrometers at the Laboratoire Léon Brillouin (LLB). This platform is the result of the expertise acquired over the years by IT and Electronics LLB Team aimed to propose a user friendly neutron spectrometers framework. It was designed keeping in mind to faster meet the needs of the users.

G. Exil, A. Laverdunt, E. Jorgji
Laboratoire Léon Brillouin CEA/CNRS UMR 12, Gif sur Yvette, France

gaston.exil@cea.fr

PINGOUIN

The platform integrates advanced information technologies like the XML metadata model for a quick and simplified deployment on all the facilities. Furthermore, and thanks to a modular architecture, reliability and maintenance have been improved, through easy detection of dysfunction and breakdowns.

Generic: PINGOUIN was planed to be used on all neutron spectrometers of the laboratory. Therefore it allows for full customization to match users requirements and wishes, although its intimate structure remains the same.

Open: The plateform accepts code from other sources. Thus, the features specific to a spectrometer can be described in python script, PINGOUIN is able to execute and keep in its library.

Protection of resources: For the same spectrometers, different user profiles are subject to corresponding access privileges/authorisations. The platform allows the spectrometer responsible to customize very finely authorizations for use and modification of ressources.

LLB SPECTROMETERS USING PINGOUIN

LLB maintains 23 neutron spectrometers installed around the ORPHEE research reactor, all equipped with the electronic acquisition system provided by Electronic LLB Team. The science aimed by each spectrometer is different, such as the small angle scattering, crystallography or magnetism.

PINGOUIN is installed in 8 neutron spectrometers. The plateform has proved his ability to equip the different experimental instruments installed by the LLB.

Therefore, we could demonstrate that the platform can provide an effective and easy to use working environment for the experimenters.

The neutron spectrometers using PINGOUIN now are 7C2, 6T2, 6T1, 5C2, 5C1(VIP) , G43(BAROTRON), IMAGINE, PA20.

AN EXAMPLE OF PINGOUIN VISUAL INTERFACE

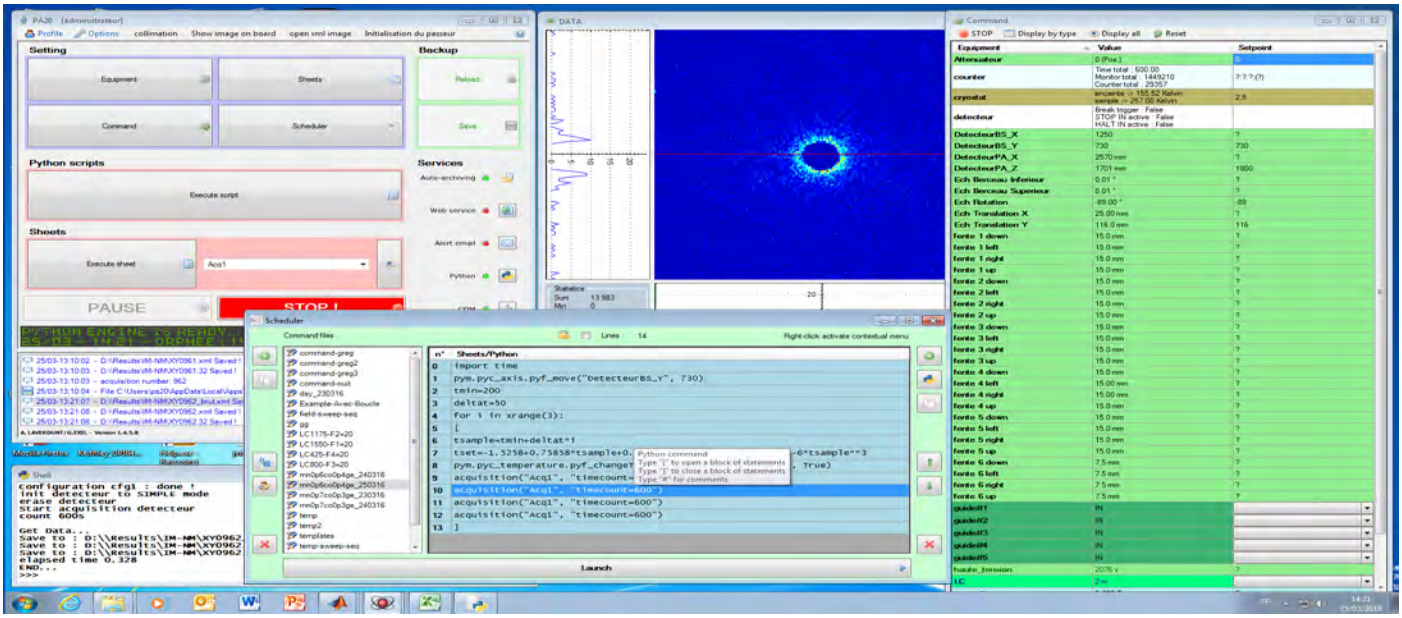

PYTHON, THE SCRIPT ENGINE

Python is a programming language object, multi-paradigm and cross-platform. It promotes imperative structured programming, functional and object-oriented. It is under a free license and runs on most computing platforms, from supercomputers to personal computers, from Windows to Unix through GNU/Linux, MacOS, or Android.

It is designed to maximize programmer productivity by providing high-level tools and a simple syntax. Python is the PINGOUIN scripting language for executing user sheets and to provide instruction sequences to the scheduler.

So, users can automate their acquisitions with the scripts they developed themselves. They are also able to make data pre-processing using graphics and scientific libraries provided by the Python community.

```
from pythonScriptingInVB import *
import time
pym.pyc_axis.pyf_move("DetecteurBS_Y", 730)
tab_temperature = [224.5, 233, 241, 249, 257]
for temp in tab_temperature:
        pym.pyc_temperature.pyf_changeTemperature("cryostat", temp, True)
        acquisition("Acq1", "count=600")
        #acquisition("Acq1", "count=600")
        print temp
        time.sleep(2) # tempo de 2s
```

Python script example

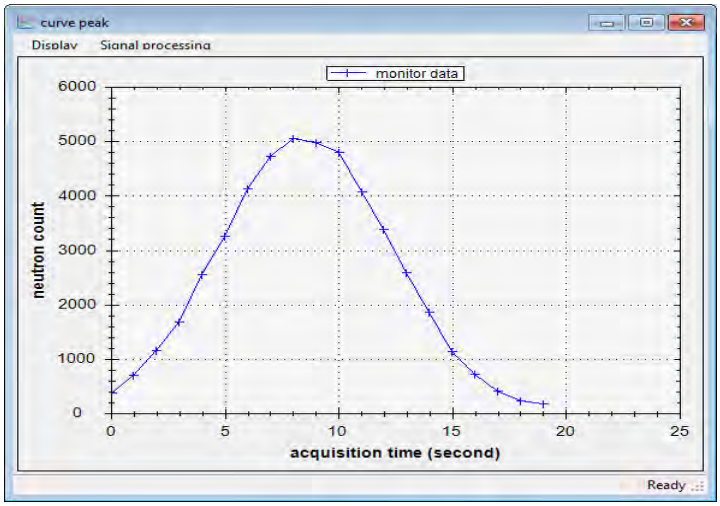

A curve generated with python

Microsoft .NET TECHNOLOGY

Microsoft Visual Studio is an integrated development environment (IDE) from Microsoft. We use this environment to develop the visual interface of Pingouin.

Visual Studio supports different programming languages and allows the code editor and debugger to support (to varying degrees) nearly any programming language, provided a language-specific service exists. Built-in languages include C, C++ and C++/CLI (via Visual C++), VB.NET (via Visual Basic .NET), C# (via Visual C#). Support for other languages such as M, Python, and Ruby among others is available via language services installed separately.

The languages uses to develop PINGOUIN core are C, C++, VB.NET and C#.

COMMUNICATION PROTOCOLS

PINGOUIN provides 4 native protocols to interface with a wide range of equipment.

RS232 is a standard for serial transmission of data. The data, input or output, are transferred one bit at a time. Available on almost every personal computer since 1981 until the mid of 2000, it is commonly called the "serial port".

IEEE-488 is a short-range digital communications 8-bit parallel multi-master interface bus specification. IEEE-488 was created as HP-IB (Hewlett-Packard Interface Bus) and is commonly called GPIB (General Purpose Interface Bus). It has been the subject of several standards.

TCP/IP The Transmission Control Protocol (TCP) is a core protocol of the Internet protocol suite. It originated in the initial network implementation in which it complemented the Internet Protocol (IP). Therefore, the entire suite is commonly referred to as TCP/IP. TCP provides reliable, ordered, and error-checked delivery of a stream of octets between applications running on hosts communicating over an IP network.

USB, short for Universal Serial Bus, is an industry standard developed in the mid-1990s that defines the cables, connectors and communications protocols used in a bus for connection, communication, and power supply between computers and electronic devices. It is currently developed by the USB Implementers Forum (USB IF). Pingouin uses the CYPRESS driver to connect to peripheral USB devices provided by the Electronic Group.

Events and workshop

Workshop on the new opportunities in neutrons scattering with small to medium sources

The LLB organized in Paris the 18 and 19 May 2015 a workshop dedicated to the development of small to medium neutron sources as new opportunities in neutrons scattering.

Invited speakers of the main laboratories working on or around the subject (LENS, ESS Bilbao, IRFU, MUNES, SINQ, CNEA, PSI, ISIS, Hokkaido University) presented the most recent advances in the conception and the applications of compact neutron sources.

After a general overview, presentations and discussions on high intensity accelerator, LINAC use, target-moderator systems, possibilities of scattering/imaging and applications in cultural heritage and proton therapy for example, allowed a widespread understanding of the recent advances and difficulties of the domain.

This workshop has to be considered as the starting point of the reflection and action launched by the LLB for the implantation of a new compact source in Saclay. This source (SONATE project) will offer to the users and the researchers an alternative for French neutron scattering after the end of the exploitation of Orphée reactor in 2019.

Teaching and education

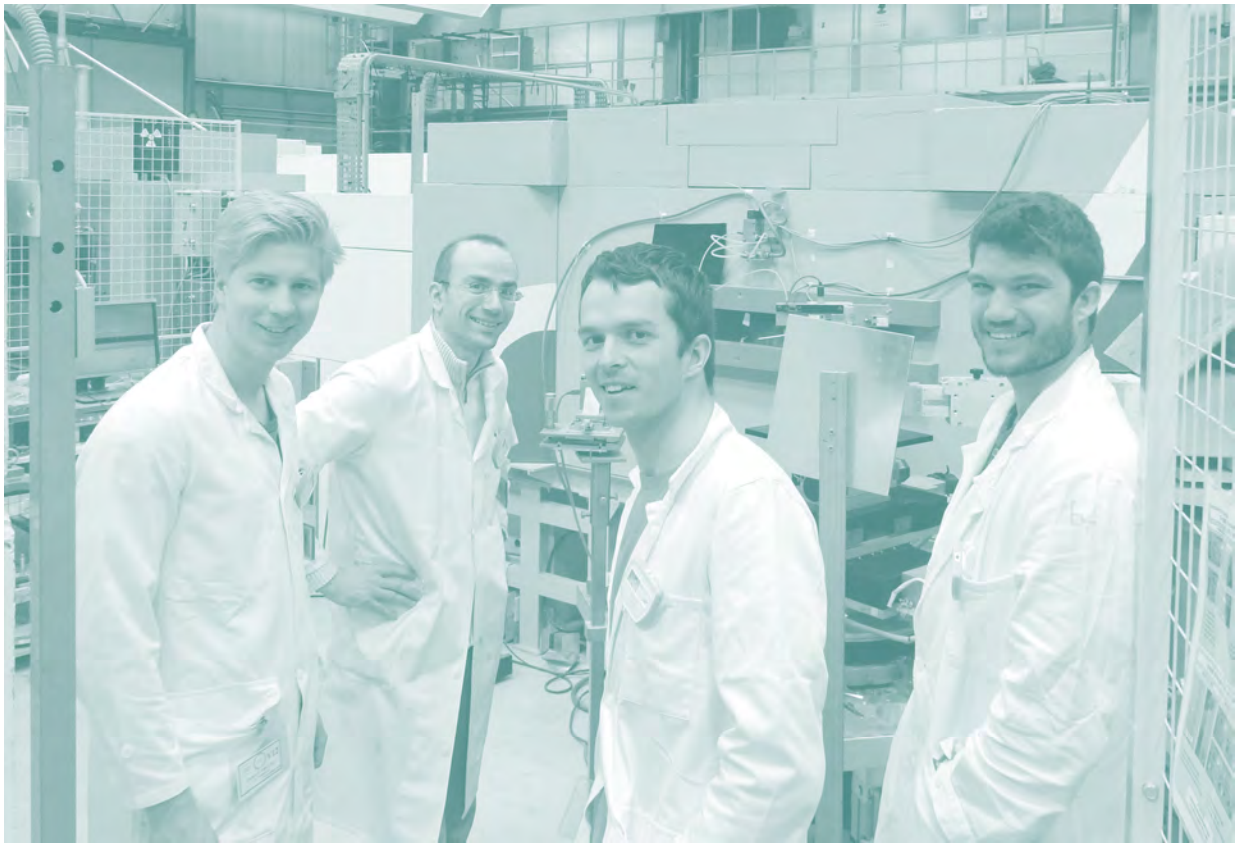

Theses defended in 2015

MANGIN-THRO Lucile

"Phase de "Boucles de courants circulants" dans les supraconducteurs à haute température critique"

Superviser: P. Bourges (Magnetism and super conductivity)

GUITTENY Solène

« Structure et dynamique de spin dans les pyrochlores géométriquement frustrés »

Superviser: S. Petit (Magnetism and super conductivity)

FERDEGHINI Filippo

« Liquide ionique sous confinement nanométrique 1D »

Superviser: J.M. Zanotti (Soft complex matter and biophysics)

BLOUZON Camille – (LLB/SOLEIL call)

« Manipulation d'une aimantation par l'action d'un champ électrique en utilisant un matériau 'multiferroïque »

Supervisers: M. Viret (SPEC) / F. Ott (Material and nanosciences, fundamental studies and applications)

KAHL Philipp

« Identification de nouvelles propriétés dynamiques dans les liquides : corrélations solides à longue portée & rôle de l'interaction fluide/substrat »

Superviser: L. Noirez (Material and nanosciences, fundamental studies and applications)

SCUSSAT Simone – *(*LLB/SOLEIL call*)*

« Compréhension des mécanismes de dénaturation des protéines en milieu complexe et pseudo solide. Mise ne place de sondes biophysiques pour les suivre »

Superviser: C. Loupiac (Dijon)/ F. Cousin (Soft complex matter and biophysics)

New PhD students in 2015

MATSUBARA Nami – CTCR – 2015-2018

« Trirutiles et propriétés multiféroïques : exploration de tellurates »

Superviser: C. Martin (ENSI CAEN) / F. Damay (Magnetism and super conductivity)

MAIRE DU POSET Aline –Agrosup Dijon – 2015-2018 (LLB/SOLEIL call)

« Etude de matrices à base de pectine pour un enrichissement en fer dans les aliments : Influence de l'organisation du gel sur l'environnement local, le degré d'oxydation et la biodisponibilité du fer »

Superviser: P. CAYOT (Univ. Bourgogne) / F. Cousin (Soft complex matter and biophysics)

PARTOUCHE David – Univ. Paris VII - 2015-2018 (LLB/SOLEIL call)

« Analyse de l'assemblage de peptides amyloïdes bactériens »

Superviser: V. Arluison *(Soft complex matter and biophysics)*

KUBIAK Krzysztof-Univ. De Gdansk (Pologne) – 2015 -2018

« Etude de la réplication des plasmides de type Cole1 »

Superviser: V. Arluison (Soft complex matter and biophysics)

HERCULES Courses (16-20 March 2015)

For its 25th edition, from March 1st to April 1st, 2015, the European school HERCULES (Higher European Research Course for Users of Large Experimental Systems) welcomes 80 young researchers from all over the world for a high level course in experimental research on large systems. Founded in 1991, the school HERCULES has emerged for the past 25 years as the reference school at international level regarding courses for users of large synchrotron and neutron radiation facilities.

During several weeks, lectures, tutorials, and practical sessions on the applications of X-Rays and neutron scattering are given by specialists of the domains. A week of this formation takes place in the Paris area, at the SOLEIL synchrotron and at the LLB for those participants interested in a reinforced experimental neutron program. At the LLB they had the opportunity to exercise on real spectrometers after a general presentation of the installation and a visit of the reactor hall.

The students were spread over 18 organized practical work.

JDN 23, Neutron Imaging Workshop, Rencontres Rossat-Mignod 5 - 8 October Evian Les Bains

Since its creation, LLB has been participating to the organization and the scientific contributions of the "Journées de Diffusion Neutronique" (JDN). The JDN is the main French annual meeting rendezvous of all the neutron scattering community.

Participants of the Neutron Imaging workshop

In 2015, workshop on new developments and applications of neutronic imaging, Rossat Mignod meeting on soft matter and biology, magnetism and nanosciences and a joint session with the Swedish neutron society took place during the JDN.

The SFN 2015 prize was awarded by the chairman of the jury, Jean-Michel Kiat, to Alexis Chennevière. The laureate has presented his thesis work on dynamics of grafted polymer chains.

FAN du LLB, 7 – 11 December, Saclay

The French neutron scattering training, the "FAN du LLB 2015" has taken place on December 7-10th 2015.

Since more than 20 years, this school has been devoting to young researchers interested in the use of neutron scattering for the study of matter.

15 participants have attended the courses and practical experiments.

The main domains presented are condensed matter (nanomagnetism, structure materials, structure determination and dynamics) and soft matter (volume and surface structure characterization, dynamics in biology, polymers and composites, heterogeneities and imaging).

Practical works which represent 75% of the training have been focused on powder scattering, monocrystal triple axis, SANS and Neutron Spin Echo .

Each participant used two different spectrometers in its chosen domain.

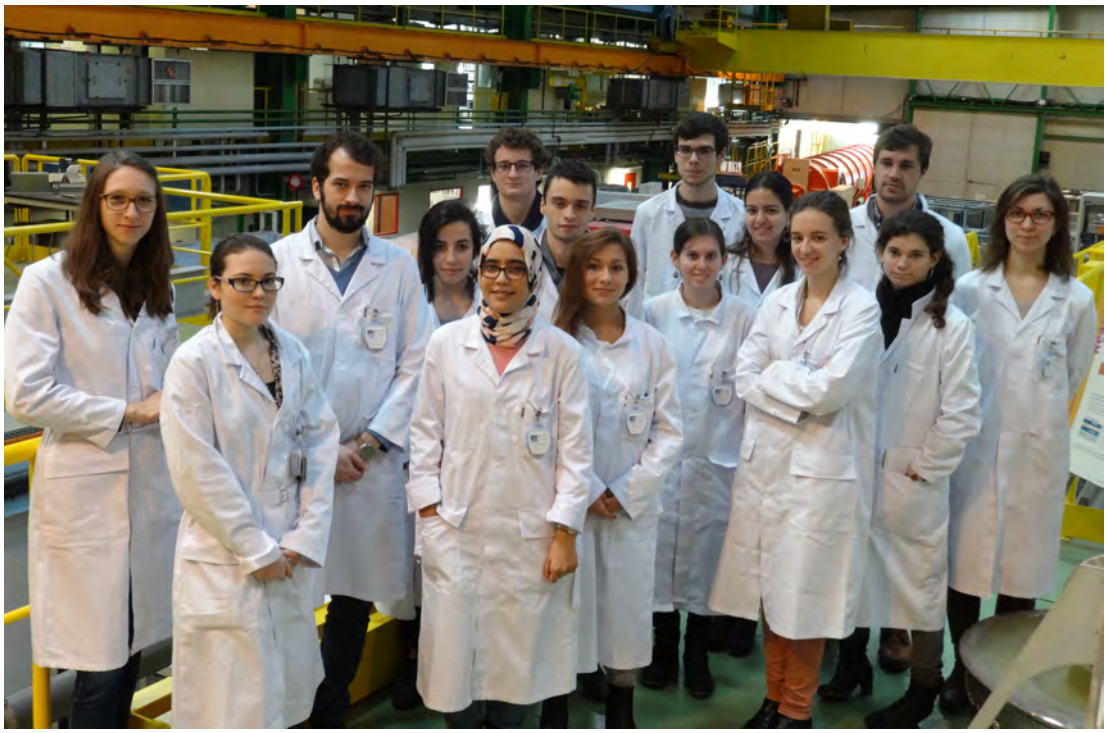

Spectrometers: what's new ?

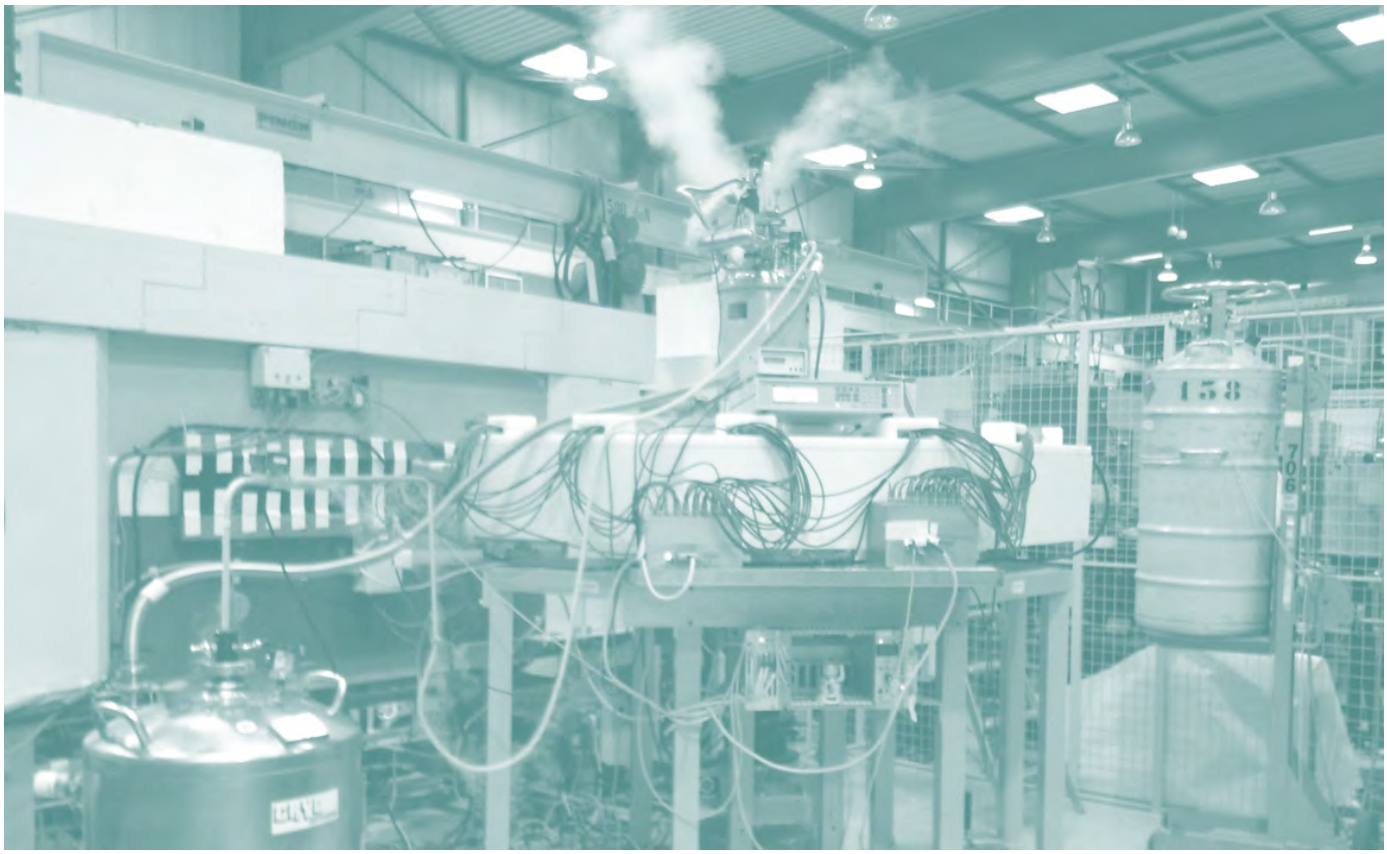

PHR-G44: a new cold neutron, high resolution diffractometer at LLB

F. Porcher, X. Guillou, P. Lavie, B. Rieu
Laboratoire Léon Brillouin CEA/CNRS UMR 12, Gif sur Yvette, France

florence.porcher@cea.fr

The new LLB diffractometer, PHR-G4.4, has received his first users in 2015. Installed at the fourth position of the cold neutron guide G4 of the hall of guides, it beneficiates of its natural a1 collimation. Its Ge(hhl) focusing monochromator provides four different wavelengths for a nominal take-off angle of 113° (adjustable) : 1.8 / 2.0 / 2.4 / 2.9Å (see Fig. 1).

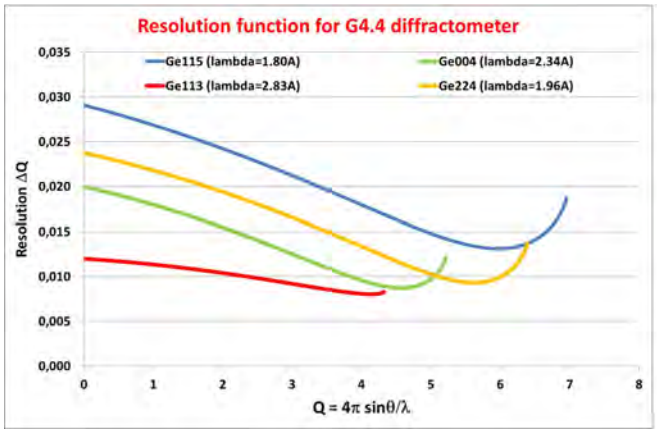

***Figure 1** : Resolution curves of PHR-G4.4*

The banana-type detector is equipped with 70 ^{3}He counters, 2° apart, preceded by 12' collimators . Maximum beam size at sample is ~1.5x5cm, and is practically limited by slits in the horizontal plane (1 cm) and is typically focused vertically down to 3-4 cm in order to fit sample size. Wavelength change is fully automatized and takes less than 1h (including beam optimization). This option allows to collect easily on the same sample data with high DQ/Q resolution for the determination of incommensurate nuclear/magnetic vectors (l = 2.4 / 2.9Å) and high Q-range for structural refinements (l = 1.8 / 2.0Å).

The diffractometer is equipped with a Orange-type cryofurnace (2K—450K) and shares high temperature furnaces with the high resolution thermal diffractomer 3T2 for measurements up to 1400°C (under 10^{-5} mbar) or 1050°C (under gas flow).

Typical applications deal with solid state physics, chemistry and material science (High-resolution refinements of nuclear or magnetic structures in complement to XRD or magnetic structure studies :

- Microporous materials (Zeolites and MOFs)
- Deuterated organic compounds, pharmaceuticals, organometallics
- Magnetic materials with magnetic periods 10< q <30Å

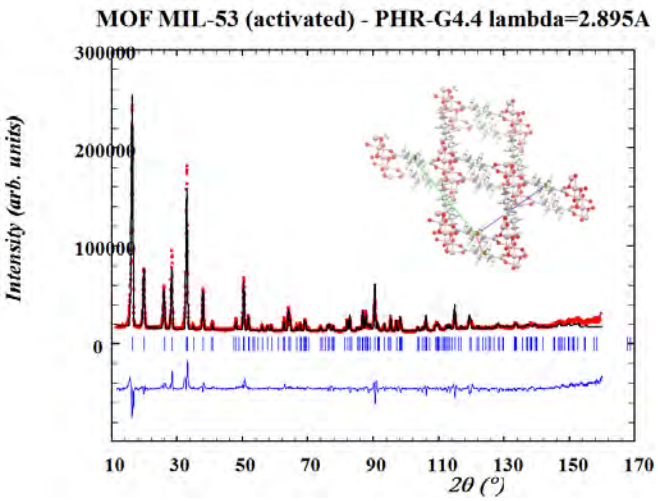

***Figure 3**: Rietveld refinement of a MOF*

***Figure 2**: The PHR-G4.4 diffractometer and its cryofurnace*

Complementary to 3T2, PHR-G4.4 is best suited for structural refinements of samples with larger primitive unit cell volume (1000 < V < 8000Å^{3}). With better resolution but longer data acquisition time (typically 1.5 day) at l = 2.4Å, PHR-G4.4 complements the high-flux diffractometer G4.1 which is better adapted for thermo-diffractometry and following magnetic transitions.

Change of the first 13 m of the neutron guide G4

Among the 6 neutron guides of the Orphée reactor, guide 4 (G4) feeds 5 experiments. One of these is the industrial neutron radiography station located at its very end. This position, at about 50 m from the core, provides a very low background and a pure cold neutron spectrum which enables very fine pictures.
However, from the beginning of Orphée in 1981, this station suffers of a slow and constant decrease of intensity. After a re-alignment in 2000 that restored only partially the lost intensity, we have undertaken the replacement of its first 13 m.
The assembling and alignment of the guide elements on the site was entirely done by LLB staff during the summer shutdown of the reactor. If the expected gain of flux was not there at the restart, this replacement allowed us to earn a lot of experience that will be an asset for us in the preparation of our ESS instruments.

A. Menelle

Laboratoire Léon Brillouin CEA/CNRS UMR 12, Gif sur Yvette, France

alain.menelle@cea.fr

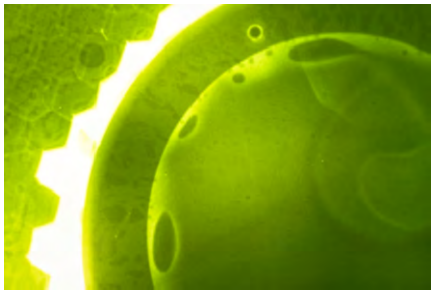

G4: A CROWDED GUIDE

The neutron guide G4 is located in the middle of our six guides fan (see fig. 1). With a length of 63 m, it is our longest large guide. Five different spectrometers use simultaneously the neutron transported by this guide. This represents roughly 20% of our full experimental capacity. It is important that this guide keeps its high quality.

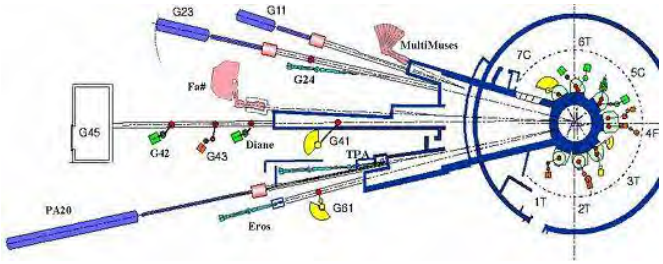

***Figure 1** : General layout of the Orphée guide system. G4 is located in the middle of the guide hall, finishing on the left side in G45.*

THE SLOW DEGRADATION OF THE END GUIDE INTENSITY

The industrial neutron radiography station has been installed quite soon after the start of the Orphée reactor at the end of guide G4. From early 1992 to 2000, the intensity has been monitored by the same uranium foil detector. The measured variations of intensities have been first attributed to the installation and movements of the 4 upstream monochromators. However, after some years, the continuous decrease of intensity with time (see fig. 2) we suspected a degradation of the alignment of the guide elements due to ground movements.

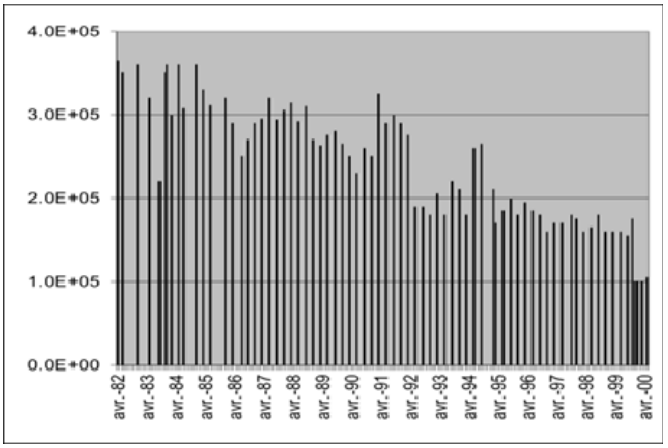

***Figure 2**: Evolution with time of the intensity recorded with a monitor at the end of guide 4.*

Unfortunately, a first re-alignment in 2000 recover only a small part of the lost intensity. Gold foil activation measurements were performed in 2011 at 5 different positions along the guide. They show up a continuous decrease of the intensity along the guide (see fig. 3) which could be better explained by a global decrease of reflection quality of the guide coating than by punctual misalignment.

Measurements performed end of 2011 on old guide coatings did show two important features. The total reflection was only measured at 98.2 % and 96.5 % respectively on an 11 and 30 years old element. The level of the off-specular intensity was increased drastically compared to a fresh coating; it was respectively 0.2 % and 0.8 % instead of usually less than 0.01 %.

These bad reflection characteristics were not improved by a careful cleaning of the element. Our conclusion was that the reflective qualities of the guide coating are slowly degrading with time.

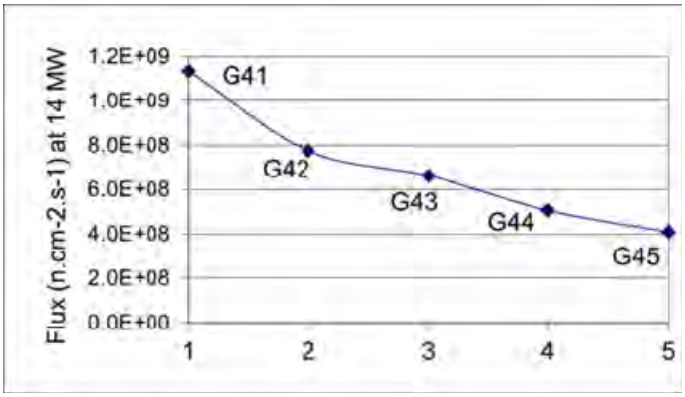

***Figure 3**: Evolution of the thermal flux measured along the guide G4 in February 2011 (the line is only a guide for the eyes; measurements have been done at positions G41, G42, G43, G44 and G45).*

Unfortunately, flux simulations using ray tracing software's could not reproduce the measured intensity with only a decrease of the reflection coefficient. We expected to have a mixture of both effects; a degradation of the coating and misalignment. We decided that the only way to recover the initial performances of G4 was to replace all the elements of the guide. Due to funding limitations, we did started by the replacement of only the first 13 m inside the containment (see fig. 4). It was done during the summer 2015 shutdown of Orphée.

CHANGING A GUIDE: A NEW EXPERIENCE

Guides elements were ordered from the SDH company. They were installed by the LLB staff using for the first time a laser tracker. The use of this instrument enables us to show that the containment exit valve was 2 mm lower than the safety valve. We also discovered small non-conformity between the original drawings of the guide and the reality. Due to the high level of radiations the alignment of the first element at the end of the beam plug after the main shutter was a bit more difficult than expected, as it was for le last element in the containment valve. In the overall, this work was a great enrichment for all the team that did earn a lot of experience in guide installation.

PERFORMANCES ASSESSMENTS

After the restart of the reactor in September, flux measurements were performed at the G42 position by gold foil activation. The thermal flux was raised from 0.77 10^9 n.cm^{-2}.s^{-1} to 0.99 10^9 n.cm^{-2}.s^{-1} corresponding to a 28 % increase. This is an encouraging result that show that a full change of the guide should completely restore its original performances.

***Figure 4**: A view of the beginning of the guide G4 before the change.*

Beam Time Access

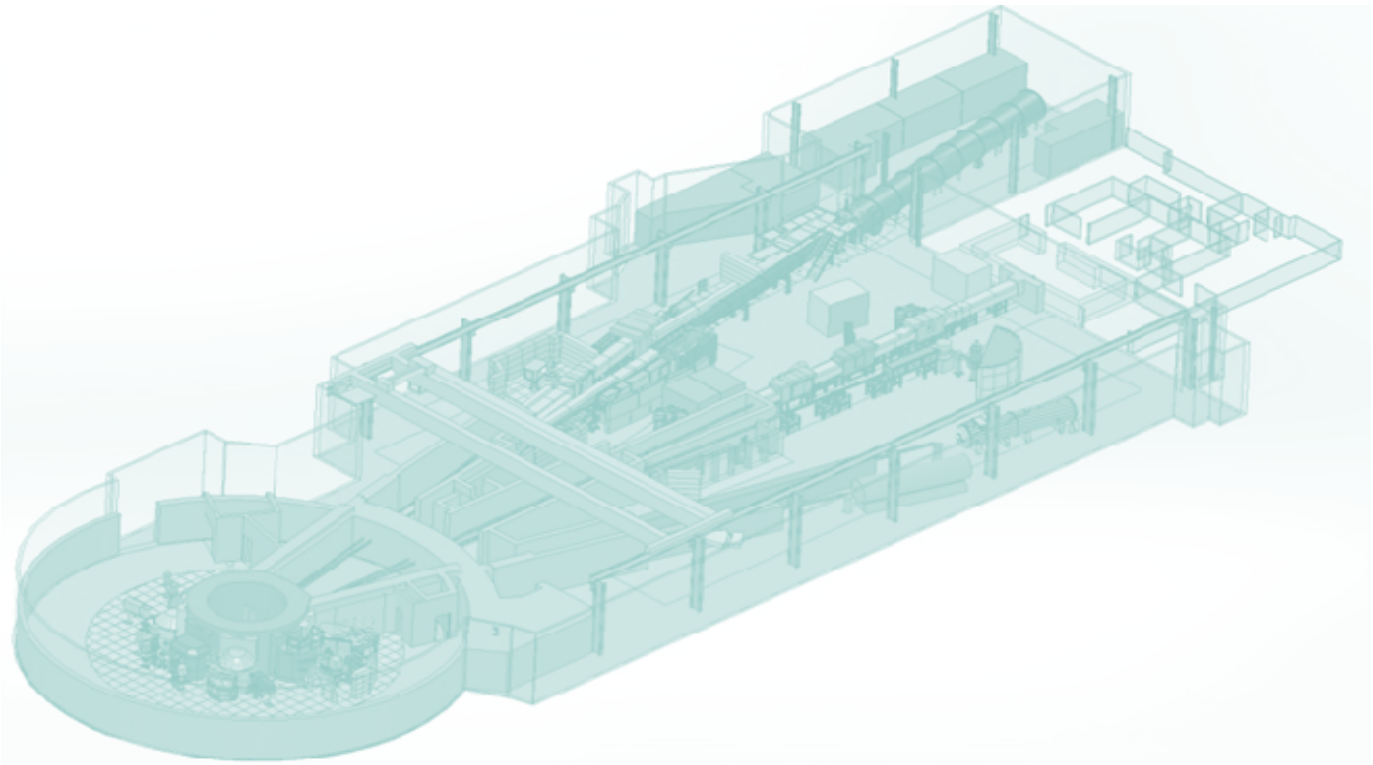

General layout of the spectrometers

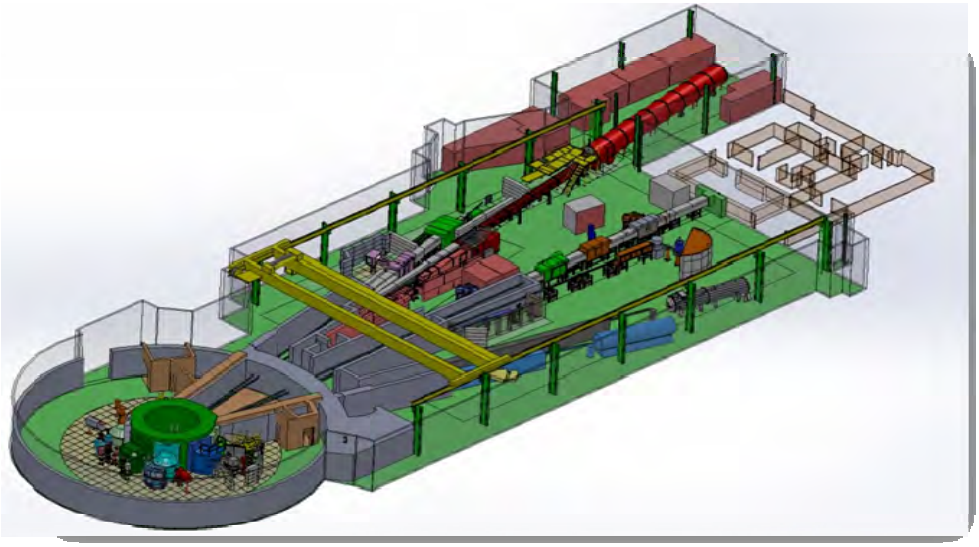

	SPECTROMETERS OPEN TO USERS	CONTACTS
	Powder diffractometers	
3T2	Florence Porcher	florence.porcher@cea.fr
G4.1	Françoise Damay	francoise.damay@cea.fr
G4.4 PHR	Florence Porcher	florence.porcher@cea.fr
G6.1	Florence Porcher	florence.porcher@cea.fr
	Single crystal diffractometers	
5C1 - VIP	Béatrice Gillon	beatrice.gillon@cea.fr
5C2	Alexandre Bataille	alexandre.bataille@cea.fr
Super 6T2	Arsen Goukassov	arsen.goukassov@cea.fr
	Diffuse scattering instrument	
7C2	Jacques Darpentigny	jacques.darpentigny@cea.fr
	Small-angle scattering instruments	
G1.2 - PACE	Sophie Combet	sophie.combet@cea.fr
G2.3 - PAXY	Fabrice Cousin	fabrice.cousin@cea.fr
G5.1 - PA20	Gregory Chaboussant	gregory.chaboussant@cea.fr
G5bis - TPA	Annie Brûlet	annie.brulet@cea.fr
	Diffractometers for material science studies	
6T1	Marie-Hélène Mathon	marie-helene.mathon@cea.fr
G4.2 - DIANE	Marie-Hélène Mathon	marie-helene.mathon@cea.fr
	Reflectometers	
G6.2 - HERMES	Didier Lairez / Lay-Theng Lee	didier.lairez@cea.fr / lay-theng.lee@cea.fr
G2.4 - PRISM	Frédéric Ott	frederic.ott@cea.fr
	Triple-axis instruments	
1T	John Paul Castellan / Yvan Sidis (CRG Instrument Karlsruhe/LLB)	john-paul.castellan@cea.fr / yvan.sidis@cea.fr
2T	Philippe Bourges	philippe.bourges@cea.fr
4F1	Sylvain Petit	sylvain.petit@cea.fr
4F2	Jean-Michel Mignot	jean-michel.mignot@cea.cr
	Quasi-elastic instruments	
G1bis - MUSES	Jean-Marc Zanotti	jean-marc.zanotti@cea.fr
	Neutron radiography	
G3bis - IMAGINE	Frédéric Ott	frederic.ott@cea.fr
G4.5	Guy Bayon / Xavier Wohleber	guy.bayon@cea.fr / xavier.wohleber@cea.fr

The LLB neutron scattering and imaging instruments

Powder diffractometers

3T2 "Thermal neutrons" 2-axis (50 detectors) high resolution, mainly for nuclear structure determination.

G4.1 "Cold neutrons" 2-axis (multidetector 800 cells) high flux, mainly for magnetic structure determination.

G4.4 "Cold neutrons" 2-axis (70 detectors) high resolution, for structure determination on polycrystalline samples with large unit cell.

G6.1 "Cold neutrons" 2-axis, flat 2D detector with long wavelength and high flux for long period magnetic systems and liquids (Available with limited support) .

Single crystal diffractometers

5C1 "Hot neutrons" 2-axis with lifting arm, polarized neutrons, magnetic field (8 Tesla) for spin-density maps determination

5C2 "Hot neutrons" 4-circle for nuclear structure determination.

6T2 "Thermal neutrons" 2-axis, lifting arm and 4-circles, mainly for magnetic structure determination. 12 Tesla magnetic field available, 2D detector.

Diffuse scattering instruments

7C2 "Hot neutrons" 2-axis (multidetector 640 cells) for local order studies in liquid or amorphous systems. Cryostat and furnace available (1.2K to 1300°C). (Available with limited support)

Small-angle scattering instruments

G1.2 "Cold neutrons" (annular detector, 30 rings) for study of large scale structures in isotropic systems (mainly polymers and colloids).

G2.3 "Cold neutrons" (X-Y detector, 128x128 cells) for study of large scale structures (10 to 500 Å) in anisotropic systems (polymers under stress, metallurgical samples, vortex in superconductors).

G5.1 "Cold neutrons" (X-Y detector, 128x128 cells) for study of large scale structures (10 to 500 Å) in anisotropic systems (polymers under stress, metallurgical samples, vortex in superconductors). PA20.

G5bis Very Small Angle Neutrons Scattering spectrometer

Diffractometers for material science studies

6T1 "Thermal neutrons" 4-circle for texture determination.

G4.2 "Cold neutrons" 2-axis for internal strain determination in bulk samples . (Available with limited support)

Reflectometers

G6.2 "Cold neutrons" reflectometer operating in time-of-flight mode for multipurpose surface studies.

G2.4 "Cold neutrons" reflectometer with polarized neutrons and polarization analysis for the study of magnetic layers.

Triple-axis instruments

1T "Thermal neutrons" high-flux 3-axis instrument with focussing monochromator and analyser, mainly devoted to phonon dispersion curves measurements. High pressure cells (100 Kbar) available. CRG Instrument operated in collaboration with the KIT Karlsruhe

2T "Thermal neutrons" high-flux spectrometer with focussing monochromator and analyser, mainly devoted to spin-waves and magnetic excitations studies (1.5 to 80 meV).

4F1 **4F2** "Cold neutrons" high flux 3-axis instruments with double monochromator and analyzer, mainly devoted to the study of low-energy (15µeV to 4meV) magnetic excitations. Polarized neutrons and polarization analysis option available.

G4.3 "Cold neutrons" high resolution and low background 3-axis instrument. (Available with limited support)

Quasi-elastic instruments

G1bis "Cold neutrons", high resolution and high flux spin-echo instrument. It can study, in a large Q range, slow dynamics of large molecules in biology or long relaxation times like in glassy transition (Fourier times ~ 20ns)

Neutron Radiography and imaging

G3bis IMAGINE: Imaging station mainly dedicated to soft matter.

G4.5 Imaging technique : white beam facility for non-destructive control or dynamics imaging (NMI3 access only).

AUXILIARY SERVICES AVAILABLE

Laboratories for sample preparation:

- Chemistry laboratory
- Biological laboratory

Technical help for:

- Cryostat, Furnace (0.1 – 2000 K)
- Medium/High pressures
- High magnetic fields (up to 10 T)
- Mechanics, Cryogenics, *Vacuum*

http://www-llb.cea.fr/fr-en/spectros_p.php

Access to beam time and selection committees

2015 was the last year for classical selection committees and beam time access. From mid-2016, a joint LLB - CRGs selection committee has been set up in the frame of the new French federation of neutron scattering (2FDN).

Beamtime access is free of charge for any experimentalist from the French Scientific community. LLB takes in charge the expenses (travel and stay) of 2 people during the experiment.

Beamtime on the open-access spectrometers can be requested by submission of:

- *An experimental application to a Selection Committee (Normal Procedure)*
  This procedure is open to any public/industrial researcher that is interested in using neutron scattering for his research. Results should be free to be totally or partially published in a Scientific Review.
  DEADLINE FOR APPLICATION: April 1st and October 1st
  http://www-llb.cea.fr/en/fr-en/proposal.php

- *An experimental application to the Directors (Exceptional)*
  This special procedure should only be used exceptionally for hot topics, confidentiality reasons or if an anomaly in the review procedure is suspected. The delay between the acceptation decision and the realization of the experiment is shortened to the minimum.
  No deadline applies for such propositions (Application all along the year).
  http://www-llb.cea.fr/en/fr-en/proposal.php

- *A fast access application*
  This procedure allows a rapid access (1 to 2 months delay) to the spectrometers in order to perform a short experiment (1 day max.). It can be used for feasibility tests, sample characterization, obtaining complementary results…
  No deadline applies for such propositions (Application all along the year).
  http://www-llb.cea.fr/en/fr-en/prop-rap.php

CONTACT AT LABORATOIRE LEON BRILLOUIN

Laboratoire Léon Brillouin

Scientific Office

CEA SACLAY

Bâtiment 563 *F - 91191 Gif-sur-Yvette Cedex*

Tel. : 33(0) 1 69 08 60 38 *Fax : 33 (0) 1 69 08 82 61*

e-mail : experience-llb at cea.fr

Internet : http://www-llb.cea.fr

2015 Selection committees

Proposals are examined by 5 Selection Committees. Each is composed of 8 to 10 senior scientists that are nominated by the management of LLB for 3 years. At least half of them do not belong to the LLB and 2 or 3 are coming from foreign institutes.

For each spectrometer, LLB gives a beam-time available which is shared out by the committee; each proposal gets a grade A or B or C.

A : The experiment must be done and the committee allocates a beam-time

B : The experiment might be done if there is some extra beam-time,

C : The experiment is refused on scientific arguments.

Selection Committees are asked to take care of the educational duty of the LLB when proposal comes from new young searcher.

SELECTION COMMITTEES: SCIENTIFIC FOCUS AND SUB-FOCUS

CLASSIFICATION

Focus 1 : Chemical physics, biological systems

1.01 Polymers and Supramolecular Structures
1.02 Water, aqueous solutions, polyelectrolytes, surfactants
1.03 System of biological interest, Biophysics
1.04 Colloids, nanostructures
1.05 Gels,composite materials
1.06 Other...

Focus 2 : Crystallographic and magnetic structures

2.01 Crystalline structures
2.02 Phases transitions
2.03 Magnetic Structures
2.04 High pressures (on powders)
2.05 Spin densities
2.06 Other ...

Focus 3 : Disordered Systems, nanostructured materials and materials

3.01 Liquid and amorphous structures
3.02 Dynamics of disordered systems
3.03 Thin film materials
3.04 Nanostructured materials, precipitation, cavities,…
3.05 Crystallographic textures
3.06 Strains and residual stresses
3.07 Magnetic thin layers
3.08 Magnetic nano systems
3.09 Other...

Focus 4 : Excitations

4.01 Magnons
4.02 Supraconductivity
4.03 Coupling spin-network
4.04 Dynamics in frustrated systems
4.05 Polarized neutrons with polarization analysis
4.06 Phonons
4.07 Systems with strong quantum correlation
4.08 Other…

LLB 2015 Reviewing committees

LLB members	French users		European users	

COLLEGE 1: Chemical physics, biological systems

Organisers: G. Fadda, J. Jestin

F. Muller	S. Lyonnard‡	CEA, Grenoble	A. Orecchini	ILL, Grenoble
	F. Nallet [Pdt]	CRPP, Bordeaux	M. Maréchal*	CEA, Grenoble
	B. Deme	ILL, Grenoble		
	B. Jean	CERMAV, Grenoble		

COLLEGE 2: Crystallographic and magnetic structures

*Organisers: A. Bataille, X. Fabrèges**

F. Porcher	V. Paul Boncour	ICPME, Thiais	A. Daoud-Aladine‡	ISIS, UK
	C. Colin	I.Néel, Grenoble	E. Ressouche	ILL, Grenoble
	M. Allix	CEMHTI, Orleans	M. Meven*	MLZ, Garching

COLLEGE 3: Disordered Systems, nanostructured materials and materials

Organisers: P. Judenstein, P. Jégou

A. Menelle	J. Henry [Pdt]	CEA, Saclay	R. Magli	Milan
	O. Castelnau	ENSAM, Paris	M. Gonzalez‡	ILL, Grenoble
	C. Gatel	CEMES, Toulouse	M. Viret*	CEA, Saclay

COLLEGE 4: Excitations

Organisers: Y. Sidis, S. Petit‡

G. Chaboussant	B. Fauqué	ESPCI, Paris	L. Paolasini [Pdt]	ESRF Grenoble
	M. d'Astuto	IMPMC Jussieu, Paris	D. Lamago	KIT, Allemagne
	P. Steffens	ILL, Grenoble		

‡ Only for spring session - * Only for automn session

LABORATOIRE LEON BRILLOUIN
UMR 12 CEA-CNRS
CEA Saclay, Bât.563
F-91191 GIF-SUR-YVETTE Cedex
France

+33 (0)1 69 08 52 41
+33 (0)1 69 08 82 61

www-llb-cea.fr

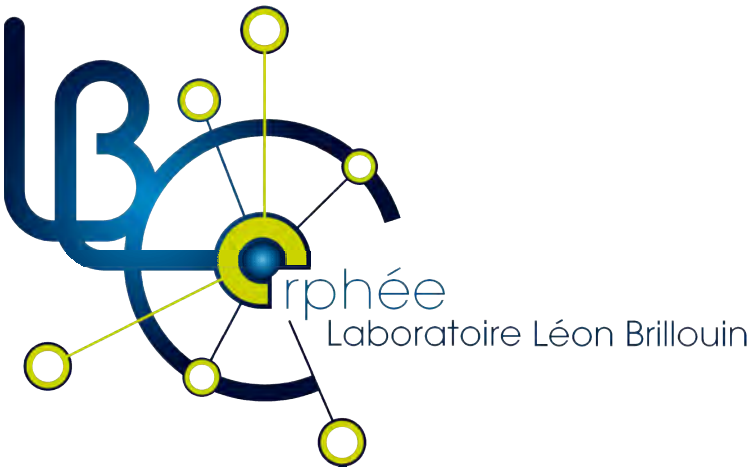

LABORATOIRE LEON BRILLOUIN
UMR 12 CEA-CNRS
CEA Saclay, Bât.563
F-91191 GIF-SUR-YVETTE Cedex
France

+33 (0)1 69 08 52 41
+33 (0)1 69 08 82 61

www-llb-cea.fr